Ministère de l'Enseignement Supérieur et de la Recherche Scientifique

Université Hassiba Benbouali de Chlef

Faculté de Technologie

Département d'Electrotechnique

THÈSE

Présentée pour l'obtention du diplôme de

DOCTORAT LMD

Filière : Electrotechnique

Spécialité : Commande électrique

Par

DJAFER Lemya

Thème:

Contribution a la Commande des Convertisseurs Multi-niveaux pour L'entraînement d'un Véhicule Electrique Multi-sources

(Contribution to the Control of Multi-level Converters for the Drive of a Multi-Source Electric Vehicle)

Soutenue le 12/02/2026 devant le jury composé de :

Pr. KANSAB Abdelkader	professeur	Université de Chlef	Président
Pr. TALEB Rachid	Professeur	Université de Chlef	Rapporteur
Dr. MEHEDI Fayçal	MCA	Université de Chlef	Co- Rapporteur
Pr. DJAHBAR Abdelkader	Professeur	Université de Chlef	Examinateur
Dr. LATROCH Maamar	MCA	Université de Chlef	Examinateur
Dr. MAAFA Amar	MCA	Université de Bouira	Examinateur
Dr. AISSA BOKHTACHTE Aicha	MCA	Université de Chlef	Invité
Pr. DJAFER Abderrahmane	Professeur	Université de Chlef	Invité

Acknowledgments

The work described in this thesis was performed within Laboratoire Génie Electrique et Energies Renouvelables (LGEER) at Hassiba Benbouali University of Chlef.

I wish to express my profound gratitude to my thesis supervisor, Pr. TALEB Rachid, professor at Hassiba Benbouali University of Chlef, and to my co-supervisor, Dr. MEHEDI Fayçal, MCA at the same institution. Their rigorous guidance, valuable insights, constructive advice, and continuous support were essential to the successful completion of this work. Collaborating with them has been a highly instructive experience, through which I have greatly enhanced my scientific knowledge. I particularly acknowledge their outstanding academic expertise and exemplary personal qualities.

I also extend my sincere appreciation to the members of the examination board for dedicating their time and expertise to the evaluation of this thesis, namely Pr. KANSAB Abdelkader (Chairman), Dr. MAAFA Amar (Examiner), Dr. LATROCH Maamar (Examiner), Pr. DJAHBAR Abdelkder (Examiner), Pr. DJAFER Abderrahmane (Guest) and Dr. AISSA BOKHTACHE Aicha (Guest).

My sincere thanks also go to Dr. AISSA BOKHTACHE Aicha and Pr. DJAFER Lahcen for their valuable support, insightful guidance, and continuous encouragement during the course of this work.

Finally, I wish to acknowledge all those who, whether directly or indirectly, contributed their support and assistance, even if they are not explicitly mentioned here.

Dedication

With great respect, I dedicate this work:

To my parents, in recognition of their continuous support, encouragement, and the sacrifices they have made throughout my journey.

To my husband Abde malik, may Allah bless him.

To my dear sisters Ibtissam, Ahlem and Aya.

To my father-in-law, whose wisdom, kindness, and encouragement have been a great source of inspiration.

To my family, friends, and all those who have supported me with their kindness and encouragement.

ملخّص- تشهد المركبات الكهربائية (VE) اهتمامًا متزايدًا باعتبارها حلًّا واعدًا لمواجهة أزمة الطاقة والتحديات البيئية. حاليًا تستخدم المركبات الكهربائية مجموعة واسعة من أجهزة إلكترونيات القدرة لتزويد المحرك بالطاقة اللازمة، مع ضمان تشغيل فعّال عند مستويات جهد عالية. وفي هذا السياق، تم تطوير العاكسات متعدّدة المستويات لتجاوز حدود المحوّلات التقليدية. تهدف هذه الأطروحة إلى تطوير بنية جديدة متعدّدة المستويات، بغرض تحسين أداء المركبات الكهربائية المزوّدة بعدّة مصادر للطاقة. يركّز العمل بشكل خاص على دراسة طوبولوجيا هجينة لا متناظرة جديدة لعاكس بقدرة 21 مستوى، يتميّز بانخفاض عدد عمليات التبديل، وذلك من أجل تحسين جودة جهد الخرج وبالتالي تحسين الأداء العام للمركبة الكهربائية. تم تصميم المبدل المقترح لتغذية محرك متزامن مزوّد بمغناطيسات دائمة (PMSM). يعتمد التحكم في المحرك بدايةً على أسلوب التحكم بالانزلاق (SMC)، وهي تقنية شائعة نظرًا لقدرتها العالية على تعويض التغيرات الداخلية في المعلمات والتعامل مع الاضطرابات الخارجية بكفاءة. ومع ذلك، ونظرًا لقيود هذه الطريقة، وخاصة ظاهرة التذبذب (Chattering)، تم تطوير تقنية محسَّنة وهي التحكم بالانزلاق الضبابي الهجين (HFSMC) التي تقلل بشكل ملحوظ من هذه الظاهرة. يتم تغذية النظام الكلي للمركبة الكهربائية بمصدرين للطاقة: خلية وقود كمصدر رئيسي، ومكثف فائق كمصدر ثانوي. تم إجراء محاكاة لتقييم أداء طوبولوجيا المبدل الجديدة، خاصة فيما يتعلق بتحسين جودة جهد الخرج وتقليل معدل التشويه التوافقي الكلي (THD). كما أُجريت سلسلة أخرى من المحاكاة على النظام الكلي للمركبة الكهربائية. أظهرت النتائج المحققة موثوقية وكفاءة النظام المقترح.
الكلمات المفتاحية: مركبة كهربائية متعددة المصادر، عاكس متعدد المستويات، تحكّم متقدّم، محرّك متزامن بمغناطيسات دائمة، خلية وقود، مكثّفات فائق

Résumé- Les véhicules électriques (VEs) suscitent un intérêt croissant en tant que solution prometteuse face à la crise énergétique et aux enjeux environnementaux. Actuellement, les VE utilisent une grande variété de dispositifs d'électronique de puissance pour fournir l'énergie nécessaire au moteur, tout en assurant un fonctionnement efficace à des niveaux de tension élevés. Dans ce contexte, les onduleurs multi-niveaux ont été développés afin de surmonter les limites des convertisseurs conventionnels. Cette thèse a pour objectif de développer une nouvelle structure multi-niveaux, visant à améliorer les performances des véhicules électriques alimentés par plusieurs sources d'énergie. Le travail porte notamment sur l'étude d'une nouvelle topologie hybride asymétrique d'onduleur à 21-niveaux, caractérisée par une commutation réduite, dans le but d'optimiser la qualité de la tension de sortie et, par conséquent, les performances globales du VE. L'onduleur proposé est conçu pour alimenter un moteur synchrone à aimants permanents (MSAP). Le contrôle du moteur est d'abord assuré par une commande en mode glissant, la technique (SMC) est trés prisée car elle permet de rejeter efficacement les variations internes des paramètres ainsi que les perturbation extérieurs. Toutefois, en raison des limitations de cette méthode, notamment le phénomène de broutement (chattering), une technique améliorée a été développée : la commande en mode glissant flou hybride (HFSMC), permettant de réduire significativement ce phénomène. Le système global du VE est alimenté par deux sources d'énergie : une pile à combustible en tant que source principale, et un super-condensateur en tant que source secondaire. Des simulations ont été réalisées pour évaluer les performances de la nouvelle topologie d'onduleur, notamment en ce qui concerne l'amélioration de la qualité de la tension de sortie et la réduction du taux de distorsion harmonique total (THD). Une autre série de simulations a également été menée sur le système complet du VE. Les résultats obtenus ont démontré la fiabilité et l'efficacité du système proposé.
Mots clés : Véhicule électrique multi sources, onduleur multi niveaux, commande avancée, moteur synchrone à aimants permanents, pile à combustible, super-capacités.

Abstract- Electric Vehicles (EVs) are gaining increasing attention as a viable solution to the ongoing energy crisis and environmental concerns. Modern EVs integrate a wide range of power electronic devices to deliver the required energy to the motor while ensuring efficient operation at high voltage levels. In this context, Multilevel Inverters have been developed to address the limitations of conventional power converters. This research aims to a novel multilevel inverter architecture, with the objective of enhancing the performance of EVs powered by multiple energy sources. The study specifically focuses on a new 21-level asymmetric hybrid inverter topology, which features reduced switching frequency, with the goal of improving output voltage quality and thereby optimizing the overall performance of the electric vehicle. The proposed inverter is designed to supply a Permanent Magnet Synchronous Motor (PMSM). The motor is initially controlled using Sliding Mode Control (SMC), a widely adopted technique because of its Robust performance against variations in internal parameters and external disturbances. However, due to certain limitations of this method—particularly the chattering phenomenon—an improved control strategy has been developed: the Hybrid Fuzzy Sliding Mode Control (HFSMC), which significantly reduces chattering effects. The overall EV system is powered by two energy sources: a fuel cell as the primary source, and a super-capacitor as the secondary source. Simulations were conducted to evaluate the performance of the new inverter topology, particularly in terms of improving output voltage quality and reducing the Total Harmonic Distortion (THD). An additional set of simulations was also carried out on the complete EV system. The results demonstrated the reliability and effectiveness of the proposed system.
Keywords: Multi-source electric vehicle, multi-level inverter, advanced control, permanent magnet synchronous motor (PMSM), fuel cell, super-capacitors.

Table of Contents

Nomenclature

EV	Electric Vehicle
BEV	Battery Electric Vehicle
HEV	Hybrid Electric Vehicle
PHEV	Plug-in Hybrid Electric Vehicle
FCEV	Fuel Cell Electric Vehicle
LPG	Liquefied Petroleum Gas
CNG	Compressed Natural Gas
ICE	Internal Combustion Engine
DCMD	Direct Current Motor Drives
IMD	Induction Motor Drives
PMSMD	Synchronous Motor Drives
VRMD	Variable Reluctance Motor Drives
SC	Super-capacitor
EDLC	Electric Double Layer Capacitor
BMS	Battery Management System
ECE-15 UDC	Urbain Drive Cycle
EUDC	Extra Urbain Drive Cycle
NEDC	New European Driving Cycle
PMSM	Permanent Magnet Synchronous Machine
NPC	Neutral Point Clamp
FC	Flying Capacitor
CHB	Cascaded H-bridge
SPWM	Sinusoidal Pulse Width Modulation
PD-PWM	Phase Disposition PWM
POD-PWM	Phase Opposition Disposition PWM
POD-PWM	Phase Opposition Disposition PWM
APOD-PWM	Alternate Phase Opposition Disposition PWM
PS-PWM	Phase Shifted PWM
THD	Total Harmonic Distortion
SMC	Sliding Mode Control

VSS	Variable Structure System
FLC	Fuzzy Logic Control
FSMC	Fuzzy Sliding Mode Control

List of Symbols

F_{ad}	Aerodynamic resistance
F_{sf}	Stokes or viscous drag force
F_{ro}	Rolling resistance force
F_{cr}	Climbing resistance force
m	The mass of the vehicle
C_d	The factor of tire rolling drag
p	The air density
V_w	The wind speed
A_f	The frontal surface area of the vehicle
C_f	Coefficient of drag
λ	The mass factor
J	The moment of inertia
i	The gearbox ratio
r	The wheel radius
F_{tr}	Tire traction force
K_m	Rotational coefficient of inertia
m_i	Inertia mass of the vehicle
φ_f	The amplitude of the flux produced by the permanent magnets
θ	The electrical angle
θ_m	The mechanical position of the rotor relative to the stator
L_{s0}	The leakage inductance
L_m	The magnetizing inductance
L_{ss}	The self-inductance
M_{ss}	The mutual inductance
V_{fc}	Fuel cell voltage
E_{nerts}	The Nerst tension
v_{act}	The activation over-voltage
v_{ohm}	The ohmic over-voltage
v_{conc}	The concentration over-voltage
t_m	The thickness of the membrane

σ_m	The conductivity of the membrane
I_{st}	The stack current
C_{eq}	The equivalent capacitance of the SC pack
N_{psc}	The number of parallel branches of SC_s
N_{ssc}	The number of series connections of SC_s
n	Reduction ratio
m	The modulation index
r	The modulation rate
α	The duty cycle
u_1	Control signal of switch K_1
u_2	Control signal of switch K_2
T	Number of transistors (power switches) used in the topology
D	Number of required diodes.
m	Number of DC sources (depending on the topology)
u	Control input
u_{eq}	Corresponds to the equivalent component
u_N	Corresponds to the nonlinear component (discontinuous control input)
$\mu_A(x)$	Membership function
de	Error change

List of Figures

Chapter 1: State of Art of Electric Vehicles

Chapter 2: Modeling of the Traction Chain Elements

Chapter3: A New Multilevel Inverter Topology with Less Switching Devices for Electric Vehicle Applications

Chapter 4: Nonlinear Control for Electric Vehicle Traction

List of Tables

Chapter 1: State of Art of Electric Vehicles

Chapter 3: A New Multilevel Inverter Topology with Less Switching Devices for Electric Vehicle Applications

Chapter 4: Nonlinear Control for Electric Vehicle Traction

GENERAL INTRODUCTION

General introduction

The increasing challenge of global heating and air pollution from urban transportation has driven the advancement of different approaches to mobility, including electric vehicles (EVs), car sharing, and e-bikes [1]. EV presents multiple benefits: electric energy is more affordable and environmentally friendly compared to oil, electric motors are more efficient than internal combustion engines, EV operate more quietly, and they can be charged at home [2]. Consequently, this remains essential for the research community to prioritize clean, renewable, and environmentally friendly energy sources and to encourage policy and economic leaders to take decisive action to tackle this issue and facilitate the shift to renewable energy [3]. In this situation, the growing presence of EV in a fiercely competitive market drives car manufacturers to create more fuel-efficient automobiles at lower expenses. Key performance criteria for EV encompass reliability, resilience, energy control, battery charging rate, and especially the electric drive system [4].

EV typically utilize large electric engines that necessitate a significant quantity of batteries and sophisticated power electronic converters to supply the necessary high-level electrical power they require. The structure of multilevel inverters enables the synthesis of high-quality, high-voltage waveforms, making them ideal for high-power drive systems [5].

In electric vehicle (EV), traditional cascaded multilevel inverters are widely utilized to drive permanent magnet synchronous motors (PMSM). However, these inverters exhibit high total harmonic distortion (THD), failing to meet IEEE standards while offering lower power conversion efficiency. Additionally, they cause higher voltage stress across control devices, and every section must be separated from high electromagnetic interference through appropriate isolation transformers [6]. PMSM-based EVs currently use these inverters, which adversely affect the performance and output quality of the PMSM, as identified by advanced sensors [7]. Key factors affecting motor performance include: 1- Uneven torque generation caused by unbalanced voltage, 2- Magnetic saturation and unequal air gaps due to winding space harmonics, which induce opposite voltage-circulating harmonic currents, 3- Significant power losses, oscillations, increased temperature, and vibrations arising from higher-order harmonics, 4- Finally gradual deterioration in motor efficiency and lifespan [8].

To address these issues, PMSMs should operate with nearly sinusoidal waveforms, even when powered by a DC source. While filters can generate sinusoidal output from DC sources, they increase in size and cost when power quality requirements are high. A more effective solution is employing multilevel inverters, which convert DC to sinusoidal AC with reduced THD [9]. Multilevel inverters represent state-of-the-art technology during power conversion, and their utilization has grown significantly compared to conventional inverters. They are widely applied in various domains, including industrial systems, grid-connected systems, solar PV systems, and electric vehicles [10]. Traditional multilevel inverters are categorized into three main types: neutral-point clamped (NPC) inverters, flying capacitor (FC) inverters, and cascaded H-bridge (CHB) inverters. The main disadvantage of NPC and FC inverters is their dependence on a large number of clamping diodes and flying capacitors to boost the number of output voltage levels. In contrast, Inverters with H-bridges are more widely used and favored over other types. Multilevel cascaded inverters are categorized into symmetric and asymmetric types. In the symmetric configuration, every DC-link values are identical, whereas, in the asymmetric configuration, the DC-link values vary. However, a significant drawback of cascaded multilevel inverters is the high number of DC-links and power switches required. In recent decades, researchers have made significant efforts to develop optimal topologies for both symmetric and asymmetric cascaded multilevel inverters [11]. Each topology possesses unique characteristics, making it appropriate for specific applications. Novel topologies are developed by modifying the fundamental designs to serve specific objectives. Some aim on minimizing the number of power switches, while others focus on minimizing the number of DC-links or achieving other objectives [12]. Despite significant efforts by researchers on multilevel inverters, there remains potential to introduce novel optimum topologies to further expand the output voltage levels' number.

Asymmetric multilevel inverters are viewed as an effective solution for overcoming the limitations of traditional multilevel inverters. These converters utilize different input voltage levels for various components and modules, enabling the combination and subtraction of these voltages to create multiple voltage levels while minimizing the number of semiconductor switches needed.

The development of batteries as an energy source remains constrained by inherent limitations such as low energy density, extended charging durations, and high production costs. To address these challenges, a viable alternative involves the generation of clean energy in adequate quantities to meet the demands of electric vehicle operation. This can be achieved through the integration of fuel cells, super-capacitors, or a hybrid configuration of these technologies, an architecture particularly advantageous for urban transportation applications.

Consequently, energy management is optimized to enable energy distribution among the propulsion system components, along with the appropriate selection of the engine.

The Synchronous Motor with Permanent Magnets (PMSM) is widely used in EV energy propulsion systems because of its numerous advantages, such as its efficient compact structure, high air-gap flux density, high energy density, favorable torque-to-inertia ratio, and excellent performance effectiveness. The PMSM necessitates an effective management strategy, meaning it demands a rapid and precise response, swift recovery from disturbances, and robustness against variations in parameters. As a result, numerous contemporary control techniques, including sliding mode control (SMC), have been advocated to enhance the performance of the PMSM [13]. SMC technique is a popular technique because it effectively rejects internal parameter changes and outside disruptions. SMC has discovered vast application in electrical power systems and electrical devices for machines [14]. Consequently, it has been effectively utilized for controlling the position and speed of PMSMs.

Nonetheless, Sliding Mode Control (SMC) presents a significant limitation: the chattering effect, which arises from the coupling of parasitic system behavior with high-frequency switching control [15]. To address this issue, various advanced control strategies have been proposed with the aim of attenuating or entirely suppressing chattering. Among these, Hybrid Fuzzy Sliding Mode Control (HFSMC) has emerged as a promising solution. Fuzzy Sliding Mode Control [16] is considered one of the most widely adopted approaches, as it integrates the robustness of sliding mode control with the adaptability of fuzzy logic systems.

Thesis Objective

This work aims to contribute to the development of a new three phase 21-asymmetric multilevel inverter with reduced number of electronic switching elements that uses phase opposition disposition pulse width modulation (PD-PWM) for powering

electric propulsion system of electric vehicle (EV). This system consists of three main subsystems: power supply, auxiliary systems, and propulsion by electric motors Synchronous Permanent Magnet Motor (PMSM) with a nominal power of approximately 50 kW and a maximum torque of 255 Nm. Our traction system requires control laws that are insensitive to disturbances, parameter changes, and nonlinearities.
This thesis is composed of four chapters presented as follows:

In the first chapter, we present a state-of-the-art overview on the evolution of electric vehicles, focusing on emerging technical and technological challenges, and the various powertrain technologies best suited for automotive applications.

Within chapter two, we develop a mathematical model for the forces acting on the vehicle and then model the internal components of each subsystem (PMSM engine, fuel cell, super-capacitor, and DC/AC converters), offering an approximate understanding of the control strategies to be implemented.

In the third chapter, we present the modeling of DC/DC static converters used to interface the various energy sources embedded in the hybrid system: the fuel cell and the super-capacitor. These converters play a fundamental role in energy management by ensuring proper voltage adaptation between the sources and the DC bus, as well as effective control of power transfer. A new asymmetric hybrid multilevel inverter with a reduced number of components is presented. This topology was evaluated through simulation with the aim of reducing the Total Harmonic Distortion (THD) and thereby assessing the quality of the generated output voltage.

Chapter four is dedicated to the control of the proposed traction system, which consists of a (PMSM) powered by an asymmetric 21-level inverter. The motor control strategy is based on Sliding Mode Control (SMC), which is presented in detail.
To address the chattering issue commonly associated with SMC, a hybrid control approach combining Fuzzy Logic and Sliding Mode Control is then introduced. The simulation test results of the overall system (MATLAB Simulink) will be conducted to analyse the system's dynamic performance and its efficiency, both in terms of tracking and robustness.

Chapter 1: State of Art of Electric Vehicles

1.1 Introduction

The majority of existing vehicles are conventional, depending solely on petroleum as their energy source. The dwindling global supply of petroleum, a pressing international concern, is leading to elevated fuel costs that severely impact operators of traditional vehicles. Additionally, traditional vehicles emit greenhouse gases, making it more difficult to adhere to strict environmental regulations.

The transportation sector is a cornerstone of the global economy and a fundamental part of modern society, deeply influencing lifestyles, recreational pursuits, and worldwide environmental conditions. Its evolution since the beginning of the 20th century has profoundly reshaped the world. This sector is heavily dependent on petroleum, accounting for more than one-fifth of global energy consumption and, since the late 1990s, has been the largest consumer of oil compared to all other sectors. In light of escalating worldwide energy needs, the urgent challenges of fossil fuel depletion, and the pressing issue of climate change, advancing clean energy alternatives has become an critical imperative [17].

In this context, automotive manufacturers and researchers are succeeding in making conventional vehicles cleaner by equipping them with new, more environmentally friendly components. The introduction of these novel technologies has resulted in a notable decrease in emissions of pollutants like SO_2, CO, total hydrocarbons (HC), NOx, and particles, facilitating adherence to current standards [18].

While the electric vehicle (EV) is considered the pinnacle of automotive advancement, its capabilities are currently limited by battery technology. As a result, hybrid electric vehicles (HEVs) offer a more viable and immediate substitute for traditional vehicle, and will likely remain a practical choice for the foreseeable future.

We are interested in this latter solution, which will enable a gradual transition from conventional vehicles to cleaner ones. For this, the control of the powertrain, the storage of electrical energy, and optimized energy management are key points [19]. This chapter begins with a general overview of electric vehicles, covering their definition and a broad description of the traction system, including electric motors, energy sources, and static converters. Finally, we provide insights into mobility and the different driving modes used.

1.2 Problematic

These days, CO_2 emissions from transportation represent 30% of total global emissions [20]. Indeed, transportation is the main cause of greenhouse gas emissions and the majority of urban pollution (whether atmospheric or noise-related). Currently, over 80 percent of the world's energy needs are met by fossil fuels, namely , natural gas, coal and oil, and there is currently no immediate alternative capable of completely satisfying our requirements. As illustrated in Figure1.1, oil remains the foremost primary energy source worldwide, comprising 36% of consumption in 2002, approximately equivalent to 3.8 billion tonnes of oil (Gtep). The transportation sector clearly emerges as the primary sector in terms of petroleum product consumption, currently holding a share of 50% Figure 1.2, compared to 42% in 1973. Consequently, CO_2 emissions continue to rise. Furthermore, the anticipated depletion of fossil fuels and climate change represent major risks for centuries to come. These figures have alerted automotive manufacturers to the necessity of creating new individual transportation methods that integrate novel types of clean and energy-efficient propulsion systems. In response, new technologies have emerged, while others remain in development and are expected to be fully utilized only in the coming years.

The future of automotive progress extends beyond alternative fuels (liquefied petroleum gas (LPG), biofuels, and compressed natural gas) to prioritize electricity-driven solutions, specifically EVs, battery electric, and fuel cell EVs.

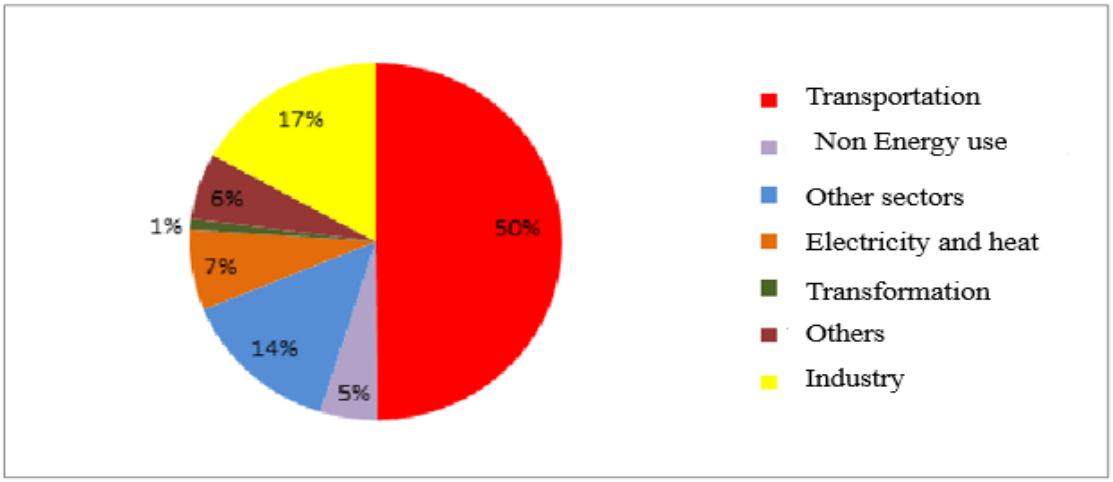

Figure 1.1. Worldwide petroleum product consumption [20].

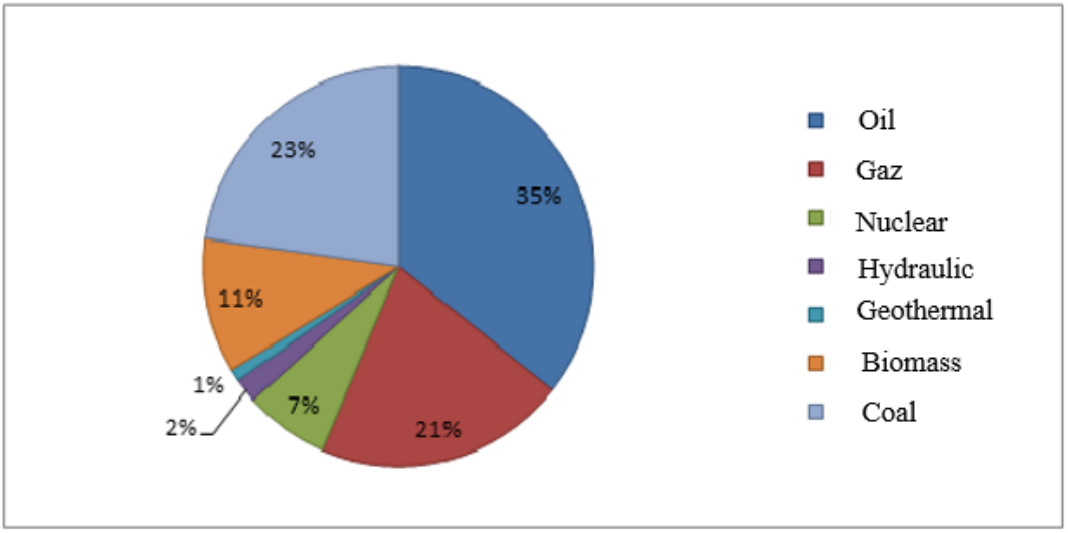

Figure 1.2. Worldwide primary energy consumption [20].

1.3 Definition of an electric vehicle

An EV operates exclusively on electric power, utilizing one or more electric motors for propulsion. The motor's rotational force is transmitted directly to the wheels, with the specific drivetrain configuration varying by design. Ongoing advancements in power electronics and energy management systems are fostering continuous innovation and novel engineering approaches to enhance this method of transportation [21]. All these explorations are related to a common issue: the production, transportation, storage, and utilization of electricity.

The electric propulsion system is the main component of the electric vehicle, it is electrically powered by motors and includes a transmission system formed by one or more electric motors driving a wheels.

1.4 History of electric vehicles

The inception of the EV traces its origins to the third decade of the 19th century. Its inventor was Robert Anderson, a Scottish businessman. It resembled more of an electric carriage [22]. Around 1835, Thomas Davenport, an American, constructed a diminutive electric locomotive.

Around 1838, the Scottish inventor Robert Davidson introduced a similar model capable of reaching speeds of up to 6 km/h. Neither of these inventors utilized rechargeable batteries.

The invention of the rechargeable lead-acid battery is attributed to Gaston Planté of France in 1859, later refined by Camille Faure in 1881. Figure 1.3 illustrates Thomas Parker seated in an electric vehicle, possibly the world's inaugural one, circa 1884. This compact vehicle relied on a non-rechargeable battery and was capable of traveling a brief distance on rails [23]. By 1891, American William Morrison had constructed the first authentic electric vehicle.

Figure 1.3. First rechargeable battery electric vehicle [24].

Figure 1.4. First true electric vehicle in 1891 [24].

In 1896, Andrew Riker's "Electric Riker" won an automobile race. By 1897, the first electric taxis were spotted on the streets of New York.

Figure 1.5. The riker electric [25].

Figure 1.6. Electric vehicle never satisfied [25].

In 1899, a Belgian company built "La Jamais Contente," marking the first electric vehicle to surpass 100 km/h (reaching 105 km/h). Piloted by Belgian Camille Jenatzy, the torpedo-shaped vehicle was outfitted with Michelin tires.

In 1900, VEs were more popular than ever, making up over a third of all road-going vehicles and rivaling both steam and gasoline-powered automobiles. In 1902, "La Phaeton de Wood" could cover 29 kilometers at a speed of 22.5 km/h, priced at $2000. By 1912, electric vehicle production had reached its zenith. Nevertheless, the arrival of the gasoline-powered "Ford Model T" in 1908 started to make an impact. "The Anderson Electric Car Company" revealed its model in Detroit in 1918.

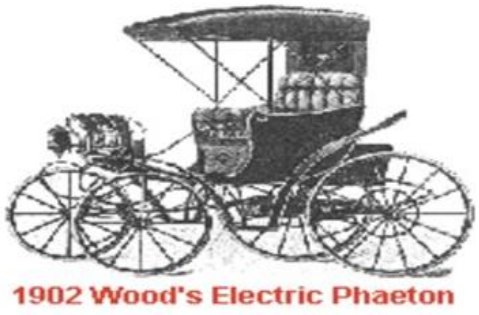

Figure 1.7. 1902 Woos's electric phaeton [24].

Figure 1.8. The detroit electric [24].

In the 1920s, several factors contributed to the decline of the EV. These included their limited range, low speed, lack of power, the availability of petroleum, the challenge of electric energy recharge, and their price [26], which was twice as high as gasoline Fords.

A 1966 act of the U.S. Congress promoted the creation of electric cars as a strategy to mitigate air pollution [27]. American public opinion was largely supportive, and with the increase in gasoline prices in 1973 (the first oil shock: the embargo of the OPEC against the United States), the timing was right. However, nothing really took off.

In 1972, Victor Wouk, considered the father of the hybrid vehicle, built the first hybrid vehicle, General Motors' "Buick Skylark." In 1974, "The Vanguard-Sebring CitiCar," resembling a golf cart, appeared at the Electric Vehicle Symposium in Washington D.C. It could travel 64 kilometers at a speed of 48 km/h.

Figure 1.9. First hybrid vehicle in 1972

Figure 1.10. Vanguard-sebring citicar [28]

To stimulate progress in alternative vehicle technology, the U.S. Congress passed a 1976 act funding research and demonstration projects for advanced batteries, engines, and hybrid powertrain systems. Starting in 1988, GM's President, Roger Smith, launched a research fund aimed at developing a new electric vehicle, eventually named the "EV1."

Figure 1.11. L'EV 1 [28].

During the 1990s, several major car manufacturers developed HEV prototypes as a strategy to improve the poor fuel efficiency of their standard gasoline-powered cars. Early concepts included models from Ford, General Motors, Renault, and Volkswagen.

The most significant developments are the Toyota Prius (Figure 1.12) and the Honda Insight (Figure 1.13), which were the first commercially available HEVs in 1997, thus holding historical value in the field of individual transportation.

Figure 1.12. Toyota Prius XW10.

Source : http://malaysiapriusclub.webs.com/photos/Toyota-Prius-XW10-1stGeneration/ui4KdhiEYv3u2EWVU8BvIc.jpg

Figure 1.13. Honda Insight I.

Source:http://upload.wikimedia.org/wikipedia/commons/thumb/9/9a/Honda_Insight_.jpg/280pxHonda_Insigh t_.jpg

1.5 Types of an electric vehicles

The most basic type of EV relies exclusively on batteries for its energy, but there are other types that can utilize different energy sources. These are referred to as hybrid EVs (HEVs). The International Electro technical Commission's Technical Committee 69 (Electric Road Cars) recommended that vehicles using two or more types of energy sources, storage systems, or converters be classified as HEVs, provided that at least one source supplies electrical energy [29]. This definition covers a wide range of HEV pairings, such as an internal combustion engine (ICE) with a battery, a battery with a

flywheel, a battery with a capacitor, and a battery with a fuel cell. As a result, the public and professionals started referring to cars with an ICE and an electric motor as HEVs, those with a battery and a capacitor as ultra-capacitor-assisted EVs, and those with a battery and a fuel cell as FCEVs. This terminology has become widely accepted, and EVs are now classified as follows:

- Battery Electric Vehicle (BEV)
- Hybrid Electric Vehicle (HEV)
- Plug-in Hybrid Electric Vehicle (PHEV)
- Fuel Cell Electric Vehicle (FCEV)

1.5.1 Battery electric vehicle (BEV)

These vehicles use batteries as their primary energy source, which can be recharged from the electrical grid or other renewable sources such as solar and wind power. The range of these vehicles is directly dependent on the battery capacity. Typically, they can travel 100 to 250 km on a single charge, with high-end models capable of reaching distances between 300 and 500 km [30]. These ranges are influenced by driving conditions and style, vehicle configuration, road conditions, climate, battery type, and age. Once depleted, recharging the battery takes significantly longer than refueling a conventional ICE vehicle. Some batteries can take up to 36 hours to fully recharge [31]. While others require much less time, but none can match the quick refueling time of a fuel tank.

Charging time depends on the configuration of the charger, its infrastructure, and the operating power level. BEVs offer advantages such as simple construction, ease of operation, and convenience. They do not emit greenhouse gases (GHGs) or produce noise, making them environmentally friendly. Electric propulsion delivers immediate and high torque, even at low speeds. These benefits, coupled with their limited range, render them well-suited for urban use. The Nissan Leaf and Tesla, along with some Chinese vehicles, are currently popular BEVs. Figure 1.14 illustrates the fundamental setup of BEVs: the wheels are propelled by one or more electric motors, which draw power from batteries through a power converter circuit.

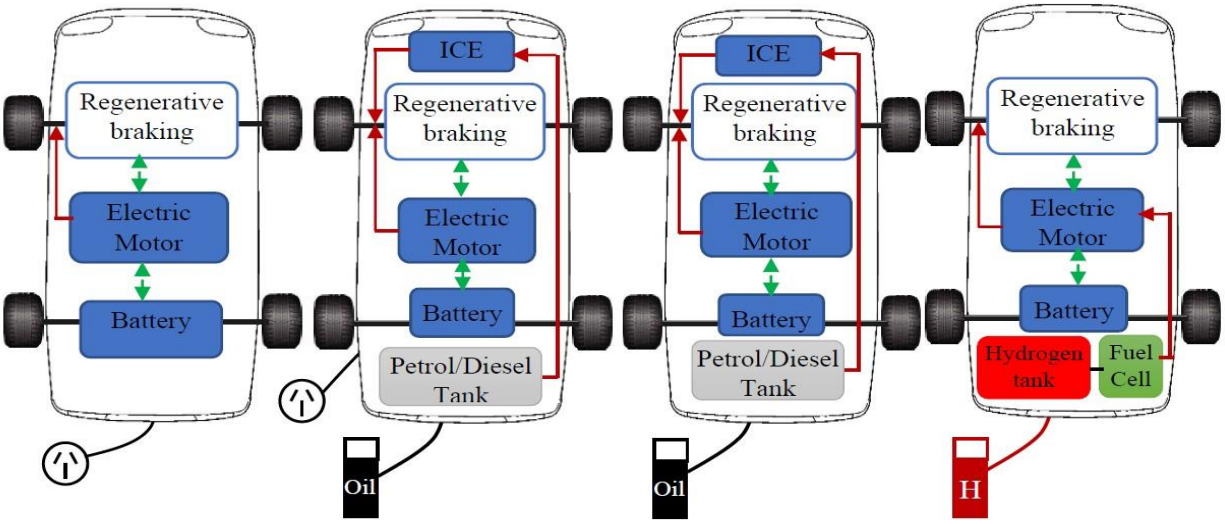

Figure 1.14. Types of electric vehicles.

1.5.2 Hybrid electric vehicle (HEV)

HEVs employ both a conventional internal combustion engine and an electric propulsion system. The internal combustion engine serves as the primary power source, while the electric motor primarily aids in improving fuel efficiency. To recharge their vehicle batteries for propulsion, HEVs depend on their internal combustion engines and regenerative braking systems, as they cannot be directly connected to the grid for recharging [32].

An HEV utilizes the electric drive system during periods of low power demand. This is a great advantage in low-speed scenarios like urban areas, as it reduces fuel consumption by keeping the engine completely off during idle periods, such as in traffic jams, thus lowering greenhouse gas emissions. When higher speeds are necessary, the HEV transitions to the internal combustion engine. The two powertrains can also work together to improve performance by bridging shift gaps and boosting speed when necessary, thereby also improving driving efficiency. To achieve these features, power management strategies are implemented. For example, upon vehicle startup, the internal combustion engine can operate as a generator to produce energy, which is then stored in the battery. During overtaking maneuvers, which demand increased speed, both the internal combustion engine and the electric motor drive the powertrain. When braking, the powertrain functions by turning the engine akin to a generator, thus charging the battery through regenerative braking. At cruising speed, the internal combustion engine

operates the vehicle while also acting as a generator to charge the battery. The flow of energy ceases when the vehicle comes to a stop [33].

1.5.3 Plug-in hybrid electric vehicle (PHEV)

The concept of PHEVs emerged to enhance the all-electric range of HEVs [34]. Similar to HEVs, PHEVs employ both an internal combustion engine and an electric powertrain. However, the significant difference is that PHEVs primarily depend on electric propulsion as the primary driving force, requiring a larger capacity battery compared to HEVs. PHEVs usually start in "all-electric" mode, operating exclusively on electricity. As the battery charge depletes, they transition to using the internal combustion engine to either provide a boost or recharge the battery pack. The internal combustion engine is employed here to extend the range. Unlike HEVs, PHEVs have the capability to recharge their batteries directly from the electrical grid; they also utilize regenerative braking [35]. PHEVs' ability to predominantly operate on electricity reduces their carbon footprint compared to HEVs. Additionally, they consume less fuel, resulting in reduced associated costs. The automotive market is now abundant with these vehicles, with sales of models like the Chevrolet Volt and Toyota Prius attesting to their popularity.

1.5.4 Fuel cell electric vehicle (FCEV)

FCEVs, also known as fuel cell vehicles (FCVs), derive their name from the fact that their core components are fuel cells, which generate power through chemical reactions [36], Because hydrogen is the preferred fuel for these vehicles to catalyze this reaction, they are often referred to as "hydrogen fuel cell vehicles." Hydrogen is transported in specialized high-pressure tanks by fuel cell trucks. Another crucial element in the power generation process is oxygen, sourced from the surrounding air. The fuel cells produce energy, which then powers an electric motor responsible for propelling the wheels. Any surplus energy is stored in devices such as batteries or super-capacitors [37]. As a result of their power generation process, FCEVs only emit water as a byproduct, which is released from the vehicle through the tailpipes. Figure 1.14 illustrates the configuration of an FCV. An advantage of these vehicles is their ability to generate carbon-free power, minimizing their carbon footprint more effectively than any other EV. Another noteworthy advantage, perhaps the most crucial at present, is that

recharging these vehicles takes no longer than refueling a traditional vehicle at a gas station. This factor enhances the likelihood of these vehicles being adopted in the near future [38]. The limited availability of hydrogen fuel stations poses a significant current challenge to the widespread adoption of this technology, although BEV or PHEV charging facilities were not widely available until recent years. Another drawback, highlighted by a study conducted by the United States Department of Energy (DOE), is the high cost of fuel cells, which can exceed $200 per kW, significantly more expensive than internal combustion engines (typically less than $50 per kW) [39]. Moreover, safety concerns emerge in the event of potential explosive hydrogen leaks from the tanks. If these obstacles were addressed, FCVs could indeed represent the future of automobiles. Table 1.1 offers an overview of typical vehicles in the industry along with their primary characteristics [39].

Table 1.1: Typical electric vehicles and their main characteristics [8].

Vehicle Model	Peugeote 208	Citroen Ami	Toyota Prius	Mitsubishi outlander	Toyota Mirai
Release Year	2022	2020	2018	2018	2018
Type	BEV	BEV	HEV	PHEV	FCEV
Entry price (€)	33000	7000	32300	37000	78900
Battery size (kwh)	46	5.5	1.3	13.8	1.6
Fossil-fuel autonomy (km)	0	0	500	550	650
Electric autonomy (km)	450	75	0	55	0
CO2 emissions (g/kg)	0	0	106	46	0

1.6 Structure of an electric vehicle powertrain

The central element of electric vehicles that distinguishes them from conventional vehicles is the electric drivetrain, which uses batteries for storing electrical energy, a motor to convert the stored electrical energy into mechanical energy, and an electric converter (inverter) to transform the direct current supplied by the batteries into alternating current to power the motor.

These converters rely on complex power electronics structures, particularly used in controlling the variable speed of the motors.

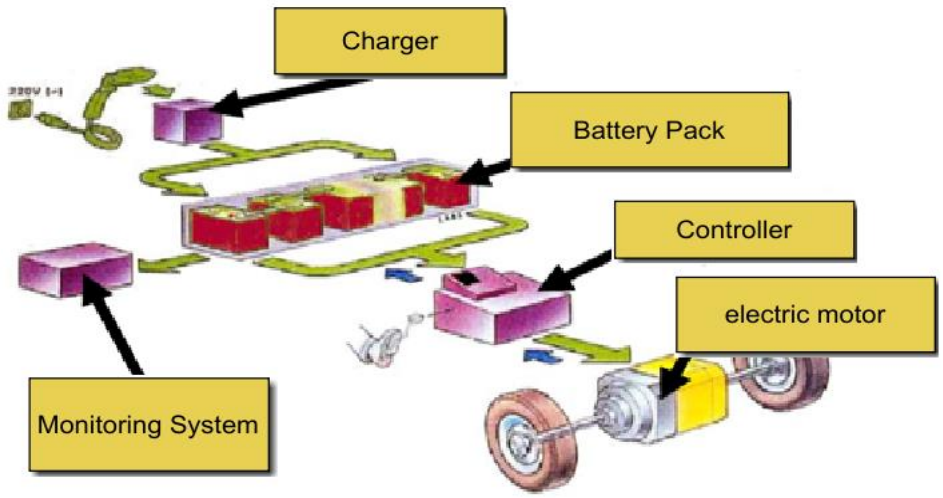

Figure 1.15. Components of an electric vehicle.

The basic configuration of an electric drivetrain comprises a battery, an inverter (power electronics), and an electric motor. The battery supplies direct current (DC), which is passed to the inverter. The inverter converts the DC into alternating current (AC) and delivers it to the electric motor. The electric motor then converts the electrical energy into mechanical energy. This process can be reversed, allowing the electric motor to serve as an electric brake. The electric motor then functions as a generator, converting braking energy into electrical energy, which is stored in the battery via the inverter. This process is called regeneration [40].

In the non-propulsion electrical system, there are distinct high-voltage and low-voltage branches. The high-voltage branch connects to the heating and cooling auxiliaries. The low-voltage branch is powered by a DC/DC converter, which ensures the 12V battery is adequately charged and supplies power to all 12V auxiliaries, such as lighting, radio, and navigation [28]. The components of an electric vehicle are illustrated in Figure 1.15

Another component, far less familiar to the average person, is the battery monitoring system. This system enables the determination of the battery pack's state of charge, consequently facilitating the estimation of the vehicle's range.

This monitoring system becomes more complex with battery technology advancements. Lithium batteries require very specific monitoring to avoid exceeding certain voltage thresholds in order to prevent battery degradation and hence extend its lifespan. These monitoring systems utilize the « Battery Management System » (BMS) [41].

1.7 Electric engines

Electric motors usually consist of a rotor, the moving part, and a stator, the stationary part. They produce motion by harnessing the interaction between a magnetic field and conductors that carry current, making use of the Lorentz force [42].

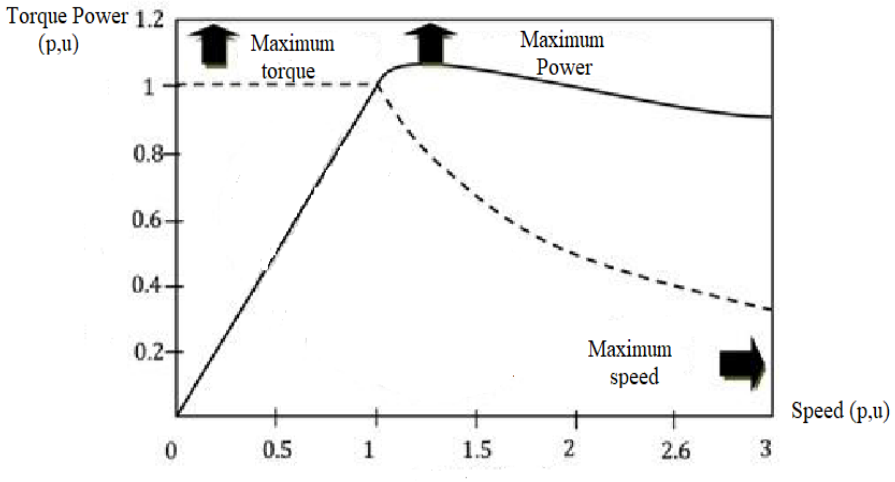

Figure 1.16. Torque/power-speed required for EV [43].

In electric vehicles, the electric motor functions as the primary propulsion source. However, in hybrid electric vehicles, the electric motor and the internal combustion engine operate either in series or in parallel, collectively supplying the propulsion power. In an electric or hybrid vehicle, the electric traction motor transforms the electrical energy stored in the energy storage unit into mechanical energy, propelling the vehicle's wheels. The main advantages of an electric motor compared to an internal combustion engine are its ability to deliver full torque at low speeds and its potential for instantaneous rated power that can be two to three times greater than that of the combustion engine.

The performance of an electric vehicle hinges on the propulsion motor it employs. When it comes to an electric vehicle, once the driver releases the accelerator, the drive wheels slowly feedback the vehicle's kinetic energy to the electric motor, which transforms into a generator, recharging the batteries. Specifically, the choice of the

propulsion electric motor and its power transmission is primarily dictated by the following operational traits [43].

-Ensuring uphill starting capability of the EV (high torque).

-Reaching the highest speed possible

-A driving strategy that continuously optimizes energy consumption (efficiency aspect: high efficiency across different speeds).

These typical characteristics required for machines used in electric propulsion systems are well illustrated in Figure 1.16, showing the evolution of torque/power-speed. So far, four types of propulsion have been applied to EVs. These are direct current motor drives (DCMD), induction motor drives (IMD), permanent magnet synchronous motor drives (PMSMD), and variable reluctance motor drives (VRMD). Table 1.2 summarizes the most important characteristics of each engine, its drawbacks, and the type of vehicle used in it [44].

Table 1.2: Types of electric engines used in EVS [8].

Motor type	Advantage	Disadvantage
direct current motor (DCMD) 	-It benefits from a high level of industrial maturity -Its control is very simple, as is its power supply. -Established manufacturing technology.	-The brushes require regular maintenance. - It is limited in torque.
Induction Motor (IMD) 	- The most advanced commutator-free motor drive system -Can be operated similarly to a separately excited DC motor by utilizing field orientation control.	

Permanent Magnet Synchronous Motor (PMSM)	-Capable of operating at various speed ranges without the need for gear systems	
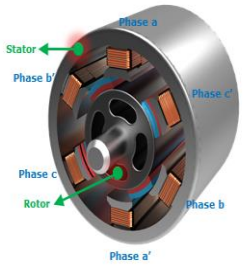	-Compact	- Significant iron loss at high speeds during in-wheel operation
	-Efficient	
	-Produces high torque even at very low speeds	

1.8 Energy storage system in electric vehicles

Electric vehicles, encompassing hybrids and battery-electric models, are poised to become the predominant choice in the clean vehicle market in the near future. It's projected that by 2020, over half of all new vehicle sales will be electric [45]. Energy storage technology stands as the pivotal factor enabling this transformative shift. Energy storage is considered the heart of an electric vehicle. Several parameters of energy storage are taken into consideration in an automotive application, such as specific energy, specific power, efficiency, maintenance requirements, management, costs, environmental adaptability, user-friendliness, and safety. For allocation in an electric vehicle, specific energy is the primary consideration as it limits the vehicle's range. Various forms of energy storage have been suggested and utilized for both electric and hybrid vehicles. Currently, these storage solutions primarily consist of chemical batteries, super-capacitors, and fuel cells. It's crucial for electrical engineers to grasp the fundamental principles of these diverse energy sources and the unique demands they impose on the power supply systems for EVs.

1.8.1 Batteries

The traction batteries are used to power the propulsion systems of EVs, so advancements in traction battery technology greatly impact the EV industry. The introduction of commercially available rechargeable lead-acid batteries marked a

significant milestone in EV development. Over time, battery technology advancements have led to a proliferation of different types of traction batteries within the industry. Despite these advancements, the fundamental requirements for traction batteries have seen little change. Unlike starter, lighting, and ignition batteries, EV batteries must sustain continuous power delivery, necessitating increased energy capacity. Furthermore, high specific power, specific energy, and energy density are critical factors to consider [46].

Numerous battery technologies have emerged alongside the development of EVs, encompassing lead-acid, nickel-cadmium (Ni-Cd), lithium-ion (Li-Ion), lithium iron phosphate (Li-phosphate), lithium polymer (Li-Polymer), nickel-metal hydride (Ni-MH), zebras, and zinc-air batteries [15]. Among these, the Li-Ion battery is the most prevalent type used in EVs. Lithium-ion batteries offer various advantages, including a high power-to-weight ratio, superior energy efficiency, and robust performance at high temperatures. Furthermore, compared to other technologies, Li-Ion batteries exhibit a low "self-discharge" rate, allowing them to maintain a full charge over extended periods. Moreover, most components of Li-Ion batteries are recyclable, rendering this technology environmentally friendly.

Table 1.3 illustrates the commonly used battery technologies in electric vehicles [48]. A battery is characterized by the following three parameters:

Figure 1.17. Lithium-Ion battery of the Nissan electric car.

– Useful power ($P = V \cdot I$) in kW: The useful power is determined by multiplying the battery voltage (V) by its maximum current output (I). This useful power should be at least equal to the peak power requirement of the electric motor to ensure that it is adequately powered across its entire operational spectrum.

– Stored energy in kWh: This energy can be compared to the capacity of a vehicle's fuel tank. The stored energy will dictate the range of an EV and the potential for energy recovery in a hybrid car. The energy stored in an electric battery is determined by its capacity in ampere-hours (Ah) and its voltage.

– C-Rate (charge rate): Initially, the size of the battery is mainly influenced by its capacity (Ah) and charging current (A), which collectively define the battery's C-rate: the rate at which the battery's capacity is charged or discharged [29].

Table 1.3: Commonly used battery types [8].

Battery Type	Components	Advantages	Disadvantages
Lead-Acid	- Positive electrode: Lead oxide - Negative electrode: Spongy lead - Electrolyte: Diluted sulfuric acid	-Available in large-scale production - Low cost - Proven technology	- Discharge level cannot exceed 20% - Short lifespan - Limited energy and power density
Nickel-Metal Hydride (NiMH)	- Positive electrode: Alkaline solution - Negative electrode: Nickel Hydroxide -Electrolyte: Alloy of Nickel, Titanium, Vanadium and other Metals	- Twice the energy density of lead-acid Batteries - Safe operation at elevated voltages - Long life-cycle - Resistant to over-charging and deep discharge	- Reduced lifespan of 200-300 cycles if rapidly discharged under high load - Decreased usable power due to memory effect
	-Positive electrode: Oxidized Cobalt	-High energy density, twice that of NiMH.	- High cost

Lithium-Ion (Li-Ion)	material -Negative electrode: Carbon material -Electrolyte: Lithium salt solution in an organic solvent	-Excellent high-temperature performance. -Extended battery life, approximately 1000 cycles -High specific power.	- Lengthy charging Time , yet still Superior to other batteries
Nickel-Zinc (Ni-Zn)	- Positive electrode: Nickel oxyhydroxide - Negative electrode: Zinc	- Elevated energy density - Environmentally friendly - Suitable for use in a wide temperature range	- Rapid dendrite growth, which limits its use in vehicles
Nickel-Cadmium (Ni-Cd)	- Positive electrode: Nickel hydroxide - Negative electrode: Cadmium	- Extended lifespan - Can be fully discharged without damage - Recyclable	- Cadmium has the potential to be a pollutant - Expensive for use in vehicles

Battery prices vary widely because economies of scale can be triggered based on the total number of cars manufactured. As a result, battery costs might vary depending on the quantity of units manufactured Table 1.4.

Table 1.5 presents an overview on the existing EVs in the industry with their battery technology [49].

Table 1.4: Overview of battery costs at pack level for different BEVs [8].

Vehicle (€/kWh)	Model Year	Assumed Units Per Year	Pack Costs
BMW i3	2014	15,000	396
GM Bolt	2016	20,000	224
BMW i3	2017	25,000	254
Renault Zoe	2017	40,000	208
Tesla Model 3	2018	100,000	164
Audi e-tron	2019	100,000	157

Table 1.5: Overview on the existing EVs in the industry with their battery technology [8].

Manufacturer	Model	Autonomy (km)	Battery technology
Citroën	C-Zero	150	Lithium ion
Mia Electric	Mia	130	Lithium iron phosphate
Mitsubishi	I-MiEV	150	Lithium ion
Nissan	Leaf	160	Lithium ion
Peugeot	iOn	130	Lithium ion
Piaggio	Porter	100	Lead acid
Renault	Fluence ZE	185	Lithium ion
Renault	Kangoo	170	Lithium ion
Smart	Fortwo	145	Lithium ion
Tesla	Roadster	390	Lithium ion
Venturi	Fétish	340	Lithium polymer

1.8.2 Super-capacitor

Super-capacitors (SCs), also referred to as ultra-capacitors, have a construction similar to regular capacitors, yet they store energy in the form of an electrolyte solution situated between two solid conductors. SCs possess a notably larger capacity compared to conventional capacitors, allowing them to store up to 20 times more energy. SCs are classified into three types: electric double layer capacitors (EDLCs), pseudo-capacitors,

and hybrid capacitors. Despite variances in their energy storage methods and electrode materials, they share characteristics such as power density, life cycle, and energy efficiency. It's important to note that EDLCs have a lower specific energy density compared to the other two types (10e15 Wh/kg). The impressively high life cycle (1,105 cycles over approximately 40 years) distinguishes SCs from other energy storage devices. Additionally, SCs demonstrate high power density (1000e2000 kW/kg) and energy efficiency (84e97%). Consequently, they can be charged rapidly and discharge a substantial amount of energy with minimal energy loss. The main disadvantages of SCs include their short lifespan and high self-discharge rate, which is why they are not suitable for standalone power sources in vehicles. Another concern is the high capital costs (exceeding $6,000/kWh). Therefore, energy storage systems are best suited as backup energy sources for short-term energy storage applications [46], [47], [48].

Electric vehicles (EVs) often encounter start-stop scenarios, especially during urban driving, leading to significant variations in battery drain rates. While the typical power demand of batteries is minimal, there are instances, such as acceleration or hill climbing, where substantial power is required over short durations [50, 51]. In high-performance electric vehicles, peak power may be as much as sixteen times that of normal power [50]. Ultra-capacitors (UCs) are well-suited for such situations due to their ability to provide high power output for short periods. Additionally, they can rapidly capture energy from regenerative braking [51]. A combined battery/UC system, addresses each other's shortcomings, resulting in an efficient and reliable energy system. The low cost, load-leveling capabilities, temperature adaptability, and long lifespan of UCs make them an attractive solution [50].

Figure 1.18. Super-capacitor.

1.8.3 Fuel Cell

A fuel cell is an energy converter that directly and continuously transforms chemical energy into electrical energy through the chemical reaction between oxygen (O_2) and hydrogen (H_2), which is the reverse reaction of water electrolysis. A fuel cell differs from other electrochemical cells (or batteries) in that the reactants are continuously replenished and the products are continuously removed. In a traditional battery, the materials that make up the electrodes are consumable. Over time and with use, these materials degrade (the anode oxidizes and the cathode reduces), eventually causing the battery to become inactive: it is depleted.

In a fuel cell, the structure (electrodes, electrolyte, and reactive sites) does not react and remains unchanged over time, given certain precautions [52]. The energy flow delivered by the fuel cell is controlled by the circulation of the fuel gas (H_2) and the oxidizing gas (O_2), with simultaneous production of electricity, water, and heat, according to the universally known overall reaction [52].

$H_2 + O_2 = HO_2 +$ electricity + heat

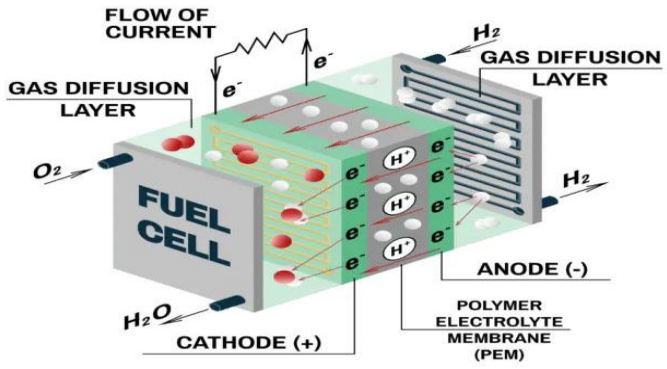

Figure 1.19. Hydrogen fuel cell.

1.9 Power converters

The use of an electric drive system within a vehicle implies the presence on board of a source of electrical energy, which is an accumulator with a capacity adequate for the desired duration of use of the vehicle. In most electric cars, there is a need to address compatibility between direct current (DC) and alternating current (AC) energy sources, as well as between the voltages of the sources and the receivers. Since the electrical energy generated by the sources is in the form of DC voltage, it is essential to have an

interface between the production unit and the application (the load) to adapt the characteristics of the energy sources to those of the load.

To ensure certain functions, such as supplying an adequate voltage level (within suitable limits), protecting the super-capacitor, or managing energy between the battery and other storage elements, a power interface must be implemented. Thus, three main functions of the power interface can be identified:

-Adapt the voltage characteristics to acceptable levels for the intended applications;

-Optimize the system's performance

-Control the state of the energy produced, stored, or supplied.

In most electric vehicles, selecting the type of power interface structure depends on various criteria specific to the application. In these applications, the structure is divided into two parts with different roles, DC (Direct Current) and AC (Alternating Current). DC/DC converters, DC/AC converters, or AC/DC converters must be used [46].

1.9.1 DC-DC converters

Due of its simplicity and the requirement for voltage elevation, the conventional parallel chopper (Boost) stands as the most prevalent topology. It serves as the interface between the electric energy sources and the DC/AC converter on the motor side [53].

1.9.2 DC-AC converters

These converters are commonly used in electric vehicles. There are two basic structures: the voltage inverter and the current switch, with the former being much more widespread. Both can be single-phase or three-phase [53].

1.9.3 AC-DC converters

AC/DC converters, alternatively referred to as rectifiers, are energy conversion devices that change an alternating current electrical source into a direct current electrical source [53].

1.10 Mobility and driving patterns

To evaluate the necessary criteria for the mobility service, a vehicle movement model is required for a fixed profile. During the study, different types of driving cycles were analyzed. The European cycles highlighted in particular are:

ECE-15: (UDC: urbain drive cycle) it was created to simulate urban driving conditions. Figure 1.20 (a).

EUDC: (extra urbain drive cycle): It was added after the fourth ECE cycle for driving modes that require higher power, reaching higher speeds. Figure 1.20 (b).

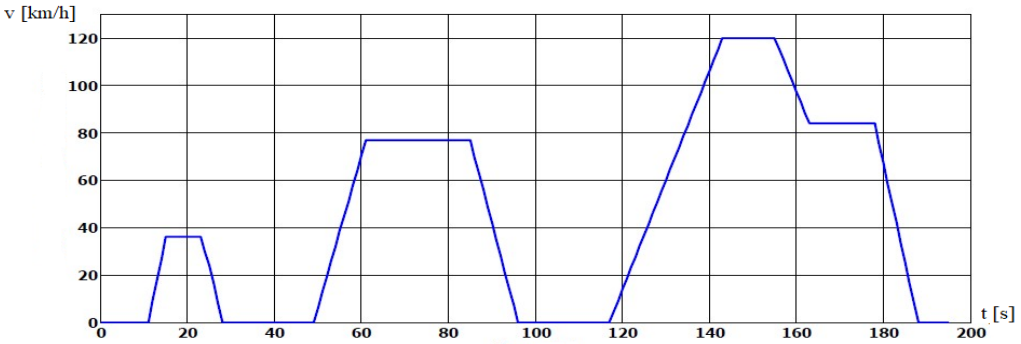

(a)

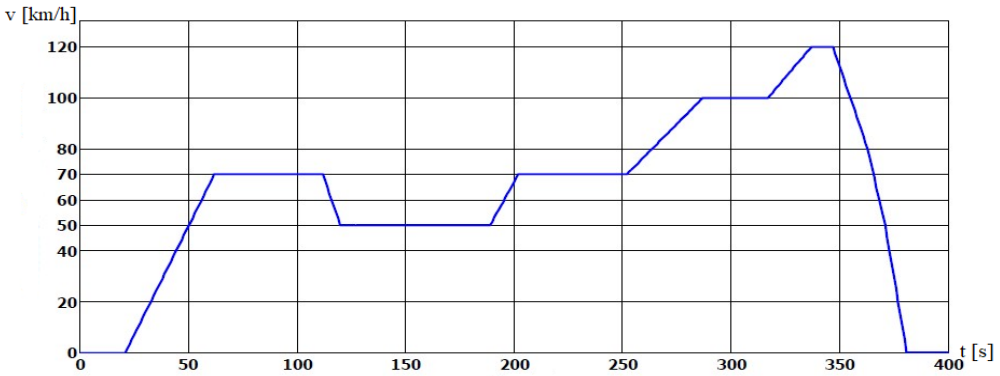

(b)

Figure 1.20. Driving cycles (a) ECE15, (b) EUDC.

NEDC (new european driving cycle): It is a combined cycle of four ECE15 cycles followed by a EUDC cycle. This cycle is the most commonly used by vehicle manufacturers for calculating CO_2 emissions and fuel consumption. This cycle does not require high power and is not accepted in some U.S. states; it will be replaced by the WLTC in the future. Figure 1.21.

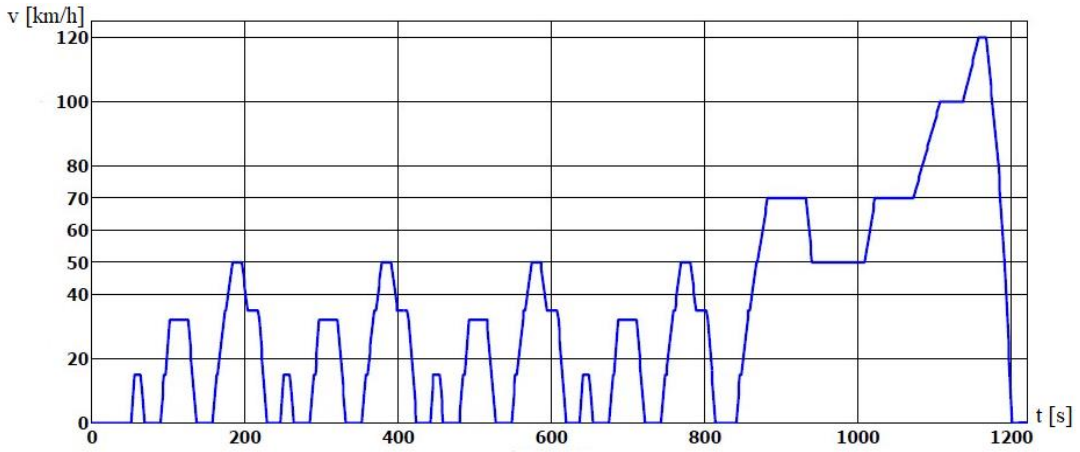

Figure 1.21. Driving cycles NEDC.

1.11 Conclusion

In this chapter, a state-of-the-art review of the electric drive system was presented. Subsequently, we detailed the essential stages of its design, addressing the various onboard energy sources (batteries, fuel cells, super-capacitors) as well as the motor technologies most suitable for this application. The hybrid vehicle would represent an optimal solution if it were not constrained by the excessive weight of the batteries and, above all, by its limited driving range. While awaiting further technological advances that will enable a wider deployment of these alternative solutions (battery electric vehicles, hybrids, and fuel cell vehicles), driven by improvements in battery technology, the mass introduction of hybrid vehicles, and the drastic reduction in the cost and size of fuel cells, the hybrid vehicle market may finally experience the growth that has been anticipated for over a century. On the motor side, given its advantages over other types of rotating electric machines, including robustness, relatively low cost, and reduced maintenance requirements, the Permanent Magnet Synchronous Motor (PMSM) appears to be the most suitable choice for electric vehicle propulsion.

Before achieving optimal control of this propulsion system and defining a control structure that ensures energy optimization, it is customary first to model the various components of the propulsion chain. The following chapter will be dedicated to the modeling of the various subsystems that make up the electric vehicle.

Chapter 2: Modeling of the Traction Chain Elements

2.1 Introduction

To devise a control strategy and accurately estimate the energy consumption of an electric vehicle, having a suitable vehicle model is essential [53]. The complexity of the electric vehicle model arises from the wide range of components it encompasses, including vehicle dynamics, transmission systems, electric machines, power electronics, and energy sources. Each of these components must be precisely modeled to ensure reliable conclusions. The electric vehicle model was created using the MATLAB/Simulink software environment. This chapter presents an analysis of the forces acting on the vehicle. Following the development of the dynamic model, the next step focuses on modeling the system components.

2.2 Description of the electric vehicle traction system

An electric vehicle (EV) powertrain consists of three main subsystems: electric motor propulsion, power supply, and auxiliary systems. The electric propulsion subsystem includes the vehicle controller, electronic power converter, electric motor, mechanical transmission, and drive wheels. The power supply subsystem comprises the power source, power management unit, and power supply unit. Lastly, the auxiliary subsystem primarily consists of the power steering unit, the cabin air conditioning system, and the auxiliary power supply unit.

The illustration in Figure 2.1 shows the components of the electric traction system in an electric vehicle. The system consists of a super-capacitor powered DC voltage source, a fuel cell, IGBT-based power converters, and a control system that manages the electric motors located at the rear of the vehicle, which are connected to the two wheels [54].

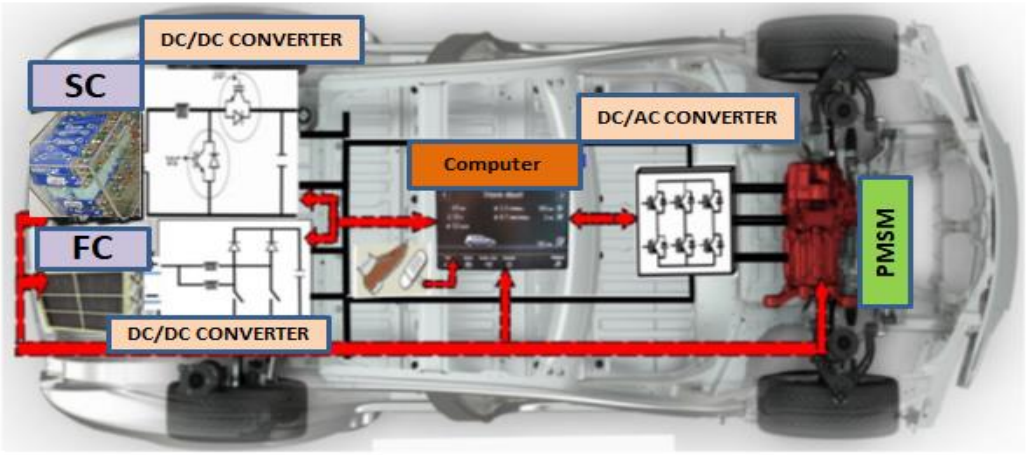

Figure 2.1. General structure of the chosen electric vehicle.

2.3 Vehicle dynamics modeling

The propulsion system produces mechanical energy, which can be stored in the vehicle as kinetic energy during acceleration or as potential energy when the vehicle ascends to higher altitudes. The amount of mechanical energy provided by a vehicle while driving is mainly influenced by three factors:

- losses from aerodynamic drag.
- Losses from rolling resistance.
- Energy dissipated in the brakes.

The mechanical model described in this section calculates the torque and driving force required for the vehicle's operation, as shown in Figure 2.2. The propulsion system must generate a tractive effort at the wheel that equals the combined forces needed to overcome aerodynamic drag, rolling resistance, and road inclination, as well as the force required to accelerate the vehicle. The force needed to pull the vehicle at the wheels is determined by the following equation [55]:

$$F_T = F_{ro} + F_{ad} + F_{cr} + F_{sf} \quad (2.1)$$

Where:

F_{ad} : Aerodynamic resistance.

F_{sf} : Stokes or viscous drag force.

F_{ro} : Rolling resistance force.

F_{cr} : climbing resistance force.

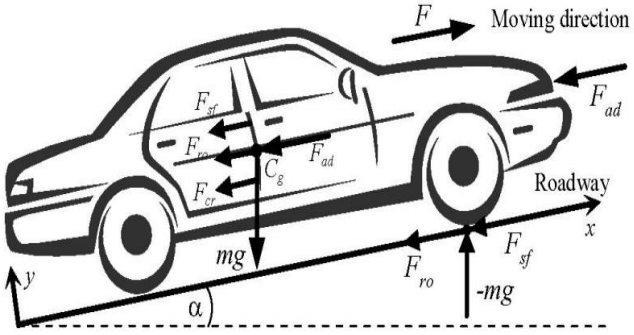

Figure 2.2. Fundamental forces exerted on an electric vehicle.

2.3.1 Force generated by rolling resistance

The resistive force generated by tire road interaction is associated with the mass of the vehicle m, the acceleration due to gravity and the wheel rolling resistance coefficient. In practice, with modern tires designed for minimal rolling resistance, the factor of tire rolling drag C_d is approximately 0.01 (around 0.015 for conventional tires) [56]. This specific factor is influenced by the width of the tires and the type of road surface. Therefore, The force generated by rolling drag is given by [57]:

$$F_{ro} = C_d . m . g . \cos(\alpha) \quad (2.2)$$

2.3.2 Air resistance force

The aerodynamic drag force is linearly related to the air density p, the square of the vehicle's speed V, the wind speed V_w, the frontal surface area of the vehicle A_f, and its coefficient of drag C_f, which ranges from 0.25 to 0.5 depending on the shape of the vehicle's body.

$$F_{ad} = \frac{1}{2} . p . C_f . A_f (V_r)^2 = \frac{1}{2} . p . C_f . A_f (V + V_w)^2 \quad (2.3)$$

2.3.3 Climbing resistance force

The gravitational force exerted by gravity while driving on an inclined road depends on the slope of the road. According to Figure 2.2. This force is positive when the vehicle is ascending and negative when it is descending. It is represented as:

$$F_{cr} = \pm m . g . \sin(\alpha) \quad (2.4)$$

2.3.4 Stokes or viscous drag force

$$F_{sf} = K_a V_r \tag{2.5}$$

K_a : Stokes coefficient.

In the literature, researchers sometimes use the vehicle's acceleration force F_a instead of the viscous friction force F_{sf}, as referenced in [58].

$$F_a = m\lambda \frac{dV_r}{dt} = m + \sum J \left(\frac{i^2}{r^2}\right) \frac{dV_r}{dt} \tag{2.6}$$

Where the mass factor λ which depends on the engaged speed, ranges from 1.06 to 1.34. J is the moment of inertia at the circumference of the driving wheel, i is the gearbox ratio, and r is the wheel radius.

The electric motor generates the traction force needed for an electric vehicle to overcome the roadway load. The equation of motion is therefore defined by:

$$K_m m \frac{dv}{dt} = F_{tr} - F_T \Leftrightarrow m_i \alpha = F_{tr} - F_T \tag{2.7}$$

F_{tr} : Tire traction force.

K_m : Rotational coefficient of inertia (mass factor).

$m_i = K_m m$: Inertia mass of the vehicle.

α : Acceleration of the vehicle.

The net force $(F_{tr} - F_T)$ accelerates the vehicle, or decelerates it if F_T exceeds F_{tr}. The work is defined by the following expression:

$$\vec{\omega} = \sum_{i=1}^{4} \vec{F_i}\, d\vec{x} \tag{2.8}$$

When the work is differentiated with respect to time, the following expression is obtained:

$$p = \frac{d\vec{\omega}}{dt} = \vec{F}\left(\frac{d\vec{x}}{dt}\right) \Leftrightarrow p = \vec{F}.v \tag{2.9}$$

Where

p : is mechanical power.

2.4 Three-phase permanent magnet synchronous machine modeling

Modern control laws, with their increasing efficiency, enhance the management of transient states and ensure precise speed regulation across a broad range of operations

[59]. All these improvements require a good understanding of the machine and its converter, especially in transient states.

2.4.1 Simplifying assumptions

The electrical and dynamic behavior of electric machines can only be studied if it is defined by a mathematical model. To obtain this model, the following simplifying assumptions are taken into account [60]:

-The absence of saturation in the magnetic circuit.

-The sinusoidal distribution of the magnetic flux created by the stator windings.

-Hysteresis, eddy currents, and skin effect are neglected.

-Negligible cogging effect.

-The resistance of the windings does not vary with temperature.

Given that the excitation is supplied by a permanent magnet, the excitation flux is assumed to be constant. Additionally, the magnet is treated as a winding with no inherent resistance or self and mutual inductance, functioning solely as a flux source [61-63].

Under these conditions, the electrical equation for the stator can be formulated using the receiver convention and assuming no damper windings, as follows:

2.4.2 Electrical equations

The three-phase stator voltage equations are expressed as:

$$\begin{bmatrix} v_a \\ v_b \\ v_c \end{bmatrix} = R_s \begin{bmatrix} i_a \\ i_b \\ i_c \end{bmatrix} + \frac{d}{dt} \begin{bmatrix} \varphi_a \\ \varphi_b \\ \varphi_c \end{bmatrix} \tag{2.10}$$

Where:

$[v_a \quad v_b \quad v_c]^t$ are the stator phase voltages, R_s is the stator resistance, $[i_a \quad i_b \quad i_c]^t$ are the stator phase currents and $[\varphi_a \quad \varphi_b \quad \varphi_c]^t$ are the total stator fluxes, which are expressed as:

$$\begin{bmatrix} \varphi_a \\ \varphi_b \\ \varphi_c \end{bmatrix} = L_{ss} \begin{bmatrix} i_a \\ i_b \\ i_c \end{bmatrix} + \begin{bmatrix} \varphi_{af} \\ \varphi_{bf} \\ \varphi_{cf} \end{bmatrix} \tag{2.11}$$

Where:

$$\begin{bmatrix}\varphi_{af}\\ \varphi_{bf}\\ \varphi_{cf}\end{bmatrix} = \varphi_f \begin{bmatrix}\cos\theta\\ \cos(\theta - \frac{2\pi}{3})\\ \cos(\theta + \frac{2\pi}{3}\end{bmatrix} \quad (2.12)$$

Where, φ_f is the amplitude of the flux produced by the permanent magnets.

θ : Absolute rotor position in electrical degrees

$[L_{ss}]$: The matrix of stator inductances.

In a salient pole machine, the matrix of stator self-inductances $[L_{ss}]$ depends on the position. It contains two terms: $[L_{s0}]$ which is constant, and $[L_m(\theta)]$ which is a function of the angle $P\theta_m$, θ is the electrical angle and θ_m is the mechanical position of the rotor relative to the stator. It can be expressed as:

$$[L_{ss}] = [L_{s0}] + [L_m(\theta)] \quad (2.13)$$

With:

$$L_{ss} = \begin{bmatrix}L_{ss} & M_{ss} & M_{ss}\\ M_{ss} & L_{ss} & M_{ss}\\ M_{ss} & M_{ss} & L_{ss}\end{bmatrix} \quad (2.14)$$

The leakage inductance $[L_{s0}]$ and the magnetizing inductance $[L_m]$.

The $[L_m]$ term is expressed within the framework of the first harmonic theory

$$[L_m(\theta)] = L_m \begin{bmatrix}\cos(2\theta) & \cos 2(\theta - \frac{2\pi}{3}) & \cos 2(\theta + \frac{4\pi}{3})\\ \cos 2(\theta - \frac{2\pi}{3}) & \cos 2(\theta + \frac{4\pi}{3}) & \cos(2\theta)\\ \cos 2(\theta + \frac{4\pi}{3}) & \cos(2\theta) & \cos 2(\theta - \frac{2\pi}{3})\end{bmatrix} \quad (2.15)$$

With L_{ss} and M_{ss} representing the self-inductance and the mutual inductance between the stator windings.

The substitution of (2.11) into (2.10) gives:

$$[v_s] = [R_s].[i_s] + \frac{d}{dt}([L_{ss}].[i_s] + [\varphi_f]) \quad (2.16)$$

We notice that equation (2.16) is nonlinear and coupled. To address this issue, we adopt variable changes and transformations that reduce the complexity of the system. In this

case, we apply the Park transformation, which converts the stationary windings (a, b, c) into rotating windings (d, q) that move with the rotor.

2.4.3 Transformation of park

By applying the Park transformation, we transform the real stator quantities (voltage, flux, current) into their fictitious components, known as the d and q components. The Park transformation is defined as follows [64]:

$$[X_{dqh}] = [p(\theta)].[X_{abc}] \quad (2.17)$$

Where X can be a current, a voltage, or a flux and θ represents the rotor position, the terms X_d and X_q represent the longitudinal and transverse components of the stator variables (voltages, currents, fluxes, and inductances).

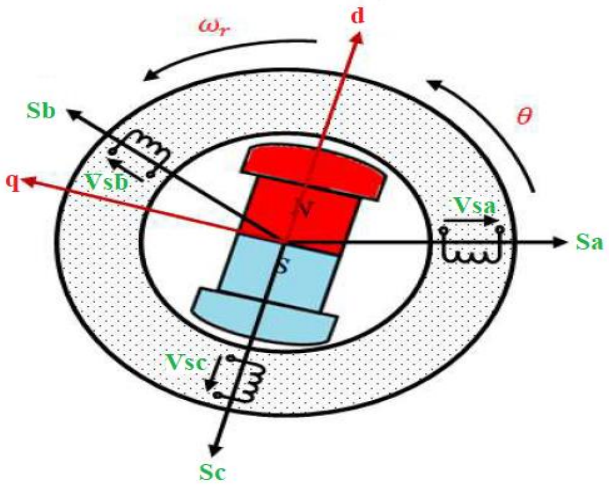

Figure 2.3. Representation of a synchronous machine [60].

In the system of equations (2.18), let us perform the following variable change [65]:

$$[p(\theta)].[v_{dqhs}] = [v_s]$$

$$[p(\theta)].[i_{dqhs}] = [i_s] \quad (2.18)$$

With :

$$[p(\theta)] = \sqrt{\frac{2}{3}} \begin{bmatrix} \frac{1}{\sqrt{2}} & \cos(\theta) & -\sin(\theta) \\ \frac{1}{\sqrt{2}} & \cos(\theta - \frac{2\pi}{3}) & -\sin(\theta - \frac{2\pi}{3}) \\ \frac{1}{\sqrt{2}} & \cos(\theta - \frac{4\pi}{3}) & -\sin(\theta - \frac{4\pi}{3}) \end{bmatrix} \quad (2.19)$$

$[p(\theta)]$ is the Park transformation matrix that converts the stator quantities $[v_s]$, $[i_s]$ and $[\varphi_s]$ into their corresponding components $[v_{dqhs}]$ and $[i_{dqhs}]$.The motor is assumed to be in a star configuration, forming a balanced system $i_a + i_b + i_c = 0$. Thus, the zero-sequence component represented by the first column of matrix (2.18) is zero.

By applying transformation (2.19) to system (2.10), we obtain:

$$[v_{dqs}] = [p(\theta)] . [v_{abcs}] = [p(\theta)] . [R_s] . [i_{abcs}] + [p(\theta)] \frac{d}{dt} ([\varphi_{abcs}]) \quad (2.20)$$

If we premultiply all these terms by $[p\ (\theta)]^{-1}$ and knowing that

$$[R_s] = R_s \begin{bmatrix} 1 & 0 & 0 \\ 0 & 1 & 0 \\ 0 & 0 & 1 \end{bmatrix}$$

Then, based on (2.16), we obtain:

$$[v_{dq}] = [p(\theta)] . [R_s] . [p\ (\theta)]^{-1} . [i_{dq}] + [p(\theta)] .$$

$$[p\ (\theta)]^{-1} . \frac{d}{dt} ([\varphi_{dq}]) + [p(\theta)] . \frac{d}{dt} ([p\ (\theta)]^{-1}) . [\varphi_{dq}] \quad (2.21)$$

with:

$$[p\ (\theta)]^{-1} = \sqrt{\frac{2}{3}} \begin{bmatrix} \frac{1}{\sqrt{2}} & \frac{1}{\sqrt{2}} & \frac{1}{\sqrt{2}} \\ \cos(\theta) & \cos(\theta - \frac{2\pi}{3}) & \cos(\theta - \frac{4\pi}{3}) \\ -\sin(\theta) & -\sin(\theta - \frac{2\pi}{3}) & -\sin(\theta - \frac{4\pi}{3}) \end{bmatrix} \quad (2.22)$$

2.4.3.1 Model of the permanent magnet synchronous machine in the park reference frame

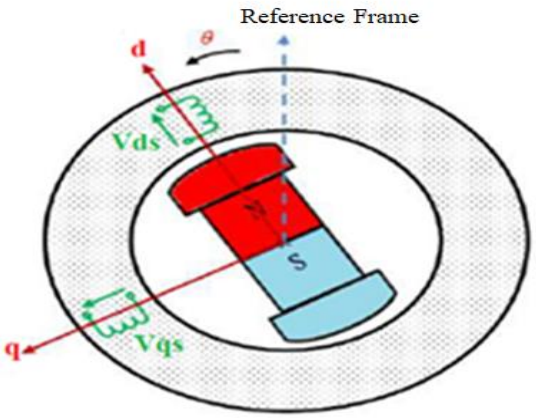

Figure 2.4. Equivalent machine of park transformation [65].

By utilizing (2.21), we derive the stator equations of the machine expressed in the rotor-linked Park reference frame:

$$\begin{cases} v_d = R_s . i_d + \frac{d\varphi_{fd}}{dt} - \omega_r \varphi_{fq} \\ v_q = R_s . i_q + \frac{d\varphi_{fq}}{dt} + \omega_r \varphi_{fd} \end{cases} \quad (2.23)$$

According to equations (2.13), (2.17) and (2.22), we have:

$$[\varphi_{dq}] = [p(\theta)] . [\varphi_{abc}] + \varphi_f$$

$$[\varphi_{dq}] = [p(\theta)] . [L] . [p(\theta)]^{-1} . [i_{dq}] + \varphi_f \quad (2.24)$$

Therefore:

$$\varphi_d = L_d . i_d + \varphi_f$$

$$\varphi_q = L_q . i_q \quad (2.25)$$

L_d, L_q : Direct and quadrature axis inductances.

Considering the flux equations, we can express:

$$\begin{cases} v_d = R_s . i_d + L_d \frac{di_d}{dt} - L_q \omega_r i_q \\ v_q = R_s . i_q + L_q \frac{di_q}{dt} + \omega_r (L_d i_d + \varphi_f) \end{cases} \quad (2.26)$$

These equations allow us to draw the equivalent circuit of the Permanent Magnet Synchronous Machine (PMSM) in the d-q axis system shown below [64-66]:

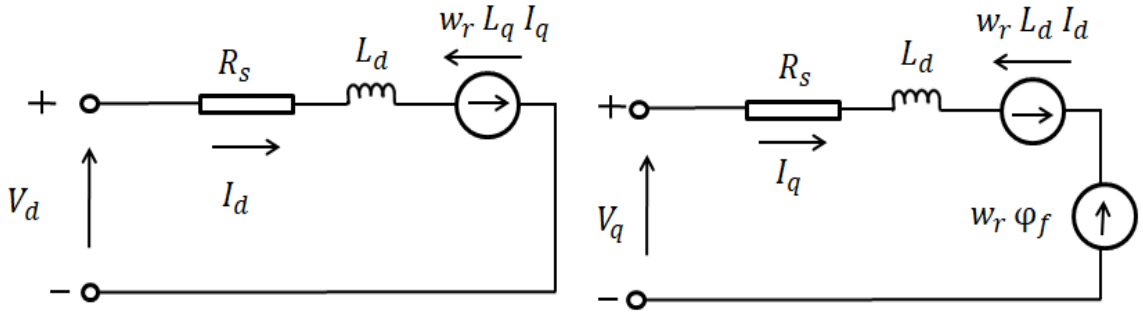

Figure 2.5. The equivalent circuit of the PMSM in the d-q axis system.

2.4.4 Expression of the power and electromagnetic torque

As Park states, the expression for power is given as follows:

$$P(t) = v_d i_d + v_q i_q \tag{2.27}$$

By replacing v_d and v_q with their expressions, we get:

$$p(t) = \frac{2}{3}\left[R_s\left({i_d}^2 + {i_q}^2 \right) - \left(i_d \frac{d}{dt}\varphi_d + i_q \frac{d}{dt}\varphi_q\right) + \frac{d}{dt}\left(\varphi_d i_q - \varphi_q i_d\right) \right] \tag{2.28}$$

Therefore:

The first term represents the Ohmic voltage drop (Joule losses).

The second term represents the change in stored magnetic energy.

The third term represents the power transferred from the stator to the rotor through the air gap (electromagnetic power).

Considering that :

$$P_e = C_e . \Omega \tag{2.29}$$

Therefore:

$$C_e = \frac{3}{2} P(\varphi_d i_q - \varphi_q i_d) \tag{2.30}$$

By replacing φ_d and φ_d with their expressions, we get:

$$C_e = \frac{3}{2} P[(L_d - L_q) i_d i_q + \varphi_f i_q] \quad (2.31)$$

With:

P : Number of pole pairs.

2.4.4.1 Mechanical équation

Analyzing transient regimes requires considering both electrical and mechanical quantities. Therefore, to complete the model, we must incorporate the mechanical equation derived from the moment theorem Figure 2.6.

The crucial equation that finalizes the PMSM model is the fundamental mechanical equation that describes the rotor dynamics of the machine:

$$\sum_i C_i = j\frac{d\Omega}{dt} \quad (2.32)$$

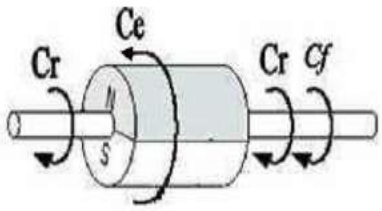

Figure 2.6. The different torques acting on the rotor.

The mechanical equation for the machine is expressed as:

$$j\frac{d\Omega}{dt} = (C_e - C_r - f\Omega)$$

$$C_f = f\Omega \quad (2.33)$$

$\omega_r = P\Omega$: mechanical rotational speed of the machine.

C_r: Resistant couple.

C_e : Electromagnetic couple.

j : Moment of inertia.

P : Number of pole pairs.

Ω : Electrical speed of the rotor.

f : Friction coefficient.

By determining the final form of the PMSM equations in the d-q reference frame with i_d , i_q ω_r and C_e as state variables:

$$\frac{di_d}{dt} = -\frac{R}{L_d} i_d + \frac{L_q}{L_d} P\omega_r i_q + \frac{1}{L_d} v_d$$

$$\frac{di_q}{dt} = -\frac{R}{L_q} i_q + \frac{L_d}{L_q} P\omega_r i_d - \frac{\varphi_f}{L_q} P\omega_r + \frac{1}{L_d} v_q \quad (2.34)$$

$$\frac{d\omega_r}{dt} = \frac{3P}{2j} \left(\varphi_f i_q + (L_d - L_q) i_d i_q\right) - \frac{1}{j} C_r - \frac{f}{j} \omega_r$$

$$C_e = \frac{3}{2} P \left[(L_d - L_q) i_d i_q + \varphi_f i_q\right.$$

2.4.4.2 State equation formulation

Assume the voltages (v_d, v_q) and the excitation flux φ_f are control variables, while the stator currents (i_d , i_q) are state variables. Using equations (2.34), the system of equations can be expressed as follows [62], [63]:

$$\frac{d[X]}{dt} = [A][X] + [B][U] \quad (2.35)$$

$$\frac{d}{dt}\begin{bmatrix} i_d \\ i_q \end{bmatrix} = \begin{bmatrix} -\frac{R_s}{L_d} & P\omega_r \frac{L_q}{L_d} \\ -P\omega_r \frac{L_d}{L_q} & -\frac{R_s}{L_q} \end{bmatrix} \begin{bmatrix} i_d \\ i_q \end{bmatrix} + \begin{bmatrix} \frac{1}{L_d} & 0 & 0 \\ 0 & \frac{1}{L_q} & 0 \\ 0 & 0 & -\frac{\omega_r}{L_q} \end{bmatrix} \begin{bmatrix} v_d \\ v_q \\ \varphi_f \end{bmatrix} \quad (2.36)$$

With:

$\frac{d[X]}{dt}$: System dynamics vector.

$[A]$: State matrix.

$[X]$: State vector.

$[B]$: Input matrix.

$[U]$: Control vector.

2.5 PEM fuel cell modeling

The energy sources for our electric vehicle, including the fuel cell (FC) and super capacitors (SC), have already been presented. This section focuses on the modeling of these two sources. This modeling is crucial and beneficial for maximizing the performance of these sources in electric vehicle applications.

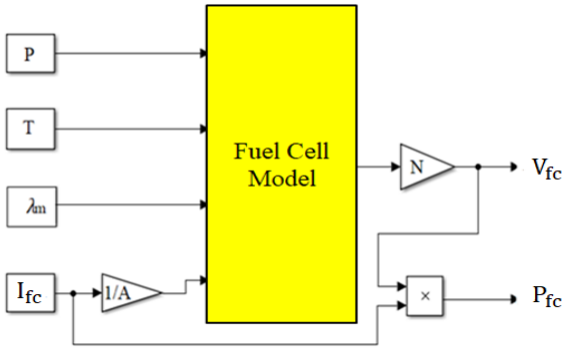

Figure 2.7. Schematic block diagram of the simulation model of the stack voltage.

2.5.1 Static characteristics of a fuel cell (PEM)

Several studies, including those in [67], suggest a static model that represents the polarization curve of the PEM fuel cell Figure 2.8 as the sum of four components: The Nerst tension E_{nerts}, the activation over-voltage v_{act}, the ohmic over-voltage v_{ohm}, and the concentration over-voltage v_{conc}.

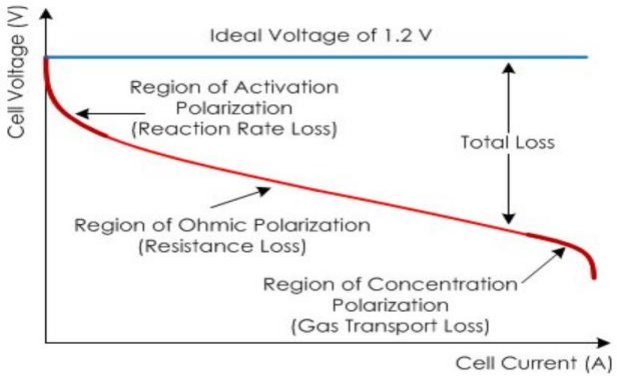

Figure 2.8. Static characteristics of a fuel cell (PEM) [67].

$$V_{fc} = E_{nerst} - V_{act} - V_{ohm} - V_{conc} \quad (2.37)$$

2.5.1.1 The open-circuit voltage of the fuel cell, Nernst equation

The fuel cell converts chemical energy directly into electrical energy. The chemical energy released by the fuel cell is determined by the change in Gibbs free energy (Δg_f), which is the difference between the Gibbs free energy of the products and the Gibbs free energy of the reactants. Gibbs free energy is used to determine the available energy necessary for external work.

The equation for calculating the change in Gibbs free energy is given [68] as follows:

$$\Delta g_{\mathrm{f}} = g_{\mathrm{f}}\,\mathrm{products} - g_{\mathrm{f}}\,\mathrm{reagents} = (g_{\mathrm{f}})_{\mathrm{H_2O}} - (g_{\mathrm{f}})_{\mathrm{H_2}} - (g_{\mathrm{f}})_{\mathrm{O_2}} \quad (2.38)$$

The variation in Gibbs free energy is influenced by temperature and pressure:

$$\Delta g_{\mathrm{f}} = \Delta g^{0}{}_{\mathrm{f}} - \overline{\mathrm{R}}\mathrm{T_{fc}}\ln\left[\frac{\mathrm{P_{H_2}}\mathrm{P}^{\frac{1}{2}}{}_{\mathrm{O_2}}}{\mathrm{P_{H_2O}}}\right] \quad (2.39)$$

Where:

$\Delta g^{0}{}_{\mathrm{f}}$: variation of Gibbs free energy at standard pressure (1 bar), which depends on the temperature $\mathrm{T_{fc}}$ expressed in Kelvin.

$\mathrm{P_{H_2}}$, $\mathrm{P_{O_2}}$ et $\mathrm{P_{H_2O}}$: hydrogen, oxygen, and water vapor pressures.

$\overline{\mathrm{R}}$: Universal gas constant (8:3145J= (kg:K)).

For each mole of hydrogen, two electrons pass through the external electric circuit, and the electrical work done is calculated as follows:

$$\mathrm{L(electrical\ work\ performed)} = -2\mathrm{FE} \quad \mathrm{(joules)} \quad (2.40)$$

Where:

F: is the Faraday constant (F = 96485 coulombs), which is the electric charge of one mole of electrons.

E**:** Open-circuit voltage of the fuel cell.

if the system is lossless:

$$\Delta g_{\mathrm{f}} = -2\mathrm{FE} \quad (2.41)$$

$$\mathrm{E} = \frac{-\Delta g_{\mathrm{f}}}{2\mathrm{F}} = \frac{-\Delta g^{0}{}_{\mathrm{f}}}{2\mathrm{F}} + \frac{\overline{\mathrm{R}}\,\mathrm{T_{fc}}}{2\mathrm{F}}\ln\left[\frac{\mathrm{P_{H_2}}\mathrm{P}^{\frac{1}{2}}{}_{\mathrm{O_2}}}{\mathrm{P_{H_2O}}}\right] \quad (2.42)$$

The term $\frac{-\Delta g_{\mathrm{f}}}{2\mathrm{F}}$ varies depending on the operating point; in practice, it is equal to 1.229 V under standard conditions (25°C and 1 bar).

2.5.1.2 The activation over-voltage

The activation over-voltage are primarily due to the kinetics of the chemical reactions, with the hydrogen reaction being fast, while the oxygen reaction is slower [68].

$$V_{act} = \alpha \ln\left(\frac{i}{i_0}\right) \quad (2.43)$$

where:

α : the constant to be determined empirically.

i : Current density delivered by the fuel cell.

i_0 : Exchange current density equivalent to the electron flux at the electrolyte/electrode interface under open-circuit conditions.

Another similar function, valid for the entire range of i, is used in fuel cell models:

$$V_{act} = V_0 + V_a(1 - e^{-c1i}) \quad (2.44)$$

V_0 : The voltage drop at a current density equal to 0, V_a (volts) and c_1 are constants.

2.5.1.3 The ohmic over-voltage

The ohmic over-voltage are due on one hand to the contact resistance of the different layers of the cell and on the other hand to the resistance encountered by the charged particles. H^+ ions in the electrolyte and e^- electrons in the electrodes, the bipolar plates and the connections (The contact resistance is negligible compared to the ionic resistance of the electrolyte and the resistances of the anode and the cathode) [68].

$$V_{ohm} = i.R_{ohm} \quad (2.45)$$

$$R_{ohm} = \frac{t_m}{\sigma_m} \quad (2.46)$$

Where:

t_m and σ_m are respectively the thickness and the conductivity of the membrane.

The variation in membrane conductivity with different values of humidity and temperature is given as follows:

$$\sigma_m = b_1 \exp\left(b_2\left(\frac{1}{303} - \frac{1}{T_{fc}}\right)\right) \quad (2.47)$$

Where:

b_1 is a function of the membrane water content, λ_m. b_2 is a constant.

$$b_1 = (b_{11}\lambda_m - b_{12}) \tag{2.48}$$

The constants b_{11}, b_{12}, and b_2 are usually determined empirically.

2.5.1.4 The concentration over-voltage

At high current densities, the low transport rate of reactants or products to the reaction site is the main cause of concentration drop. This voltage drop is expressed in terms of a limiting current density called i_L, which is inversely proportional to temperature, and a constant B, known as the transport or mass transfer constant [68].

$$V_{conc} = -B \ln\left[1 - \frac{i}{i_L}\right] \tag{2.49}$$

Another, simpler empirical relationship:

$$V_{conc} = i(c_2 \frac{i}{i_{max}})^{c3} \tag{2.50}$$

c_2, c_3 et i : Constants that depend on temperature and pressure

i_{max}: Maximum current density.

2.5.1.5 Output voltage of a fuel cell system

By combining all the voltage drops related to the losses in the previous sections, the operating voltage of the fuel cell can be expressed as follows [68]:

$$V_{fc} = E_{nerst} - V_{act} - V_{ohm} - V_{conc} \tag{2.51}$$

$$= E_{nerst} - \left[V_0 + V_a\left(1 - e^{-c1i}\right)\right] - \left[iR_{ohm}\right] - \left[i\left(c_2 \frac{i}{i_{max}}\right)^{c_3}\right]$$

Where:

V_{fc} : fuel cell voltage (V),

E_{nerst} : open-circuit voltage of the cell (Nernst potential),

V_{ohm}, V_{conc}, and V_{act} are the ohmic, concentration, and activation over voltages, respectively, the voltage V_{fc} is the voltage of a single fuel cell.

Multiple cells are stacked in series to form a stack. To calculate the voltage of the stack, you need to multiply the voltage of a single cell by the number of cells, n, and the stack current, I_{st}, is equal to the current of the cell.

The current density is then defined as the stack current per unit of the active cell area:

$$\begin{cases} V_{st} = N.V_{fc} \\ i = \frac{I_{st}}{A} \end{cases} \quad (2.52)$$

2.6 Modeling of super capacitors

A super capacitor can be quite simply modeled using the following model. We have chosen that the super capacitors, added as high-power storage devices, must supply the entire power $P_{load} = P_N$ for Δt = 10s. The energy supplied is estimated to be approximately 4.8MJ [27].

The energy E_{sc} stored at the voltage U_{sc} of the SC pack can be expressed as follows:

$$E_{sc} = \frac{1}{2} C_{eq} U^2{}_{sc} = \frac{1}{2} \frac{N_{psc}}{N_{ssc}} C_{sc} U^2{}_{sc} \quad (2.53)$$

Where C_{eq} is the equivalent capacitance of the SC pack, N_{psc} and N_{ssc} are the number of parallel branches and the number of series connections of SC_s, respectively, and C_{sc} is the SC capacitance.

The super-capacitors considered in this thesis are of the Maxwell/BCAP3000 type, rated at 3000F, 2.7 V, with parameters given in Table D.1 (Appendix D)

It is generally allowed to use 75% of the energy stored in the SC pack by discharging the pack from its nominal voltage $U_m = 300V$ (approximately 80% of the DC bus voltage [28]) to half of this value, equal to $U_m = 150V$

It is generally allowed to use 75% of the energy stored in the SC pack by discharging the pack from its nominal voltage.

Each elementary SC is then discharged from an initial voltage $V_{sci} = 2.7V$ to a final voltage $V_{scf} = 1.35V$, Additionally, internal losses in the SC_s can be accounted for by the efficiency coefficient k=0.9 [28].

The energy extracted from the SC_s can then be expressed as:

$$P_N \Delta t = k\left(\frac{1}{2} C_{eq} U^2{}_M - \frac{1}{2} C_{eq} U^2{}_m\right) \quad (2.54)$$

To optimize the combination of super capacitors with the battery in UPS applications, we need to establish a model to describe the behavior of the super capacitor during rapid charge and discharge cycles. We consider the equivalent electrical circuit with two RC branches, as proposed by [30], as shown in Figure 2.9.

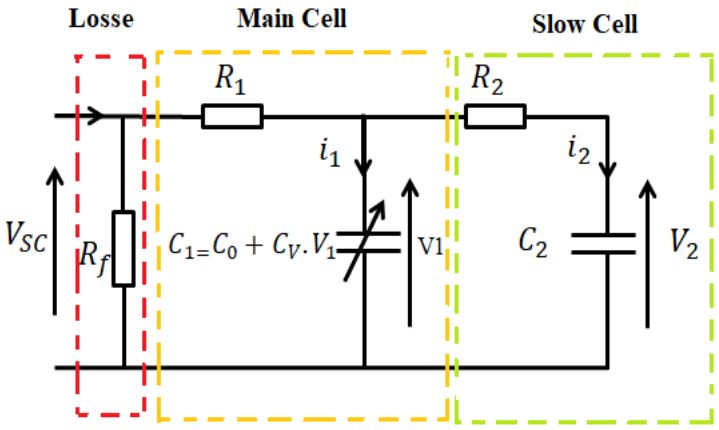

Figure 2.9. Simplified circuit of the super-capacitor: two-branch model [69].

The main capacitance C_1 (differential capacitance [71]) depends on the voltage v_1. It consists of a constant capacitance C_0 (in F) and a constant parameter C_v (in F/V), and it is expressed as $C_1 = C_0 + C_v v_1$. The R_1C_1 branch determines the immediate behavior of the super capacitor during rapid charge and discharge cycles over a few seconds.

The R_2C_2 cell is the slow branch. It complements the first cell over a long time range of a few minutes and describes the internal energy distribution at the end of charging (or discharging).

The equivalent parallel resistance R_f represents the leakage current and can be neglected during the rapid charge/discharge of the super capacitor.

2.7 Gearbox

At the output of the electric motor shaft, torque is available. This torque is transmitted to the wheels through several mechanical components. The first is the gearbox. The Hy Power Bora features a continuously variable transmission (CVT), where the transmission ratio is controlled by a hydraulic system that changes the pulley diameters. However, due to the complexity of the system, the modeled system is that of a speed reducer with a fixed transmission ratio Figure 2.10.

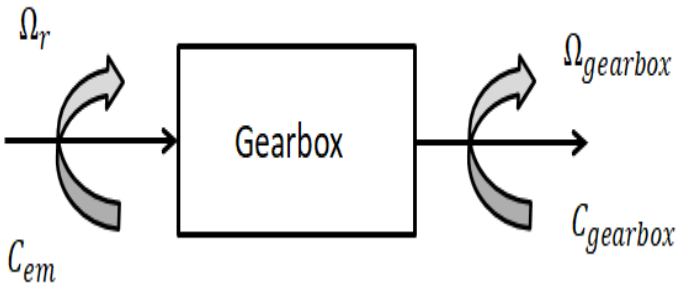

Figure 2.10.Gearbox.

From the expression below, the resisting torque applied to the machine is deduced in the case of a lossless reducer:

$$\Omega_r = n.\Omega_{gearbox} \tag{2.55}$$

$$C_{em} = \frac{C_{gearbox}}{n} \tag{2.56}$$

$$\Omega_r.C_{em} = \Omega_{gearbox}..C_{gearbox} \tag{2.57}$$

with n: reduction ratio

The angular velocity Ω_r (rad/s) is related to the vehicle speed $\frac{V_h}{R}$ (m/s) by the following relation:

$$\Omega_r = \frac{V_h}{R} \tag{2.58}$$

- **Speed Profile Over Time**

Figure 2.11 shows the speed profile of the NEDC cycle used to perform the analysis.

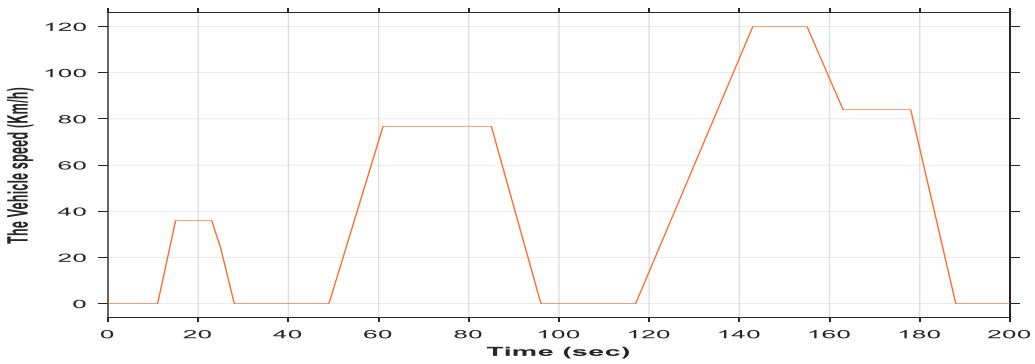

Figure 2.11. The vehicle speed over time.

Three distinct phases can be identified in this speed profile:

- The phase where the speed increases linearly, the acceleration phase
- The phase where the speed is constant, the steady phase;
- The phase where the speed decreases linearly, the deceleration phase.

In conclusion, the speed behavior over time always follows the following form (an affine function):

$$v(t) = at + b \tag{2.59}$$

Depending on the considered speed phase, a and the average speed during this phase are calculated, and ultimately, the force that the vehicle must develop during this phase is determined. Figure 2.12 shows the evolution of the traction force over time for a 10% incline between 16s and 22s, based on the NEDC speed cycle.

- **Calculation of the traction force over time:**

According to the fundamental equation of dynamics:

$$\vec{m}\alpha = \vec{F}_{tr} + \vec{F}_{ad} + \vec{F}_{cr} + \vec{F}_{ro} \tag{2.60}$$

By projecting these forces along the direction of motion:

$$m\alpha(t) = F_{tr}(t) - F_{ad}(t) - F_{cr}(t) - F_{ro}(t) \tag{2.61}$$

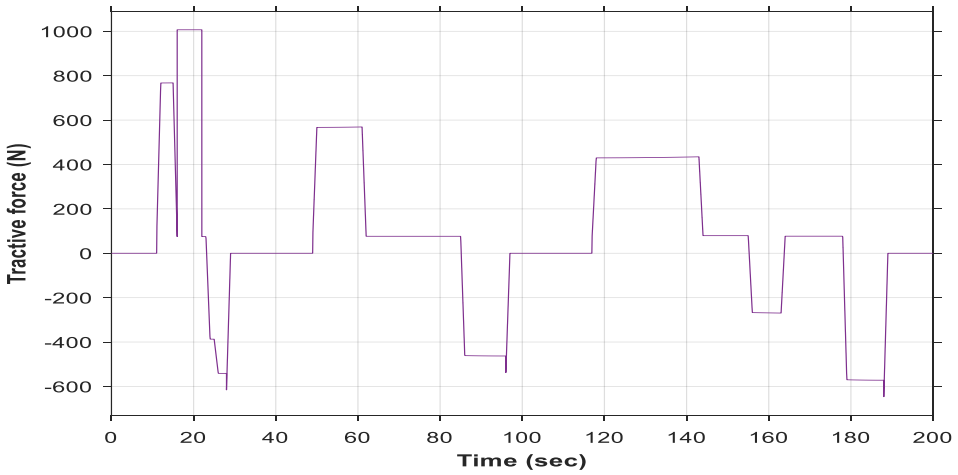

Figure 2.12. Evolution of the traction force over time for a 10% incline.

The figure illustrates the time evolution of the vehicle's traction force according to the NEDC cycle. An alternation between positive and negative values can be observed,

corresponding respectively to the acceleration and braking (or energy recovery) phases. A significant increase in traction force is noted between 16 s and 22 s, reaching approximately 1000 N, due to the presence of a 10% slope that requires greater motor effort. These variations reflect the vehicle's dynamic behavior and the response of the propulsion system to the different demands of the driving cycle.

- **Power Calculation:**

By definition, power is:

$$P(t) = F(t).V(t) \tag{2.62}$$

For the following, we do not consider power losses (in other words, we do not take efficiency into account). Depending on the speed phase and the force developed during this phase, the vehicle's power is determined. Figure 2.13 illustrates the evolution of power over time for a 10% incline between 16s and 22s.

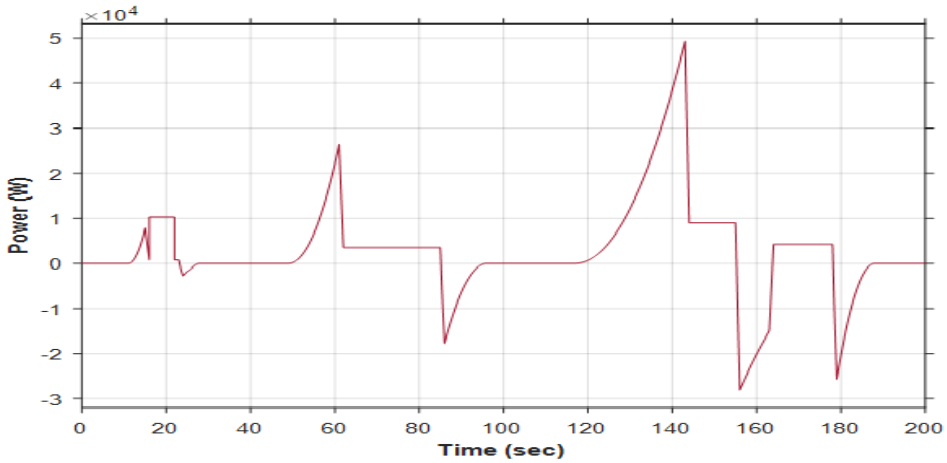

Figure 2.13. Évolution de la puissance en fonction du temps pour une pente de 10%.

Variation of the vehicle's power over time. The plot shows alternating motoring phases (positive power) and regenerative braking phases (negative power). A noticeable rise in power between 16 s and 22 s corresponds to a 10% uphill segment. The peak power reaches approximately 4.8×10^4 while the minimum value is about 2.9×10^4 demonstrating the system's ability to both supply and recover substantial power under varying driving conditions.

- **Maximum current**

The current is calculated by:

$$I(t) = \frac{P(t)}{U_{DC\_Bus}} \tag{2.63}$$

Figure 2.14 shows the current curve as a function of time for a 10% incline.

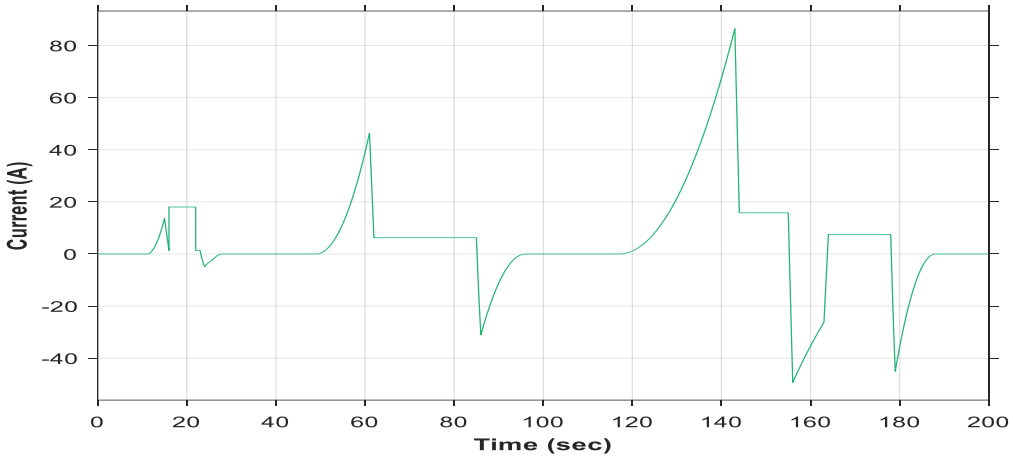

Figure 2.14. Current as a function of time.

The peak current reaches about 83 A, whereas the minimum value is around −55 A, demonstrating the system's capability to both deliver and recuperate substantial electrical current under varying driving conditions.

So in our work, we have chosen the traction motor power to be 50 kW. The machine parameters must be specified in the electric drive model of the PMSM under Matlab/Simulink, as shown in Table A.1 (Appendix A).

2.8 Overview of the fuel cell vehicle considered

At present, numerous automotive applications rely on fuel cells as the primary energy source and super capacitors as supplementary power sources. The use of super capacitors helps to reduce the power strain on the main energy source, namely the fuel cell. Throughout this work, the characteristics of the studied vehicle are assumed to be similar to those of the Volkswagen Bora HY Power, such as a maximum speed of 140 km/h and an acceleration from 0 to 120 km/h in 10 seconds [72]. The Volkswagen Bora HY Power vehicle consists in part of:

-A fuel cell consists of four blocks mounted in parallel. Each block includes three stacks connected in series. A stack has a power output of approximately 8 kW and is composed of 25 cells. During operation, a portion of the fuel cell's power is consumed by its accessories (air compressor, motorized valves, etc.). The hydrogen supply is provided by 26 compressed hydrogen tanks at 350 bars.

-A super-capacitor module consists of two blocks mounted in parallel. Each block contains 84 super-capacitor cells connected in series. A cell has a capacitance of 3000 F and a nominal voltage of approximately 2.5V. It has a maximum specific energy of 5.3 Wh/kg and a maximum specific power of 4.8 kW/kg.

-Intermediate converters: a Boost converter connected to the fuel cell, a Buck/Boost converter connected to the super-capacitors, and an inverter connected to the DC bus, where the voltage must be regulated at 570 V; the switches used are 600 V IGBTs with anti-parallel diodes.

-A synchronous motor with a nominal power of approximately 50 kW, peak power, and a maximum torque of 255 Nm.

2.9 Sizing of the vehicle's energy sources

The objective of this section is to present a method for sizing the energy sources (fuel cell and super-capacitor module) in a fuel cell vehicle, specifically to determine the required number of fuel cell units and super-capacitor module. The specifications considered are those of the Bora vehicle. We only consider the characteristics of the energy sources (fuel cell and super-capacitors) used in the Bora vehicle [72] and [73]. The electrical system of the vehicle under study contains:

-Two DC-DC converters are used to adjust the voltage levels between the two sources and the DC bus. The converter associated with the fuel cell operates in Boost mode, raising the fuel cell voltage to 570V. It is unidirectional. The other converter, placed between the super capacitors and the DC bus, is bidirectional. It operates in Boost mode when the super capacitors supply electrical energy to the DC bus and in Buck mode when electrical energy is directed to the super capacitors to charge them.

-An inverter connected to the DC bus

-A synchronous machine that drives the vehicle's wheels

The mass of the vehicle under study is assumed to be around one ton (the mass of the Bora vehicle body is 1000 kg). It has a frontal area of approximately 2.5 m², a drag

coefficient of about 0.3, and a rolling resistance coefficient of around 0.01. The maximum speed is 120 km/h, with an acceleration from 0 to 100 km/h in 12.5 seconds.
To size the vehicle's energy sources, it is important to estimate the power required by the vehicle. Assuming that the road is flat, it is expressed by [73]:

$$P_{ch} = \left[\frac{1}{2}P_{air}V_h{}^2SC_x + MgC_r + Mg\sin\alpha + M\frac{dV_h}{dt}\right]V_h \quad (2.64)$$

with:

M : The mass of the vehicle (in kg)

V_h: The speed of the vehicle (in m/s)

SC_x: The master torque coefficient (frontal area × drag coefficient) (in m²)

P_{air} : The air density (kg/m³)

C_r : The vehicle's rolling resistance coefficient

g: The acceleration due to gravity (9.81 m/s²).

2.9.1 Fuel cell sizing

The fuel cell is the primary energy source in the vehicle. Therefore, it must be able to provide sufficient power for the vehicle to reach a maximum speed of 120 km/h as specified in the requirements. Using equation (2.64) and assuming the vehicle's speed is stabilized at 120 km/h, the power of the fuel cell is calculated to be 47.2 KW. Adding 5% for the power consumed by the fuel cell auxiliaries, we obtain a maximum power of approximately $P_{fc_{max}} = 49.56\ KW$

The voltage limit E_{cell} of a single cell in a PEM fuel cell is 8 V. This voltage corresponds to the maximum power provided by the cell. The fuel cell must power a DC bus $U_{DC} = 570$ via a multi-level Boost converter. The Boost converter's efficiency decreases as the transformation ratio increases [74], so the duty cycle should be around 0.29 for optimal operation [74]. Therefore, the fuel cell voltage $U_{fc} = N_{fc_{series}}.E_{cell}$ must be at least equal to $U_{DC}(1 - D)/2$ where $N_{fc_{series}}$ is the number of cells connected in series. It is given by:

$$N_{fc_{series}} = \frac{U_{fc}}{E} = 25 \quad (2.65)$$

The fuel cell used in the Bora vehicle has a power of $N_{fc_{cell}} = 500W$. The number of series branches connected in parallel is given by:

$$N_{fc_{parallele}} = \frac{N_{fc_{max}}}{N_{fc_{series}}\ N_{fc_{cell}}} \approx 4 \quad (2.66)$$

In summary, the fuel cell onboard the vehicle consists of four blocks connected in parallel, with each block containing three stacks connected in series. Each stack is an assembly of 25 cells.

2.9.2 Sizing of Super capacitors

Super capacitors serve as an auxiliary energy source, operating during acceleration and braking of the vehicle. The maximum power that the super capacitors must supply to the vehicle for it to accelerate from 0 to $V_{tf} = 100$km/h in t_a= 36.5 s is given by [74]:

$$P_{SCmax} = M\frac{V_{tf}}{t_a}V_{tf} \quad (2.67)$$

We have determined a maximum power of P_{SCmax}. This power corresponds well to that of the super capacitor module used in the Bora vehicle. According to the specifications of the HY. Power Bora vehicle, a super capacitor module is sized based on the required power and the duration for which it must supply this power.

The sizing methodology consists of determining:

-The operating voltage range.

-The maximum transferred energy $E_{max_{transf}}$

-The number of elements to be connected in series Ns and in parallel Np

The following parameters are defined:

$N_{élé}$: The total number of super capacitors

$V_{élé_{max}}$: The maximum allowable voltage of a super capacitor

$U_{sc_{max}}$: The maximum voltage of the super capacitor module

$U_{sc_{min}}$: The minimum voltage of the super capacitor module

Generally, $U_{sc_{min}} = \frac{U_{SC_{max}}}{2}$ because when the super capacitor module discharges between $U_{SC_{max}}$ and $\frac{U_{SC_{max}}}{2.75\%}$ of the stored electrical energy is consumed.

The maximum transferred energy (corresponding to 20 kW for 36.5 s) is given by:

$$E_{max_{transf}} = P_{SC_{max}}t_a = \frac{1}{2}N_{élé}C_{élé}(V^2{}_{élé_{max}} - \frac{V^2{}_{élé_{max}}}{4}) \quad (2.68)$$

Using equation (2.68), the number of elementary super capacitors required to meet the energy demand is expressed as:

$$N_{élé} = N_p N_s = \frac{E_{max_{transf}}}{C_{élé} V^2_{élé_{max}}} \frac{2}{1-k^2} = \frac{E_{max_{transf}}}{C_{élé} V^2_{élé_{max}}} \frac{2}{1-(0.55)^2} \quad (2.69)$$

Sizing assumption: To ensure a safety margin relative to the minimum voltage of the super capacitor pack, the calculation of the number of elements is performed with a discharge depth of k=55% with:

k : Depth of discharge

$C_{élé}$: Capacitance of a super capacitor element (F). For a super capacitor cell used in the vehicle, we have $N_{élé} = 300F$ with $V_{élé_{max}}$(the maximum voltage is set to this value to ensure better longevity). Hence:

$E_{max_{transf}} = 730$ KJ and $N_{élé} = 95$

The maximum voltage of the super capacitor module is set to $U_{SC_{max}} = 240V$ to ensure acceptable converter efficiency, hence:

$$N_s = \frac{U_{SC_{max}}}{V_{élé_{max}}} \approx 84 < N_p = \frac{N_{élé}}{N_s} = 1.31, \text{ Thus } N_p \approx 2 \quad (2.70)$$

To summarize, the super capacitor module installed in the vehicle consists of two blocks connected in parallel. Each block contains 84 super capacitor cells connected in series. Each cell has a capacitance of 3000 F.

2.10 Power supply system

The use of an electric powertrain in electric vehicles implies the presence on board of an electric energy source, which can be:

-A fuel cell with a capacity appropriate for the vehicle's desired range.

-The super-capacitor stacks onboard.

In the majority of electric vehicles, there is a challenge regarding the compatibility between the voltages of the sources and the receivers. This compatibility challenge requires the presence of electronic converters onboard electric vehicles, which are responsible for eliminating operational incompatibilities.

Therefore, vehicles may be equipped with:

- DC-DC converters
- AC-DC converters

- DC-AC converters

This section explains the role of (DC-AC) converters onboard an electric vehicle in powering an PMSM [66].

Figure 2.15 depicts the schematic diagram of the converter-machine connection

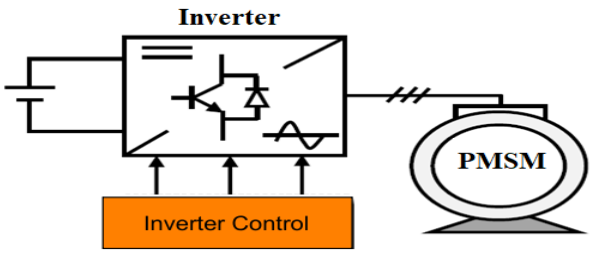

Figure 2.15. Global diagram of a variable-speed PMSM and its power supply.

There are several types of inverters:

- Voltage inverters.
- Current inverters.
- According to the number of phases (single-phase, three-phase).
- According to the number of levels (2, 3, etc.).

2.10.1 Modeling of the two-level three-phase voltage inverter

The inverter is a static converter that transforms a direct current signal into an alternating current signal with adjustable frequency and amplitude [62]. It plays a crucial role in machine control, especially for synchronous machines.

The inverter circuit consists of six bidirectional switches, each composed of a transistor and a flyback diode connected in anti-parallel, as shown in Figure 2.16. The pairs of switches (k11, k12), (k21, k22), and (k31, k32) are controlled in a complementary manner to ensure the continuity of currents in the stator phases of the machine and to prevent short-circuiting the source [62], [63].

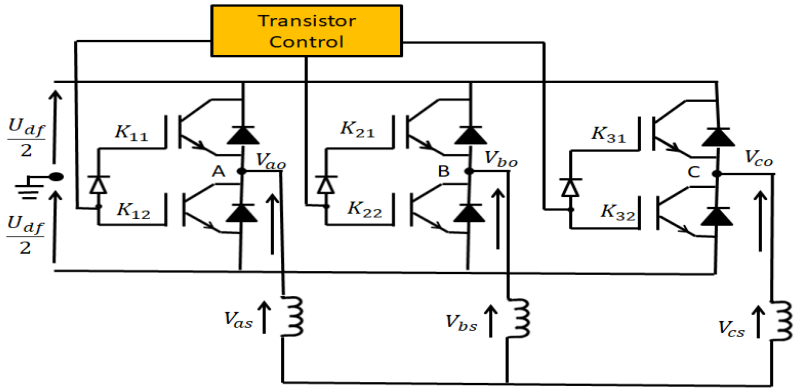

Figure 2.16. Representation of a two-level three-phase voltage inverter.

Considering an ideal converter [63], hence the following hypotheses:

- The switching of the components is instantaneous.
- The voltage drops at their terminals are negligible.
- The load is three-phase balanced and star-connected with isolated neutral point.

The single-phase voltages applied to the three phases of a three-phase load can be represented as follows:

$$\begin{cases} v_A = v_{AO} + v_{ON} \\ v_B = v_{BO} + v_{ON} \\ v_C = v_{CO} + v_{ON} \end{cases} \quad (2.71)$$

By addition, we obtain:

$$v_A + v_B + v_C = v_{AO} + v_{BO} + v_{CO} + 3v_{ON} \quad (2.72)$$

As the three-phase voltage system is symmetrical, it can be represented as:

$$v_A + v_B + v_C = v_{AO} + v_{BO} + v_{CO} + 3v_{ON} = 0 \quad (2.73)$$

Therefore:

$$v_{ON} = -\frac{1}{3}(v_{AO} + v_{BO} + v_{CO}) \quad (2.74)$$

By substituting (2.74) into (2.71), the resulting system is:

$$\begin{cases} v_A = \frac{2}{3}v_{AO} - \frac{1}{3}v_{BO} - \frac{1}{3}v_{CO} \\ v_B = -\frac{1}{3}v_{AO} + \frac{2}{3}v_{BO} - \frac{1}{3}v_{CO} \\ v_C = -\frac{1}{3}v_{AO} - \frac{1}{3}v_{BO} + \frac{2}{3}v_{CO} \end{cases} \quad (2.75)$$

The system (2.75) can be written in the following matrix form:

$$\begin{bmatrix} v_A \\ v_B \\ v_C \end{bmatrix} = \frac{1}{3}\begin{bmatrix} 2 & -1 & -1 \\ -1 & 2 & -1 \\ -1 & -1 & 2 \end{bmatrix}\begin{bmatrix} v_{AO} \\ v_{BO} \\ v_{CO} \end{bmatrix} \quad (2.76)$$

System (2.76) defines the mathematical model of the three-phase inverter, with the output line-to-line voltages expressed as:

$$\begin{cases} v_{AB} = v_A - v_B \\ v_{BC} = v_B - v_C \\ v_{CA} = v_C - v_A \end{cases} \quad (2.77)$$

2.10. 2 Pulse width modulation (PWM) control

The PWM. is realized by comparing a low frequency modulating wave (reference voltage) to a high frequency carrier wave of triangular shape. The switching times of the switches are determined by the intersection points between the carrier and the modulating wave. The schematic diagram of this technique is given in Figure 2.17.

Figure 2.18 shows the commutation instants of the switches, This technique is characterized by the following two parameters:

$$m = \frac{f_p}{f_r} \quad (2.78)$$

With:

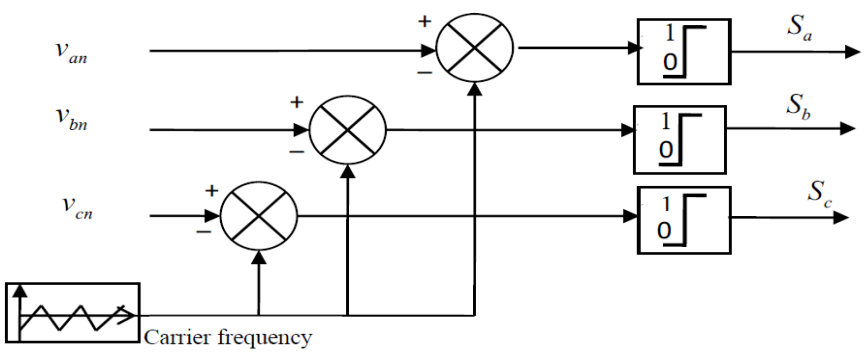

Figure 2.17. Principle diagram of the PWM.

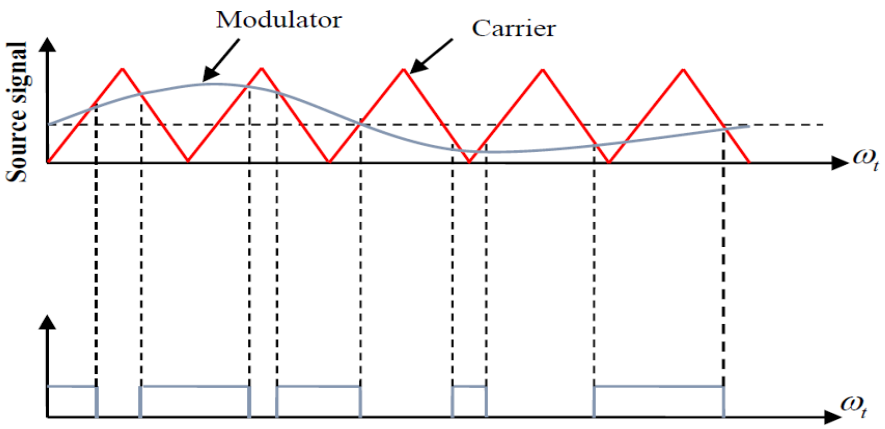

Figure 2.18. PWM technique.

m: The modulation index, defined as the ratio of the carrier frequency to the reference frequency.

$$r = \frac{V_r}{V_p} \tag{2.79}$$

Where:

r: The modulation rate (or adjustment coefficient) which gives the amplitude ratio of the modulator to the peak value of the carrier.

2.11 Conclusion

The primary objective of this chapter was to present the dynamic behavior of the electric vehicle based on the forces acting on the vehicle during uphill driving. The design of the vehicle depends on the characteristics of the traction motor, which are determined by the traction forces, the vehicle's acceleration, and the energy consumption of the electric vehicle.

Then, the modeling of the permanent magnet synchronous drivetrain, powered by a pulse-width modulation voltage inverter, was developed. Since the inverter can be considered as the connection element between the machine and the power source, and based on the variable topology modeling method, the semiconductors were considered as ideal switches. As a result, the inverter was modeled by a connection matrix whose elements are logical variables. After that, we presented the modeling of the energy sources (fuel cell and super-capacitor) as well as their sizing. This modeling will allow us to predict the performance of the traction chain.

Chapter 3: A New Multilevel Inverter Topology with Less Switching Devices for Electric Vehicle Applications

3.1 Introduction

The electric traction system typically consists of energy sources, such as super-capacitors and fuel cells, along with receivers, including the traction motor. Efficient energy management between these components necessitates the use of power electronic converters to regulate and condition the energy flow. Initially, we will examine the mathematical modeling of DC/DC converters linked to these sources, along with their control strategies. Subsequently, we will introduce a novel DC/AC converter design aimed at enhancing the performance of the traction system. To demonstrate the effectiveness of this converter, simulation results will be analyzed.

3.2 Energy source combination

Different electrical topologies are possible for combining these energy sources (fuel Cell and super-capacitor) [75] and managing the power of both sources:

They can have a single degree of freedom or two degrees of freedom. The degree of freedom represents an electrical quantity to be controlled (current and/or voltage). The choice of architecture is primarily justified by the simplicity of system implementation and the overall cost it entails [76].

At the energy source level, one of the roles of power converters is to control the power distribution between the fuel cell system and the super-capacitor.

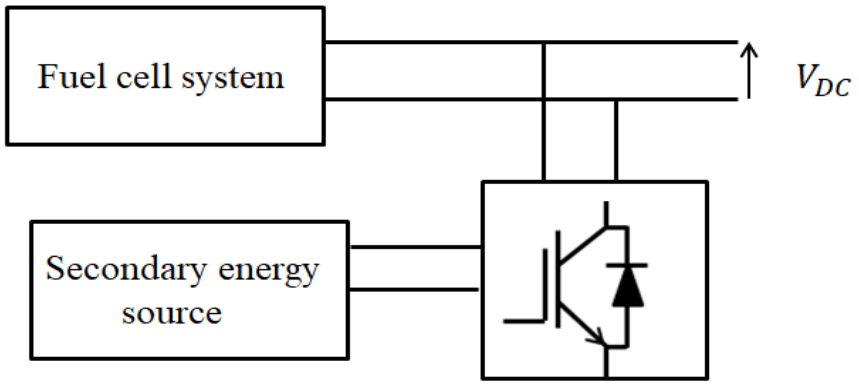

Figure 3.1. Architecture with a single reversible converter connected to the secondary source.

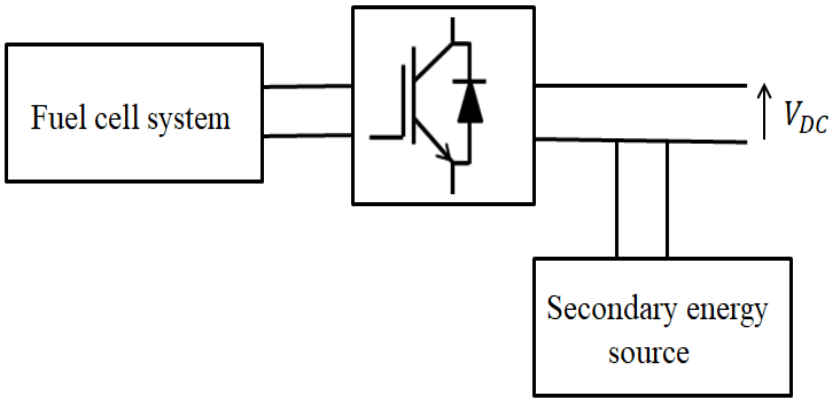

Figure 3.2. Architecture with a single non-reversible converter connected to the primary source.

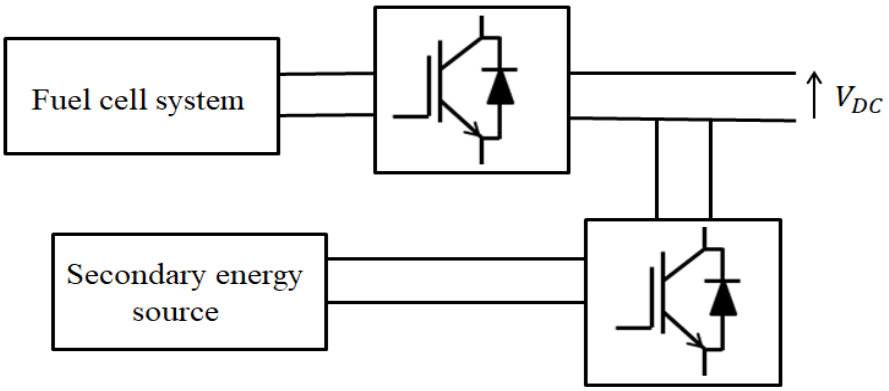

Figure 3.3. Dual-converter parallel architecture.

Furthermore, its local control typically regulates the current, voltage, and/or transmitted power to ensure the safety of the connected components. Three main hybrid architectures are considered [77]:

1. The fuel cell is directly connected to the DC bus and imposes its voltage. A bidirectional DC/DC converter is placed between the secondary source and the bus in Figure 3.1.

2. The secondary source is placed directly and imposes its voltage on the DC bus. A non-reversible DC/DC converter is used between the PAC and the bus in Figure 3.2.

3. The PAC and the super-capacitor are both connected via DC/DC converters in Figure 3.3. In this case, the bus voltage can be freely chosen (which is the case in this work).

3.3 DC/DC converter

3.3.1 DC/DC converter associated with the fuel cell

To use the fuel cell in the electric vehicle as an energy source, it must be connected to a fixed-voltage DC bus. In this case, the fuel cell voltage needs to be increased, as it is often lower than the DC bus voltage. Therefore, a boost converter is used to adapt the fuel cell voltage to that of the DC bus. The fuel cell system imposes specific constraints due to its design and operating principles.

3.3.1.1 Constraints imposed by the fuel cell (FC)

- **High current and low voltage**

To increase the power of the fuel cell (FC), multiple cells must be connected in series to achieve a higher voltage, or larger surface areas must be used to increase the current. For design reasons, the number of cells in series within a stack is limited to 100, resulting in a nominal voltage of around 60 V and an open-circuit voltage of 100 V. Improving the unit power of a stack requires increasing the surface area of the cells. For example, the company axane has presented two power ranges corresponding to two different fuel cell plate surface areas.

-The first one has a surface area of 80 cm² and provides a power output of 2.5 kW.

-The second one has a surface area of 550 cm² and provides a power output of 20 kW

The voltage of these two ranges remains within the same range, between 60 V and 100 V. Under these conditions, it is clear that we are in the high-current, low-voltage domain [78].

- **Low ripple in the output current**

To avoid reducing the fuel cell's performance and to improve its lifespan, the current ripple demanded by the converter connected to the fuel cell must be kept low, as it degrades the cell's efficiency [78]. These additional losses are negligible when the current ripple provided by the fuel cell is below 10%.

- **Response to load variations**

The time constant of the fuel cell during step load changes is limited by the mechanical dynamics of the compressor. We observe a time constant on the order of a few tens of

milliseconds. For each system, the duration of this regime mainly depends on the operating point and the amplitude of the steps. It can last up to several seconds, or even longer.

To summarize, three main criteria determine the type and architecture of the converter associated with the fuel cell:

1- Increase the fuel cell voltage to a level that allows it to be connected to the DC bus.

2- Handle the high current due to the nature of the fuel cell.

3- Reduce the current ripple delivered by the fuel cell

To meet these three criteria, a parallel architecture can be used. This architecture involves connecting multiple boost converters in parallel and staggering their control signals. This converter is called an “Interleaved Boost Converter”.

3.3.1.2 Two-phase interleaved boost converter

The interleaving technique is used to solve the problem associated with the high input current of the parallel converter in several applications (which is our case). Connecting the converters in parallel is an architecture that allows the current to be divided among several elementary cells. The current passing through each cell is then lower. This reduces the current stress on the components. This architecture also helps reduce the size of the magnetic elements by benefiting from the attenuation of the current ripple at the input of the interleaved converter, as well as reducing conduction losses in the converter [79]. Figure 3.4 shows the interleaved boost converter made up of N identical branches connected in parallel.

- **Sizing voltage**

$$V_K = V_D = V_S$$

- **Sizing current**

$$I_K = D\frac{I_E}{N}$$

$$I_D = (1 - D)\frac{I_E}{N}$$

Among the advantages of this architecture:

-Reduction of current stress on semiconductors.

-Reduction of the amplitude of input and output current ripples, as the equivalent switching frequency is multiplied by the number of branches.

-Reduction of power losses.

-Architecture better suited for fuel cells.

However, the drawbacks of this structure include a high number of components, higher cost, complex control, and the voltage constraints on the semiconductors remain the same as in a conventional Boost converter. The minimum number of branches results from a techno-economic trade-off, primarily analyzing the economic cost of components and power losses.

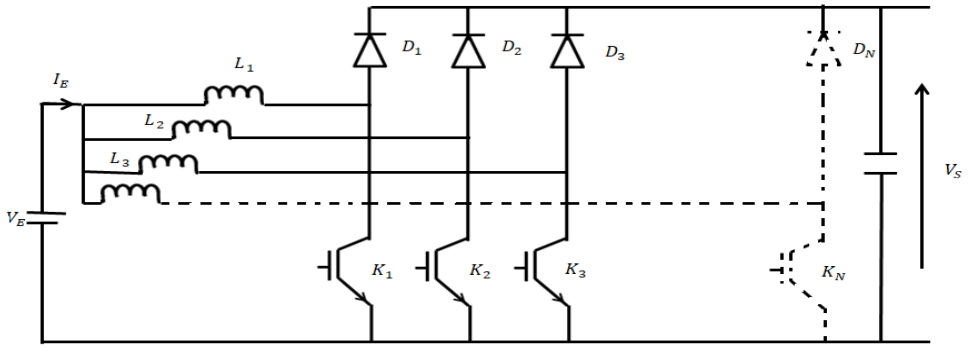

Figure 3.4. Interleaved boost converter architecture with n branches.

In our work, we used two branches of the fuel cell converter to avoid complicating the control scheme.

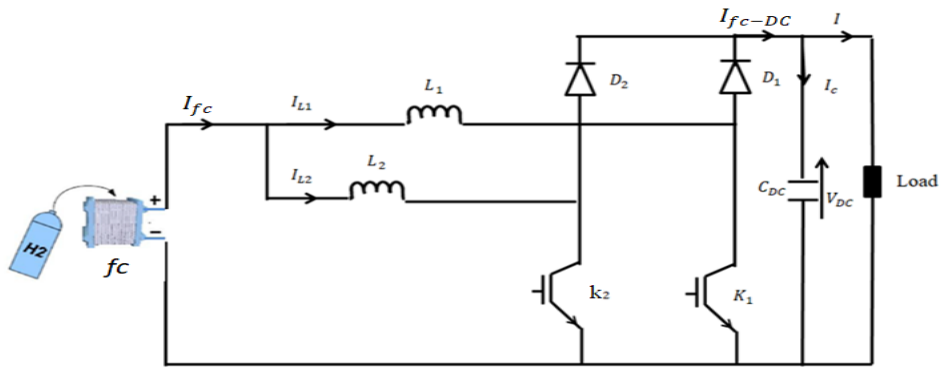

Figure 3.5. Interleaved boost converter with 2 branches associated with a fuel cell [81].

In the converter shown in Figure 3.5, each elementary boost converter is controlled with the same duty cycle D, with control signals phase-shifted by half a period. The average current flowing through each cell represents half of the input current, assuming both branches are identical. The output voltage remains the same as that of a conventional Boost converter for a given duty cycle [81].

3.3.1.3 Mathematical model of the interleaved DC/DC Boost converter

Based on the electrical schematic of the two-branch interleaved Boost converter shown in Figure 3.5, applying Kirchhoff's laws, we obtain the following model:

$$\begin{cases} L_1 \frac{dI_{L1}}{dt} = V_{fc} - V_{DC}(1-u_1) \\ L_2 \frac{dI_{L2}}{dt} = V_{fc} - V_{DC}(1-u_2) \\ I_{fc} = I_{L1}(1-u_1) + I_{L2}(1-u_2) \\ I_{fc} = I_{L1} + I_{L2} \\ C_{DC} \frac{dV_{DC}}{dt} = I_{fc} - I_{CH} \end{cases} \quad (3.1)$$

Where:

u_1 and u_2 are two binary control variables for switches K_1 and K_2, delayed by half a period relative to each other. They can take values of 1 or 0: 1 when the switch is closed, 0 when it is open.

I_{fc-DC} current from FC injected into the DC bus, it is discontinuous, and its average value is related to the current from FC by the following relation:

$I_{fc-DC} = (1-D)I_{fc-DC}$

Where D is the duty cycle of this chopper

3.3.1.4 Sizing of the Interleaved DC/DC Boost Converter

- **Inductance Calculation**

Generally, the inductances are identical $L_1 = L_2 = L$ for both branches to achieve optimal ripple. In our thesis work, the fuel cell is connected to a DC bus via the converter, where the bus voltage remains constant. The ripple of the fuel cell current as a function of the bus is given by the following relation:

$$\Delta I_{fc} = \begin{cases} \frac{D(1-2D)V_{DC}}{L_f} & si \quad D \leq 0.5 \\ \frac{(2D-1).(1-D)V_{DC}}{L_f} & si \quad D \geq 0.5 \end{cases} \quad (3.2)$$

For a duty cycle D=0.25 and D=0.75, the maximum ripple is given by:

$$\Delta I_{fc\_max} = \frac{V_{DC}}{8L_f} \quad (3.3)$$

The minimum inductance is:

$$L = \frac{V_{DC}}{8\Delta I_{fc\_max} f} \quad (3.4)$$

We take $V_{DC} = 570V, and\ \Delta I_{fc\_max}$= 3A, f=10KHZ, therefore L=2mH

- **Capacitor capacitance calculation**

It is the same as the classic boost, the capacitance value is calculated using the following equation:

$$c = \frac{\alpha I_{CH}}{\Delta V f} \quad (3.5)$$

α: The duty cycle (around 2.5)

I_{CH}: Charging current (max value = 80A from the charging cycle)

f: Switching frequency (10 kHz)

ΔV: Maximum voltage ripple (5V)

We find:

C= 0.004F

3.3.1.5 Control of the interleaved boost converter associated with the fuel cell

Due to the low-voltage nature of the fuel cell (FC), it is necessary to increase its voltage. The Boost converter and its various types are current-voltage converters well suited to the fuel cell for two main reasons:

-They naturally provide voltage step-up.

-They have an inductive nature at the input, which helps reduce current ripple

The converter used is of the interleaved type, where the current supplied by the fuel cell is divided among the different branches of the converter to minimize the total current ripple.

Two control techniques are proposed. The first technique consists of using two cascaded loops: The outer voltage loop compares the reference voltage value with the measured value and sets a current reference in the inductors. The inner current loop

compares the reference with the actual current in the inductors, and the error is corrected to determine the duty cycle. A PWM modulator converts the duty cycle into a pulse control signal for the converter's transistors Figure 3.6. In this technique, all elementary transistors switch with the same duty cycle, and only one point is used for current measurement. The presence of parasitic resistances is considered in the circuit. If these resistances are identical, the elementary currents will automatically balance. In the case of a high number of interleaved branches, the number of current sensors can be reduced by measuring at a single point instead of m points in m elementary branches [78]. In the second technique, the reference current is calculated by the voltage loop and compared with the two elementary currents Figure 3.7. This solution ensures absolute balance accuracy. However, it requires using as many sensors as the number of interleaved branches. The circuit becomes more complex, not only due to the number of sensors but also because of the number of regulators [78].

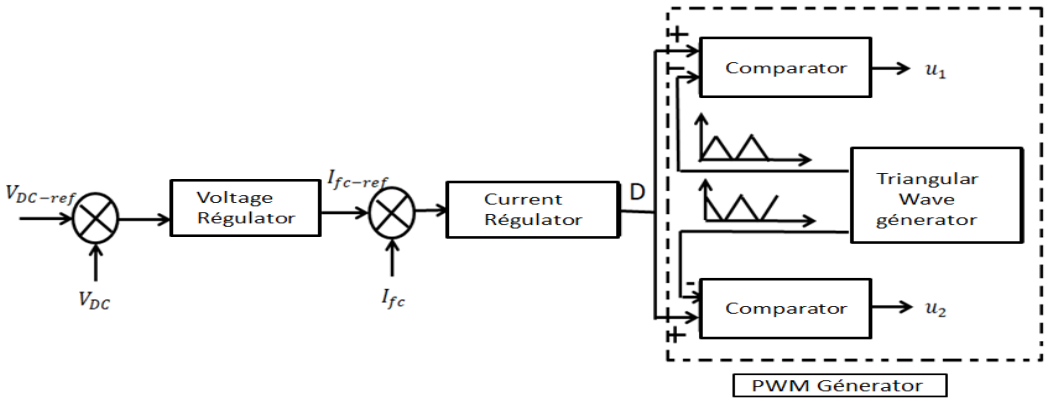

Figure 3.6. Interleaved converter control without elementary current balancing [81].

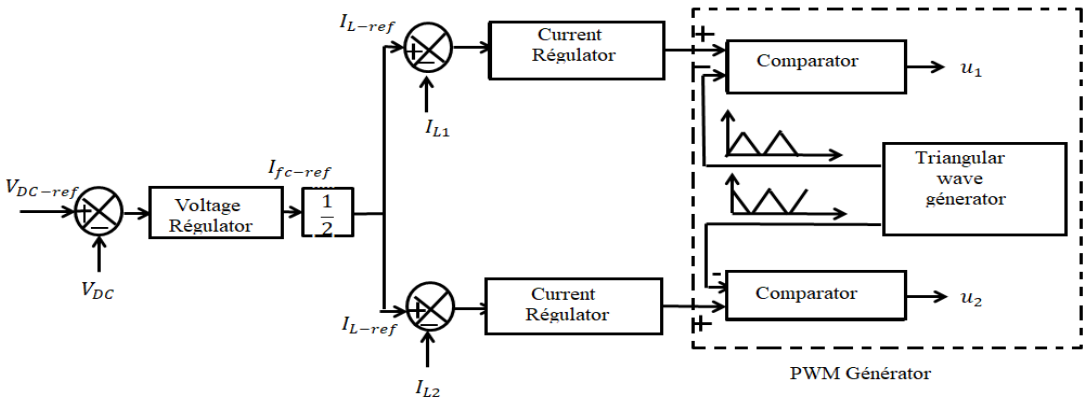

Figure 3.7. Interleaved converter control with elementary current balancing [81].

3.3.2 Converter associated with super-capacitor

To ensure the connection between the DC bus and the storage element (super-capacitor), a DC/DC converter is necessary. This converter also controls the power supplied and absorbed. The super-capacitor can be charged or discharged, which requires the use of a bidirectional current converter.

In our work, we have chosen a two-quadrant bidirectional converter Figure 3.8. This converter consists of a switching cell with two switches (K_1, K_2) that is bidirectional in current. Each switch is a controllable transistor that can be opened and closed, with diodes mounted in antiparallel [80].

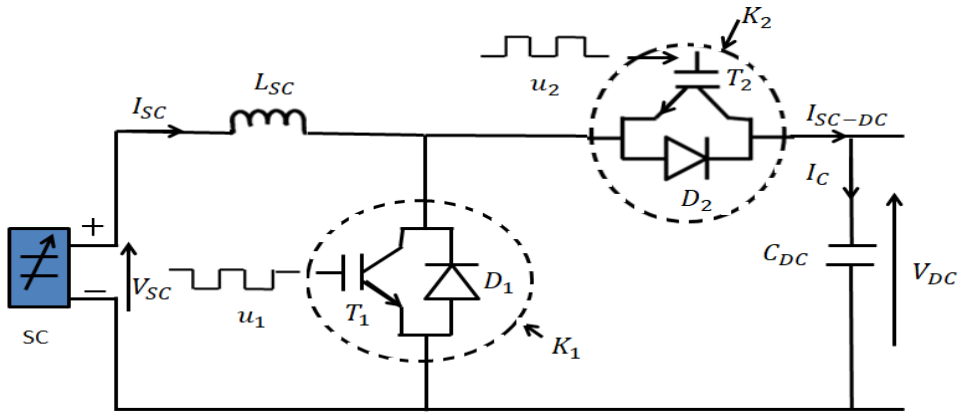

Figure 3.8. Two-quadrant chopper connected to super-capacitor [81].

3.3.2.1 Mathematical model of the DC/DC buck-boost converter

This converter has two operating modes: a buck mode when the super-capacitor receives energy from the DC bus and a boost mode when the super-capacitor supplies energy. Let u_1 and u_2 be the binary variables representing the states of the switches (K_1 and K_2), where state 1 corresponds to a closed switch and state 0 corresponds to an open switch. The analysis of the converter's operation allows us to establish the following differential equations [81].

Boost Operating Mode ($I_{sc} > 0$)

$$\begin{cases} L_{sc}\frac{dI_{sc}}{dt} = V_{sc} - V_{DC}(1-u_1) \\ I_{sc-DC} = I_{sc}(1-u_1) \end{cases} \quad (3.6)$$

Buck Operating Mode ($I_{sc} < 0$)

$$\begin{cases} L_{sc}\frac{dI_{sc}}{dt} = V_{sc} - V_{DC}(u_2) \\ I_{sc-DC} = I_{sc}(u_2) \end{cases} \quad (3.7)$$

V_{sc}: Voltage at the terminals of the super-capacitor

I_{sc}: Super-capacitor current

I_{sc-DC}: Super-capacitor current injected into the DC bus.

L_{sc}: Smoothing inductance.

u_1: Control signal of switch K_1

u_2 : Control signal of switch K_2

To avoid a short circuit of the voltage source, the signals u_1 and u_2 must be complementary ($u_2 = \bar{u}_1 = 1 - u_1$) Thus, we can write a single system of equations by setting $u_1 = u$

$$\begin{cases} L_{sc}\frac{dI_{sc}}{dt} = V_{sc} - V_{DC}(1-u) \\ I_{scDC} = I_{sc}(1-u) \end{cases} \quad (3.8)$$

3.3.2.2 Control of the buck-boost converter associated with the super-capacitor

Unlike the interleaved boost converter of the fuel cell, the super-capacitor's buck-boost converter is current-controlled using a conventional PI regulator Figure 3.9.

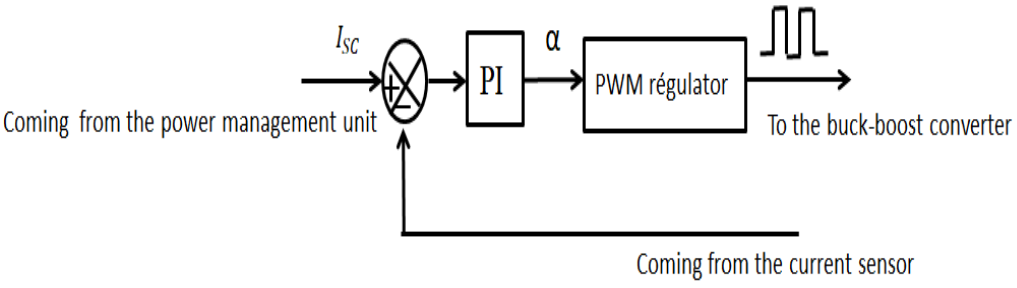

Figure 3.9. Super-capacitor current regulation diagram [81].

3.4 Multi-level inverter

The classic inverters have a lot of constraints so the electronic field started to need an inverter that can produce high performance and an almost sinusoidal output. As a solution, the evolution of the multi-level inverter has started [82].

The multi-level inverter is a power circuit that generates high-power outputs with at least three states (three levels) the more levels that can be generated, the closer the output is to the sinusoidal waveform. The number of levels in multi-level inverters is improved by increasing the number of switches and other components, depending on their topologies [83]. There are several topologies for the multi-level inverter. The neutral point clamp NPC, flying capacitor FC, and cascaded H-bridge CHB are the most often used in the field Figure 3.10.

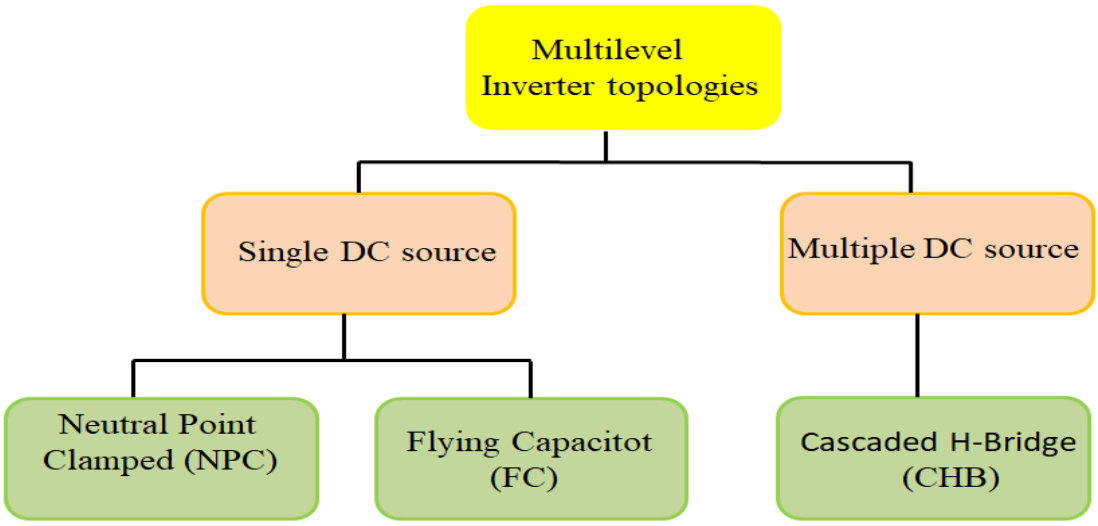

Figure 3.10: Multi-level inverter topologies according to their source type.

3.4.1 Multi-level inverter topologies

3.4.1.1 Diode clamped topology

The neutral point clamped multi-level inverter topology known also by the name of diode clamped, this topology contains one DC source and multiple semiconductor switches and diodes, the function of clamped diodes is a level shifter. The NPC can generate outputs that have more than three levels. To increase the number of levels we

need to increase the number of specific components such as the switches and the diodes. Figure 3.11 shows the three-level structure of the NPC topology [84].

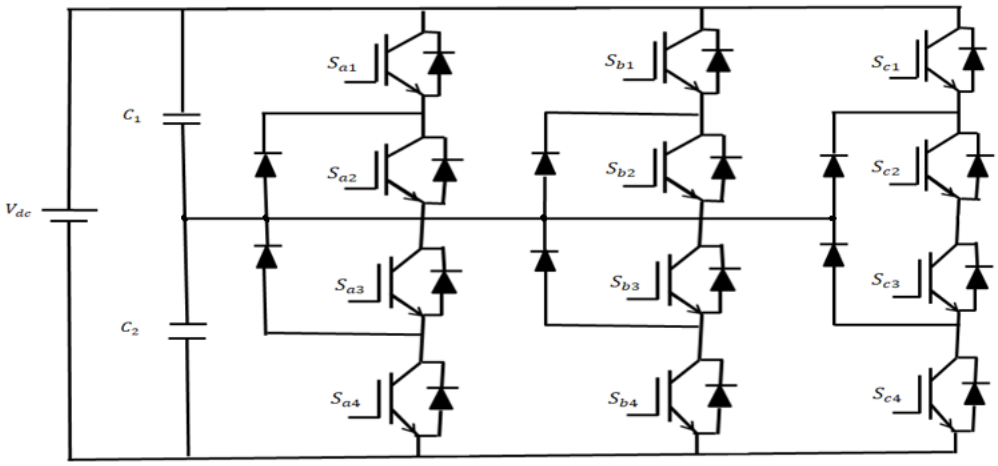

Figure 3.11. NPC multilevel inverter topology circuits.

While the diode-clamped configuration offers extendibility, The three-level configuration represents the widely favored configuration within the industry, owing to the challenges of capacitor voltage balancing as the total number of voltage levels increases 53, 75 and 76. In practice, the NPC topology is chiefly applied to motor drive systems, but it has also been applied in photovoltaic systems [85] and grid applications [86].

3.4.1.2 Flying capacitor topology

This topology was originally proposed in 1992 by T.A. MEYNARD, H. FOCH in [87]. It is regarded as a suitable alternative to the diode-clamped topology. The converter consists of several switching devices arranged in series, with one or more capacitors connected to each leg of the converter, as illustrated in the figures. In this topology, the capacitors are isolated from the DC bus, hence the term flying capacitor converter.

The primary drawback of this topology lies in the huge quantity of capacitors required, particularly in higher-level structures, as well as the need for additional circuits to pre-charge them. It has been implemented in high-power domains, with active power filtering being a key example [88]. Figure 3.12 shows the structure of three-level flying capacitor topology.

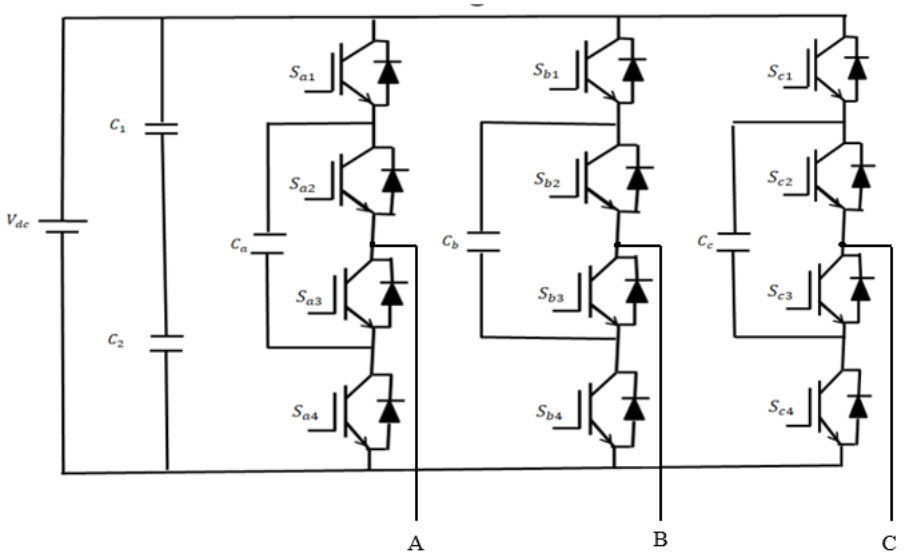

Figure 3.12. Three level flying capacitor topology.

3.4.1.3 Cascaded H-bridge topology

The cascade H-bridge (CHB) configuration was originally suggested in 1975 by Baker Richard H. and Bannister Lawrence H. [89]. This configuration is realized by series connection of multiple H-bridge cells, each supplied by an independent isolated DC source. Owing to its inherently modular structure, the CHB inverter enables decentralized implementation of control and protection schemes at the cell level, thereby ensuring scalability while substantially reducing both design complexity and overall manufacturing cost. Figure 3.13 illustrates the structure of CHB converter topology.

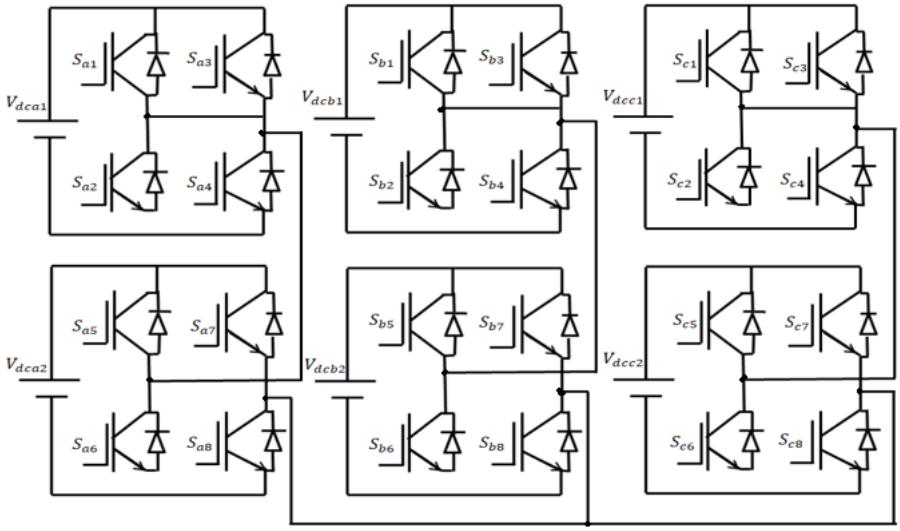

Figure 3.13. Three-phase generalized cascaded h-bridge converter topology.

The cascade H-bridge topology has been used in multiple applications such as photovoltaic systems [90], motor drive systems [91], electric vehicles [92].

3.4.2 Symmetric configurations of multilevel topologies

The flying-capacitor, diode-clamped, and cascaded H-bridge structures are categorized as symmetrical multilevel inverters, characterized by equalized DC-link capacitor voltages and uniform voltage blocking requirements across all semiconductor devices. Their primary limitation is the exponential increase in the number of switching devices with higher voltage levels. A comparative evaluation of the device count for each topology is summarized in Table 3.1, assuming identical power ratings for all switches.

Table 3.1: Comparative analysis of fundamental multilevel inverter topologies [89].

	Topology	T	D	m
3 Level	Diode clamped	4	6	2
	Flying capacitor	4	4	2
	Cascaded h bridge	4	4	2
5 Level	Diode clamped	8	20	4
	Flying capacitor	8	8	4
	Cascaded h bridge	8	8	4
7 Level	Diode clamped	12	42	6
	Flying capacitor	12	12	6
	Cascaded h bridge	12	12	6
m+1 Level	Diode clamped	2m	m^2+m	m
	Flying capacitor	2m	2m	m
	Cascaded h bridge	2m	2m	m

The data table demonstrates that the cascaded H-bridge inverter exhibits superior performance, especially for higher voltage-level implementations.

3.4.3 Asymmetric configurations of multilevel topologies

In recent times, increasing attention has been directed toward asymmetric multilevel inverter topologies, primarily to minimize the number of switching devices. Structurally, most asymmetric configurations resemble their symmetric counterparts; the distinction lies in the unequal DC input voltages assigned for each module and the corresponding voltage/current ratings of the semiconductor devices. Nevertheless, these topologies exhibit different operational characteristics, particularly in terms of the number of achievable voltage levels.

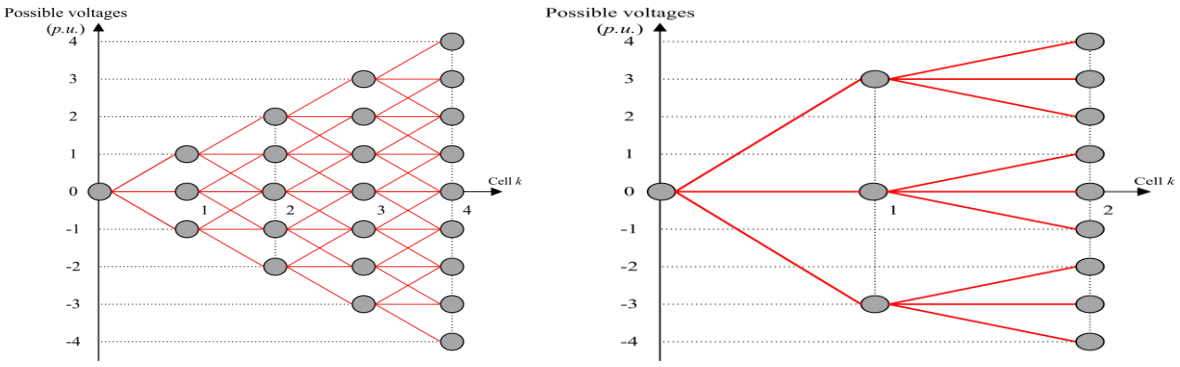

Figure 3.14. Possible voltage levels using 9-level symmetric and asymmetric topologies.

3.4.4 SPWM Technique

Sinusoidal pulse width modulation (SPWM) represents the most widely employed modulation technique for multilevel inverter control due to its simplicity and ability to achieve high power quality. Its principal drawback, however, lies in the elevated switching frequency, which adversely impacts the lifespan of the semiconductor devices in multilevel converters. The underlying principle of SPWM involves the use of multiple carrier signals, phase-shifted across several levels, which are compared with a sinusoidal reference signal. As illustrated in Figure 3.15, the comparison between the carriers and the reference defines the gating signals applied to the switching devices of the multilevel inverter.

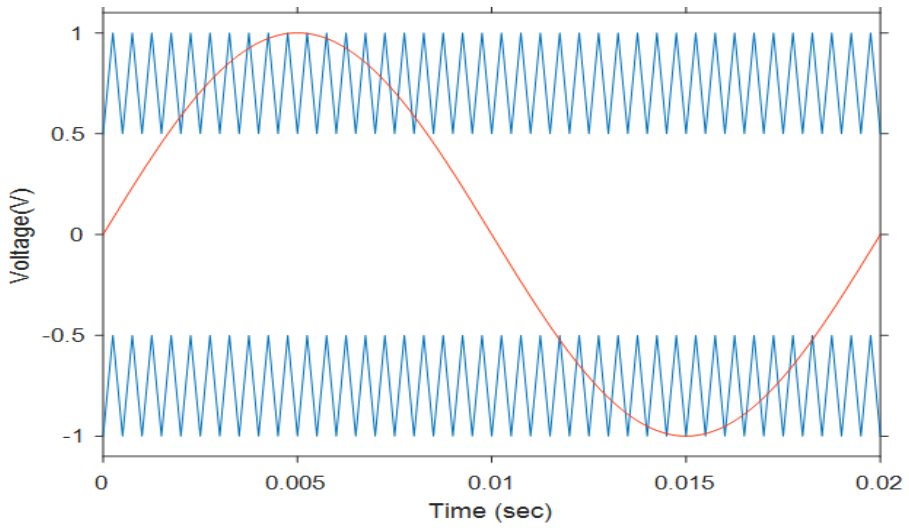

Figure 3.15. Sinusoidal pulse width modulation for N level inverter.

3.4.4.1 Level shifted PWM

A. Phase disposition PWM (PD-PWM)

The phase disposition PWM (PD-PWM) technique employs multiple triangular carrier signals along with a single sinusoidal reference per phase. To synthesize an output with m potential levels, the method requires m–1 carriers of identical amplitude and frequency. Figure 3.16 illustrates the carrier disposition corresponding to a five-level inverter.

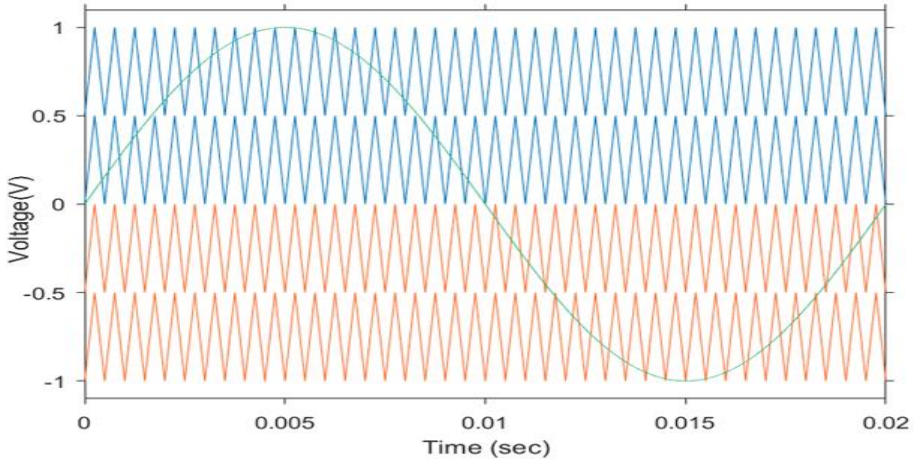

Figure 3.16. Carrier arrangement for PD-SPWM.

B. Phase opposition disposition PWM (POD-PWM)

Figure 3.17 illustrates the carrier arrangement of the phase-opposition disposition (POD-PWM) technique, in which the carriers above the zero reference are phase-shifted by 180° relative to those below it.

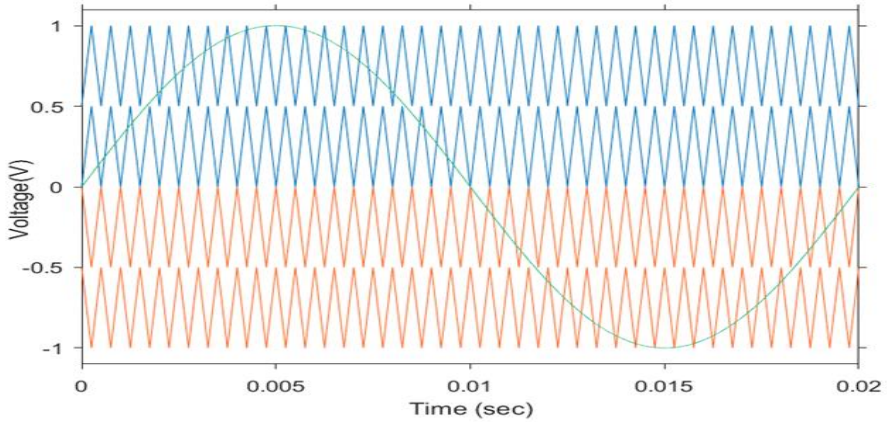

Figure 3.17. Carrier arrangement for POD-SPWM.

C. Alternate phase opposition disposition PWM (APOD-PWM)

The alternate phase-opposition disposition (APOD-PWM) technique is realized by introducing a 180° phase shift between adjacent carrier signals, as shown in Figure 3.18.

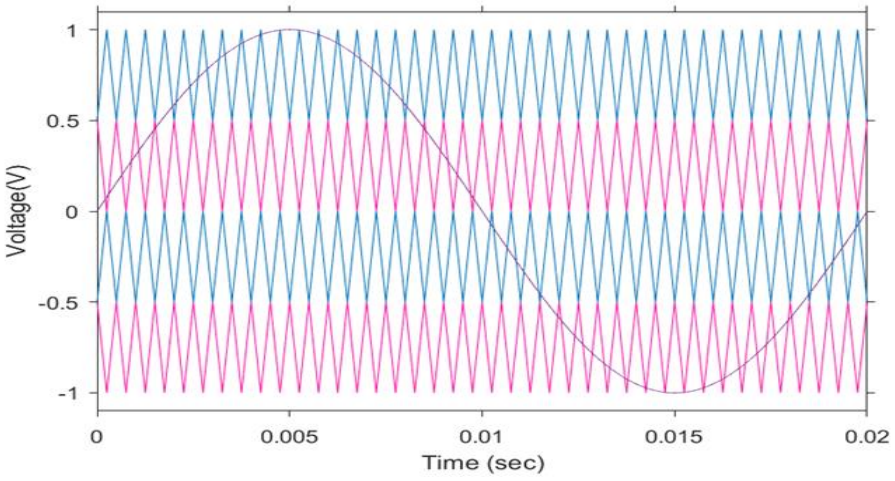

Figure 3.18. Carrier arrangement for APOD-SPWM.

3.4.4.2 Phase shifted PWM (PS-PWM)

Phase-shifted PWM is a multi-carrier modulation method usually used for flying capacitor and cascaded H-bridge inverter topologies mainly due to their modularity.

3.5 The proposed cascaded topology

The cascade H-bridge multilevel configuration has many advantages over clamped diode and ying capacitor configurations, but it has a significant drawback for higher voltage levels. It raises production costs by requiring a lot of heat sinks, protection circuits, and switching devices. This work proposes a new topology that uses non-equal DC input sources to solve this issue (also known as asymmetric topology.) and making use of a hybrid configuration that combines bidirectional switches with a basic H-bridge topology to provide greater voltage levels than traditional topologies while using fewer switching devices. The structure of the suggested 21-level inverter is depicted in Figure 3.19.

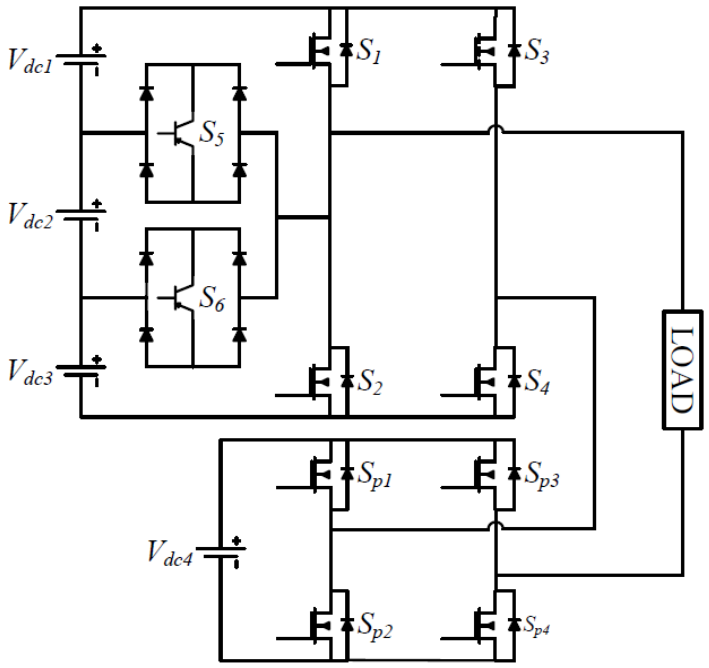

Figure 3.19. The suggested 21- level inverter configuration.

The proposed 21- level inverter consists of two cells with H bridges. The upper cell consists of a basic H-bridge made up of four power switches (S_1, S_2, S_3, S_4), two bidirectional switches (S_5, S_6) along with three DC power sources, each having the same voltage value, the bidirectional switches S_5 and S_6 function to control the connection of the DC sources, enabling the construction of the required waveform of the staircase

output voltage, this inverter cell may produce 7 different voltage outputs ± 3Vdc, ± 2Vdc, ± Vdc and 0. The lower cell is implemented as a basic H-bridge composed of four power switches that are linked to a separate DC source, this cell may produce three different voltage output +Vdc, 0 and –Vdc. The output voltage levels are defined by

$$N = 2S + 1 \tag{3.9}$$

Where N represents the inverter level, while S denotes the number of DC voltage sources. The inverter output voltage V_{in} is the total sum of the individual inverter outputs

$$V_{in} = V_{cell1} + V_{cell2} \tag{3.10}$$

Table 3.2 presents the allowed switching configurations for every possible combinations.

It is important to note that these combinations are only applicable under the conditions listed below:

$$V_{dc1} = V_{dc2} = V_{dc3} \tag{3.11}$$

$$V_{dc4} = 7 \times V_{dc1} \tag{3.12}$$

This implies that the voltage source for the second cell must be seven times that of the first cell, to achieve 21 voltage levels. From the proposed topology and equation (3.12), it is evident that the switching devices in the second cell experience higher voltage stress compared to those applied in the upper bridge. Hence, switching devices with high voltage ratings are required for lower bridges.

Table 3.2: Output voltage levels (p.u.) with their respective conducting switches for the suggested 21-level inverter.

Voltage, p.u.	Switches in ON state	Voltage, p.u.	Switches in ON state
10	S_1, S_4, S_{p1}, S_{p4}	–10	S_3, S_2, S_{p2}, S_{p3}
9	S_4, S_5, S_{p1}, S_{p4}	–9	S_3, S_6, S_{p2}, S_{p3}
8	S_4, S_6, S_{p1}, S_{p4}	–8	S_5, S_3, S_{p2}, S_{p3}

7	S_2, S_4, S_{p1}, S_{p4}	–7	S_2, S_4, S_{p2}, S_{p3}
6	S_3, S_5, S_{p1}, S_{p4}	–6	S_6, S_4, S_{p2}, S_{p3}
5	S_3, S_6, S_{p1}, S_{p4}	–5	S_5, S_4, S_{p2}, S_{p3}
4	S_2, S_3, S_{p1}, S_{p4}	–4	S_1, S_4, S_{p2}, S_{p3}
3	S_1, S_4, S_{p2}, S_{p4}	–3	S_2, S_3, S_{p2}, S_{p4}
2	S_4, S_5, S_{p2}, S_{p4}	–2	S_3, S_6, S_{p2}, S_{p4}
1	S_4, S_6, S_{p2}, S_{p4}	–1	S_3, S_5, S_{p2}, S_{p4}
0	S_2, S_4, S_{p2}, S_{p4}	0	S_2, S_4, S_{p2}, S_{p4}

In this work, we use the PD-SPWM modulation technique. Figure 3.20 illustrates the principle of sinusoidal PWM (21-level inverter).

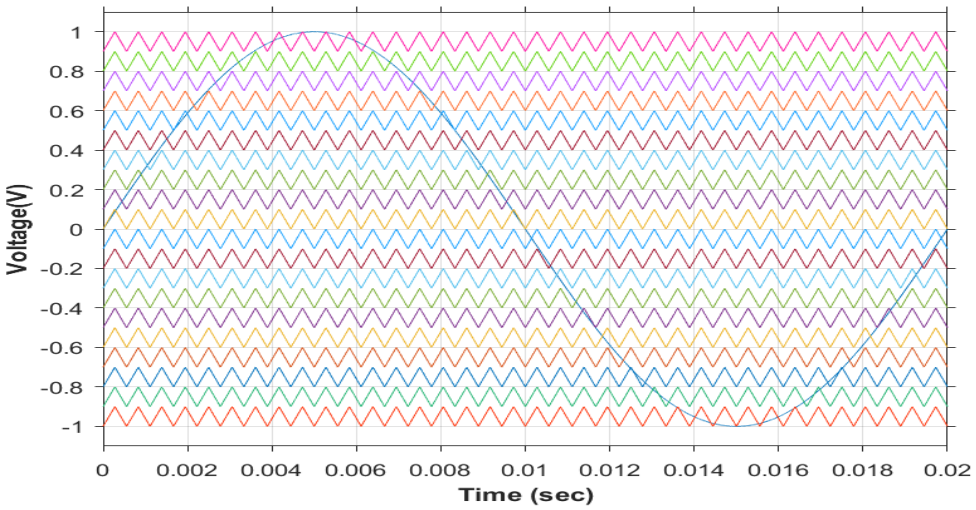

Figure 3.20. Principle of Sinusoidal PWM 21-Level Inverter.

3.6 General schematic of the converter employed

The presence of two energy sources with different characteristics on board the vehicle requires the use of static converters to condition the energy from these sources [93]. The primary objective of this energy conditioner is to provide a variable DC bus voltage level. The minimum voltage to be supplied corresponds to the voltage of the

sources, which is in turn closely related to the starting voltage required by the traction motor [94]. This minimum voltage level must ensure the vehicle's operation at low speed, i.e., in urban driving mode. The maximum voltage level, on the other hand, is defined by the maximum speed of the motor, which corresponds to the vehicle's maximum speed in highway or road mode [95].

Figure 3.21 illustrates the overall structure of the converter used.

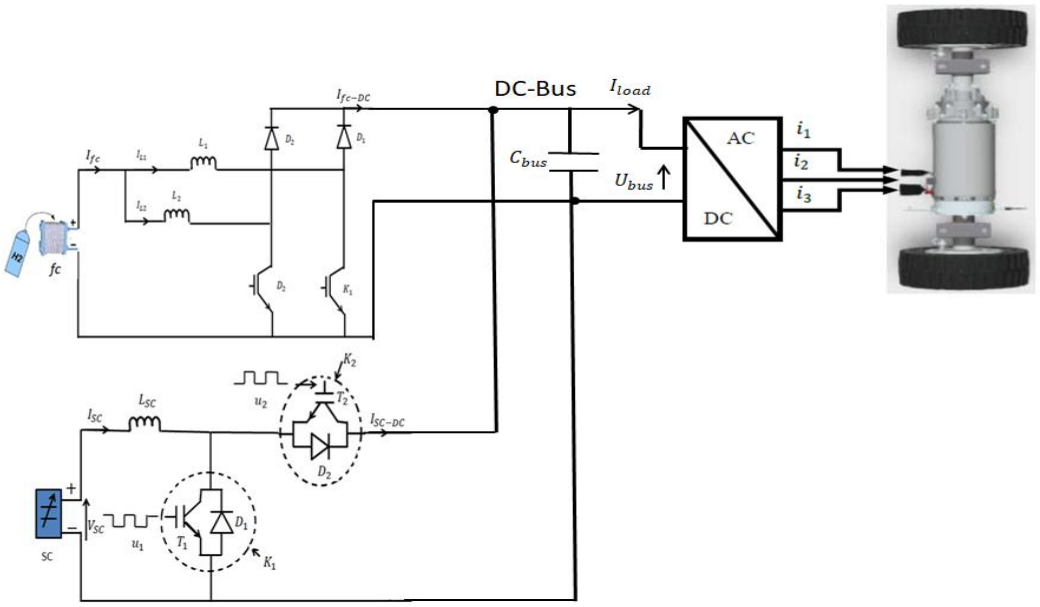

Figure 3.21. The complete architecture of the employed converter.

3.7 The concept of energy management within the system

In the proposed hybrid power system (fuel cell and super-capacitor), both energy sources are interfaced with a Direct Current (DC) bus via dedicated power converters.

The primary objective is to maintain a stable and adequate DC bus voltage to supply the inverter, utilizing both the fuel cell and the super-capacitor as energy sources [96]. The resulting DC bus voltage ($V_{DC\_}$ inverter) serves as the input voltage to the inverter.

In our case, a strategy will be tested and simulated to verify certain criteria, such as minimizing fuel consumption and maintaining a good state of charge of the super-capacitor. This strategy is: Energy management through frequency separation.

3.7.1 Energy management through frequency separation

In this strategy, the approach is based on the constraints imposed by the hybrid power system, including power and response time limitations in the dynamic operation of the fuel cell, as well as state-of-charge limits for the super capacitor pack [24].

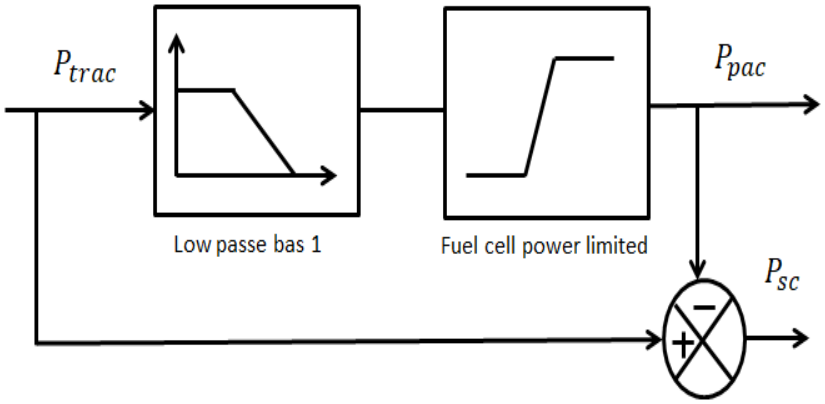

Figure 3.22. Energy management by frequency separation.

-The power of the fuel cell must be limited between a maximum power P_{fc-max} and a minimum power P_{fc-min}

-The fuel cell has a slow dynamic response compared to super-capacitor due to the large mechanical time constant of the air compressor.

To limit the dynamics of the fuel cell reference current, the DC bus reference power is passed through a low-pass filter to generate the fuel cell reference. The difference between these two references is used to determine the super-capacitor reference power Figure 3.22.

According to this strategy, power demands are divided into two categories: those with fast dynamics are supplied by the super-capacitor pack, while those with slow dynamics are handled by the fuel cell.

3.8 Simulation results

Figure 3.23 illustrates the evolution of three voltage levels in a hybrid fuel cell/super-capacitor architecture, with energy management based on frequency control. The DC bus voltage remains nearly constant around 570 V, which is critical for ensuring reliable power delivery to the load. This indicates that the energy management system

effectively regulates and stabilizes the bus voltage despite fluctuations in the power sources.

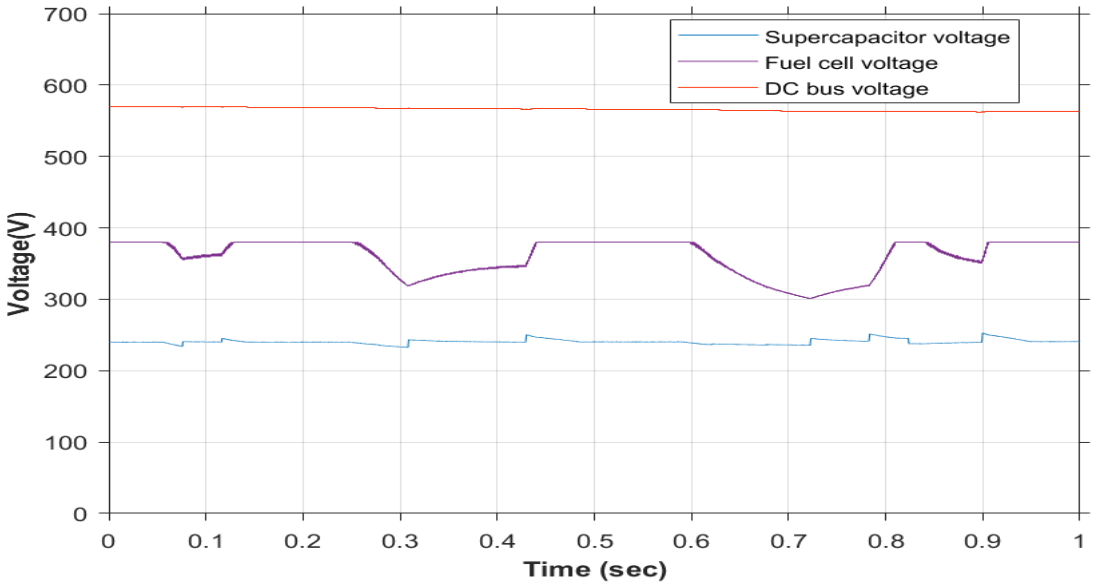

Figure 3.23. DC voltage in a hybrid Fuel Cell/ super-capacitor architecture using frequency-based energy management

To highlight the function of the boost and buck-boost DC/DC converters in ensuring voltage level adaptation between the two energy sources and the DC bus.

Figures 3.24 and 3.25 illustrate that the output voltage of the two converters reaches and maintains the reference level of 570 V

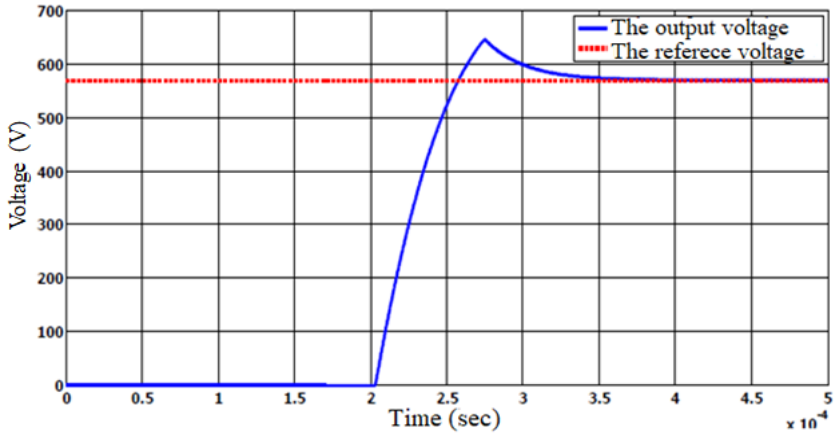

Figure 3.24. Dynamic response of the boost converter output voltage.

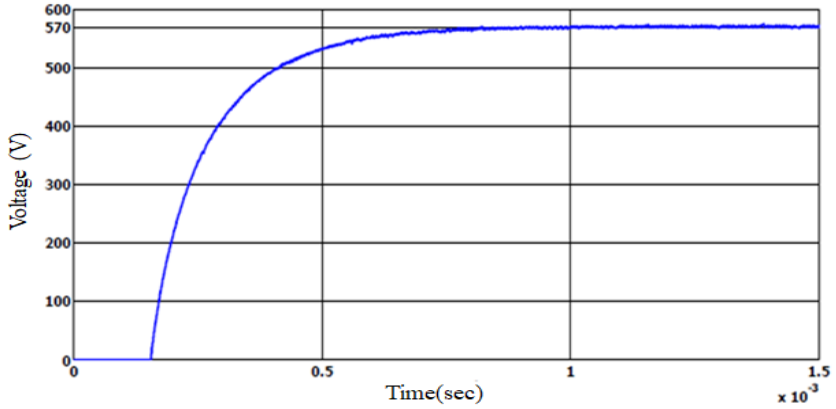

Figure 3.25. buck-Boost Converter Output Voltage.

To confirm the efficiency of the recommended topology. A comparative study has been done in this section to demonstrate the merits of the proposed topology over of tow-level inverter topology. Total Harmonic Distortion (THD) was selected as a quality measure to evaluate the quality of the generated output voltage and is calculated using the following equation.

$$THD\% = \frac{\sqrt{\sum_{n=3}^{50} H_n{}^2 H_1}}{\times} 100 \qquad (3.13)$$

Figure 3.26 (a) shows the voltage wave forms generated by tow-level inverter topology. Figure3.26 (b) displays the spectra of the output voltage waveforms, showing a total harmonic distortion (THD) of 73.39%.

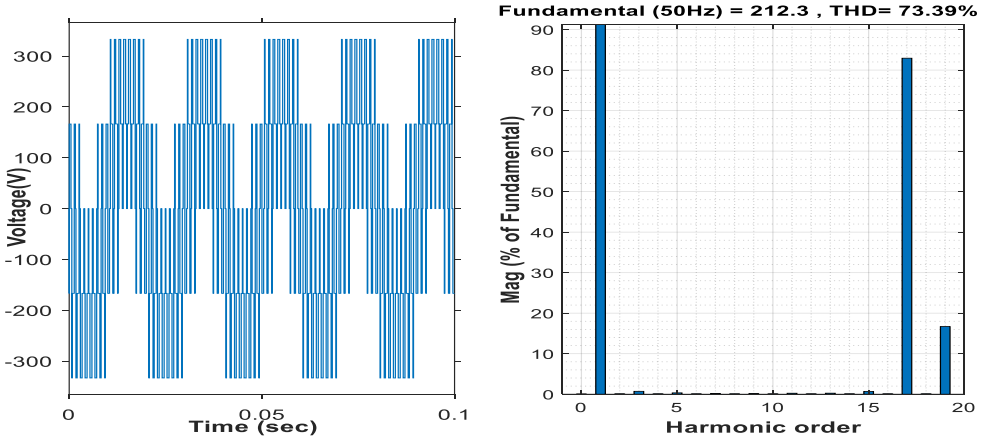

(a) (b)

Figure 3.26. (a)Voltage waveform produced by two-level inverter, (b) The spectra of the output voltage.

Figure 3.27 a, b show the output voltage wave form of a 21-levels inverter, respectively. The upper cell produce the magnitudes of voltage ±36.5, ±73, ±109.5 and 0, lower cell produce the magnitudes of voltage +255.5, 0 and -255.5. Figure 3.27 (c) shows total output voltage is sum of 2 cells inverter with the peak of 365. Figure 3.27 (d) displays the spectra of the output voltage waveforms, showing a total harmonic distortion (THD) of 6.13 %.

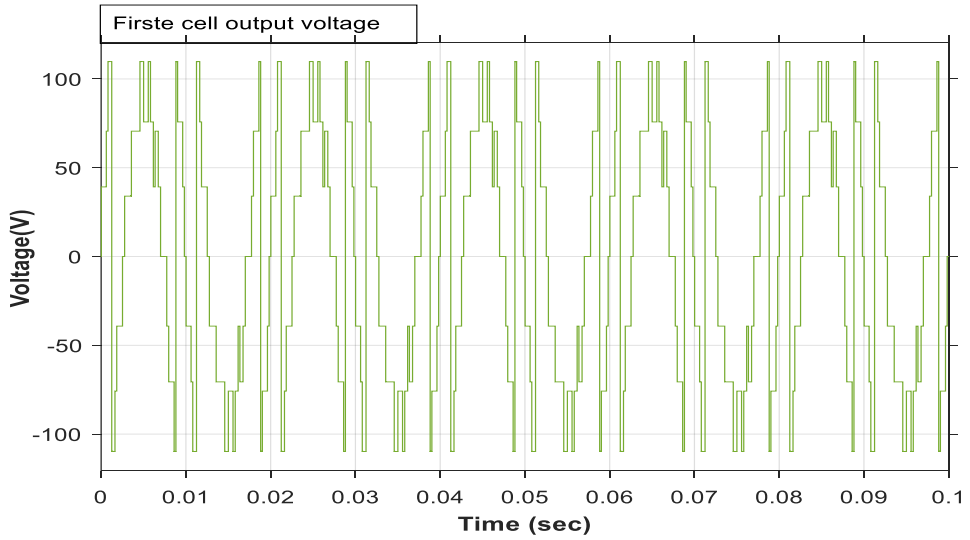

(a)

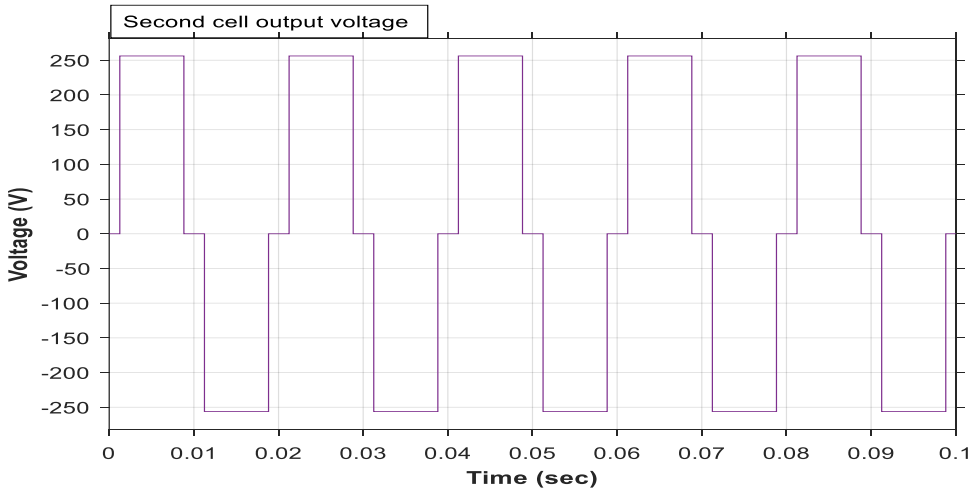

(b)

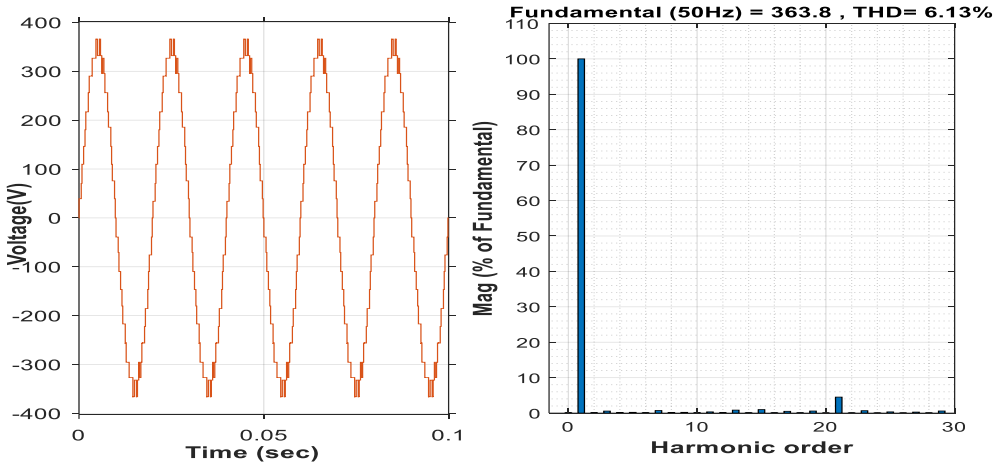

(c) (d)

Figure 3.27. The output voltage wave form of a 21-levels inverter; (a) upper cell output voltage; (b) lower cell output voltage; (c) total output voltage; (d) harmonic spectrum for output voltage.

Table 3.3 clearly demonstrates and gives an overview of the actual waveform quality along with its fundamental component. The THD emphasizes the benefit of the level. It is also noted that increasing the inverter level enhances the inverter's output signal.

Table 3.3: Distortion factors of each type of inverter.

Inverter level	Output voltage (THD%)
2-levels	73.39
21-levels	6.13

3.9 Conclusion

This chapter is divided into two sections. The first focuses on the modeling of the DC/DC converters linked to the energy sources (fuel cell and super-capacitor), along with their control strategies. The second part presents the new proposed topology of a multilevel DC/AC converter. At the end, a simulation is conducted to evaluate the performance of these converters.

Chapter 4: Nonlinear Control for Electric Vehicle Traction

4.1 Introduction

Classical control laws can be insufficient because they are not robust, especially when the requirements for accuracy and other dynamic characteristics of the system are strict. It is necessary to use control laws that are insensitive to disturbances, parameter variations, and nonlinearities. When the controlled system is subject to disturbances and parameter variations, a self-adaptive solution can be used. By readjusting the controller parameters, it maintains predefined performance levels despite these disturbances and variations. However, this approach has the drawback of often requiring a complex implementation.

In this first part of the chapter, we present the concepts of the new variable structure control technique known as sliding mode control. We describe the methodological aspects necessary for understanding this technique by providing a review of the general foundations and sliding mode control. Finally, we conclude with the application of this technique to the PMSM. However, the chattering phenomenon represents its main drawback. To address this issue, another control technique is used, which combines the advantages of both types of controllers while eliminating the chattering effect. This technique is called fuzzy sliding mode control and will be the focus of the second part of this chapter. Finally, we present the simulation results of the powertrain.

4.2 General Concepts of Sliding Mode Control Theory

The switchings of the variable structure control are performed based on the state variables, which are used to create a 'manifold' or 'surface' known as the sliding surface. Sliding Mode Control (SMC) consists of driving the state trajectory toward the sliding surface and making it evolve with a certain dynamic until reaching the equilibrium point [97]. A sliding surface is a surface S on which the system follows the desired evolution (where the error evolves). When the state is maintained on this surface, the system is said to be in the sliding regime. Thus, as long as the sliding conditions are met, the system's dynamics remain insensitive to parameter variations of the process, modeling errors (within a broader range compared to classical control approaches), and certain disturbances [98].

4.3 The objective of sliding mode control

The objective of Sliding Mode Control is to:

-Design a surface S(x) = 0 such that all system trajectories follow a desired behavior of tracking, regulation, and stability.

-Determine a control law capable of driving all state trajectories toward the sliding surface S(x) = 0 and keeping them on this surface.

4.4 Sliding mode control of the PMSM

Permanent magnet synchronous motors (PMSMs) are increasingly attracting attention in electric drive applications due to their high power density, high torque-to-inertia ratio, and higher efficiency compared to other types of motors. In an electric vehicle drive system, the motor speed must closely follow a specified reference trajectory, regardless of load disturbances, parameter variations, and model uncertainties. Moreover, a wide speed range covering both the constant torque and constant power regions is desirable. In electric vehicles, there are unavoidable interferences such as current coupling, friction force, parameter variations, and load disturbances during operation. Due to the presence of these interferences, accurately describing a mathematical model of the PMSM is challenging, and rapidly mitigating these disturbances with a linear control method is difficult. Substantial research has been reported detailing control and performance challenges. The classical proportional-integral (PI) controller, due to its implementation simplicity, remains the dominant choice in most applications. However, due to load disturbances, un modeled state variations, parameter changes, and friction forces, PI controllers are unable to provide effective solutions to many practical problems [99].

Variable structure sliding mode control is a type of nonlinear control method that can automatically adjust based on the system's current state. It does not require a precise mathematical model and can force the system to follow a predefined trajectory in sliding mode. The sliding mode trajectory can be artificially defined in advance and remains unaffected by the system's parameters and disturbances [100]. This control approach involves defining a so-called sliding surface and a Sliding Mode Control (SMC) law to guide and constrain the system to remain in the vicinity of this so-called 'switching' surface. SMC falls within the framework of variable structure system theory, which

aims to achieve a closed-loop dynamic that is largely independent of the process itself and, most importantly, of any potential parameter variations.

4.4.1Variable Structure Systems

A Variable Structure System (VSS) is a system whose structure changes during operation. It is characterized by the selection of a function and a switching logic. In variable structure systems with sliding mode, the state trajectory is brought to a surface (hyperplane) and, using the switching law, is forced to remain in the vicinity of this surface.

In general, the system dynamics can follow multiple surfaces. The trajectory in the phase plane consists of three distinct parts Figure 4.1 [101].

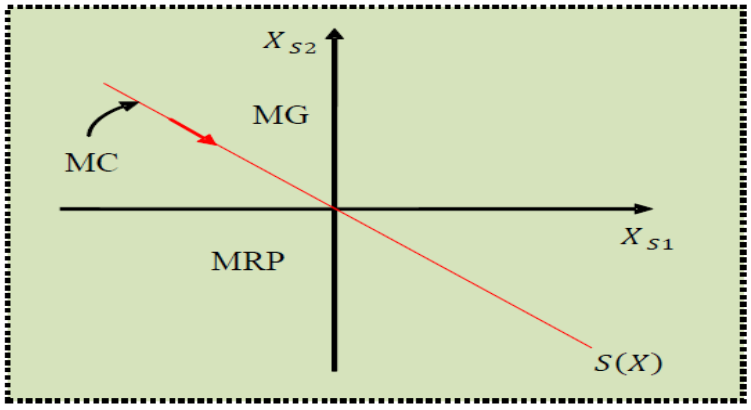

Figure 4.1. Different modes for the trajectory in the phase plane.

-The Convergence Mode (MC): in which the regular variable moves from the initial equilibrium point.

-The Sliding Mode (MG): during which the state variable has reached the sliding surface.

-The Permanent Regime Mode (MRP): The system's behavior is around the equilibrium point.

Variable structure systems are characterized by the selection of a function and a switching logic.

Consider the system described by the following differential equation:

$$\dot{x}(t) = f(x, t, u) \tag{4.1}$$

Where: $x = [x_1, x_2, \ldots . x_n] \in R^n$ is the state vector; $u \in R^n$ is the control input; t is time; and f is the function describing the system's evolution over time.

The sliding surface associated with the variable structure system is defined by:

$$S = \{x \in R^n : S(x) = 0\} \tag{4.2}$$

To keep the representative state of the system's evolution on a manifold, the control vector u is defined to switch between two values (u^+, u^-) depending on the sign of the switching surface S(x)

$$u(x,t) = \begin{cases} u^+(x,t) & si\ S(x) > 0 \\ u^-(x,t) & si\ S(x) < 0 \end{cases} \tag{4.3}$$

$u^+(x,t)$, $u^-(x,t)$ are continuous functions.

$S = \{x \in R^n : S(x) = 0\}$ is a sliding surface manifold that divides the state space into two regions: $S(x) < 0$ and $S(x) > 0$

This switching logic aims to constrain the trajectory to follow the switching surface. It is then said that the system's trajectory slides along the switching surface S(x)=0, a phenomenon known as sliding motion [102]. The trajectory in the phase plane consists of two parts Figure 4.2

- The Reaching Mode.
- The Sliding Mode

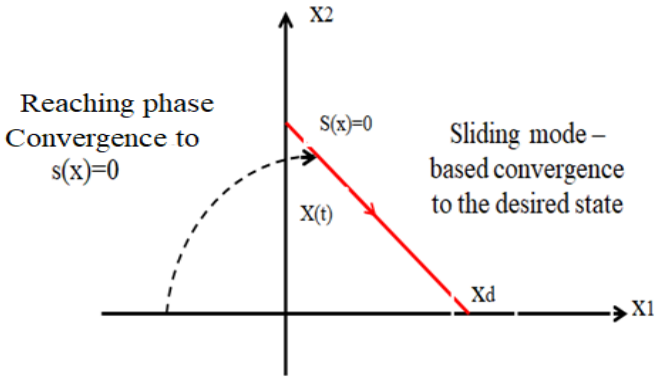

Figure 4.2. State trajectory in the phase plane.

In the first phase, the system state, starting from an arbitrary initial condition $x_1(0)=0$, tends toward the switching surface S(x)=0.

The second phase is characterized by the sliding mode, during which the state variable evolves on the sliding surface and converges toward the desired state $x_d(t)$

The variable system (4.1) with the control law (4.3) can be rewritten as follows:

$$\dot{x}(t) = f(x,t,u) = \begin{cases} f^+(x,t) & si\ \ S(x,t) > 0 \\ f^-(x,t) & si\ \ S(x,t) < 0 \end{cases} \quad (4.4)$$

S(x, t) is a surface in R^n that divides the space into two disjoint regions: $S(x,t) > 0$ and $S(x,t) < 0$.

Outside the discontinuity surface, the functions f^+ and f^- can exhibit different behaviors:

-The functions f^+ and f^- cross the surface from one side to the other.

- The functions f^+ and f^- are each attracted toward the surface.

The case of interest is when both functions f^+ and f^- are directed toward the surface; in this case, the surface is said to be attractive.

In a two-dimensional space, the principle of control discontinuity Equations (4.3) and (4.4) can be illustrated by Figure 4.3.

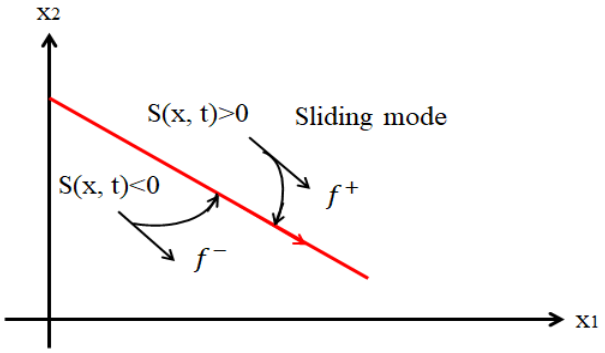

Figure 4.3. Convergence of the state trajectory to the switching surface prior to sliding mode.

Thus, the problem of the existence of the sliding regime comes down to analyzing the system's trajectory, which must not deviate from the surface S. We aim to verify that the distance and the derivative of the distance between the trajectory and the switching surface have opposite signs. This can be demonstrated by the following equation:

$$\begin{cases} \lim\limits_{s\to 0^-} & \dot{S} > 0 \\ \lim\limits_{s\to 0^+} & \dot{S} < 0 \end{cases} \quad (4.5)$$

Hence, the attractiveness condition for achieving the sliding regime:

$$s(x).\dot{s}(x) < 0 \quad (4.6)$$

This is the principle of attractiveness. Additional mathematical justifications can be found in books dealing with nonlinear systems.

4.4.2 Design of sliding mode control

The design of sliding mode control mainly consists of determining three steps [103]

1. The selection of the surface.
2. The establishment of the existence conditions for convergence.
3. The determination of the control law.

4.4.2.1 Selection of the sliding surface

The selection of the sliding surface concerns the required number of these surfaces and their shape, depending on the application and the intended objective. In general, for a system defined by the following state equation [101]:

$$\dot{x}(t) = f(x,t) + g(x,t)u(t) \quad (4.7)$$

It is necessary to choose "m" sliding surfaces for a vector y of dimension "m". Regarding the shape of the surface, two possibilities arise: either in the phase plane or in the state space. In the latter case, there is the so-called "switching law method by state feedback", this method uses the concepts of state feedback control to synthesize the switching law. Its major drawback lies in its slow transient response and highly complex design.

In the case of processing in the phase space, the switching function is a scalar function, such that the variable to be controlled slides on this surface to reach the origin of the phase plane.

Thus, the surface S(x) represents the desired dynamic behavior of the system. J.J. Slotine proposes a general equation to determine the sliding surface that ensures the convergence of a variable to its desired value. This equation is given in the following form [101]:

$$s(x) = \left(\frac{\partial}{\partial t} + \lambda_x\right)^{r-1} e(x) \quad (4.8)$$

$e(x)$: The deviation of the variable to be controlled, $e(x) = x_{ref} - x$

λ_x: A positive constant that represents the bandwidth of the desired control.

r: Relative degree, equal to the number of times the output must be differentiated to make the control appear.

For:

$r = 1 \Rightarrow s(x) = e(x)$

$r = 2 \Rightarrow s(x) = \lambda_x e(x) + \dot{e}(x)$

$r = 3 \Rightarrow s(x) = \lambda_x^2 e(x) + 2\lambda_x \dot{e}(x) + \ddot{e}(x)$

$S(x) = 0$ is a linear differential equation whose unique solution is $e(x) = 0$

The difficulty of this control lies in a trajectory tracking problem, where the objective is to keep S(x) at zero. This is equivalent to an exact linearization of the error while satisfying the convergence condition. The purpose of the exact linearization of the error is to enforce the error dynamics (reference – output) to follow the dynamics of an autonomous linear system of order "r" [103]

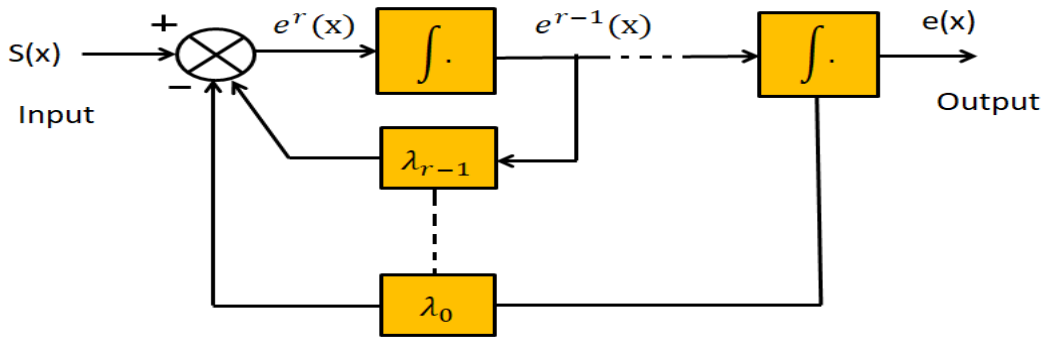

Figure 4.4. Exact linearization of the error.

4.4.2.2 Conditions for the existence of convergence

The convergence conditions ensure that the system dynamics converge towards the sliding surfaces. From the literature, we identify two conditions, which correspond to the convergence mode of the system state [101].

- **Direct switching function**

This is the first convergence condition, proposed by Emelyanov and Utkin. It is given in the following form:

$$s(x).\dot{s}(x) < 0 \qquad (4.9)$$

This means that the trajectory of the operating point, after reaching the sliding surface during a transient regime that satisfies condition (4.9), oscillates on either side of the surface with a high frequency and low amplitude, and quickly tends toward the desired operating point $e(x) = 0$ [101].

- **Lyapunov function**

The Lyapunov function is a positive scalar function $\mathrm{V(x)} > 0$ for the state variables of the system. It is used to assess control performance, study robustness, and ensure the stability of nonlinear systems.

By defining the Lyapunov function as:

$$\mathrm{V(x)} = \frac{1}{2}S^2(x) \tag{4.10}$$

For the Lyapunov function to decrease, it is sufficient to ensure that its derivative is negative. This is verified by the following relation:

$$\dot{\mathrm{V}}(\mathrm{x}) < 0 \Rightarrow \mathrm{s(x)}.\dot{\mathrm{s}}(\mathrm{x}) < 0 \tag{4.11}$$

This can be expressed by the following relations:

$$\lim_{s\to 0^-} \quad \dot{S} > 0 \quad and \quad \lim_{s\to 0^+} \quad \dot{S} < 0 \tag{4.12}$$

Equation (4.10) explains that the square of the distance to the surface, measured by $S^2(x)$, decreases continuously, forcing the system trajectory to move toward the surface from both sides. This condition assumes an ideal sliding regime where the switching frequency is infinite.

4.4.3 Determination of the control law

One of the essential assumptions in the design of variable structure systems controlled by sliding modes is that the control must switch instantaneously (infinite frequency) between u_{max} and u_{min}, depending on the sign of the sliding surface. In this case, very high-frequency oscillations appear in the sliding mode.

In sliding mode, the goal is to force the system dynamics to match the sliding surface $\mathrm{s(x)}$ using a control law defined by the following equation:

$$\mathrm{u(t)} = \mathrm{u_{eq}(t)} + \mathrm{u_N} \tag{4.13}$$

With:

u: control input.

u_{eq}: corresponds to the equivalent component.

u_N: Corresponds to the nonlinear component (discontinuous control input).

When the switching surface is reached, we can write:

$$u = u_{eq} \text{ and } u_N = 0 \quad (4.14)$$

The control u_{eq} can be interpreted as the average value that the control u takes during rapid switching between u_{max} and u_{min}.

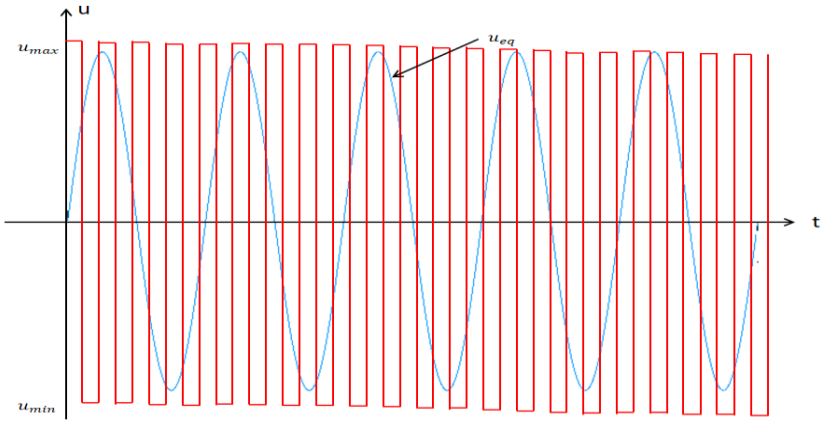

Figure 4.5. The equivalent continuous control u_{eq} applied during the switching between u_{max} and u_{min}.

The control vector u thus allows adjusting the dynamics of the two operating modes: u_{eq}: Enables influence over the sliding mode. It is computed based on the fact that the system's behavior during the sliding mode is described by $\dot{S}(x) = 0$, meaning in the case of a system without uncertainties.

It is obtained using the invariance conditions of the surface $\dot{S}(x,t) = 0$ and $S(x,t) = 0$

u_N: Enables influence over the reaching mode. It is determined to ensure the attraction of the controlled variable toward the sliding surface and to satisfy the convergence condition. It guarantees the system's insensitivity to parameter variations.

We are interested in computing the equivalent control and subsequently the attractive control of the system defined in the state space by equation (4.7).

$$\dot{x}(t) = f(x,t) + g(x,t)u(t) \tag{4.15}$$

The vector u is composed of two components:

$$u(t) = u_{eq}(t) + u_N \tag{4.16}$$

$$\dot{S}(x,t) = \frac{dS}{dt} = \frac{\partial S}{\partial x}.\frac{\partial x}{\partial t} = \frac{\partial S}{\partial x}\dot{x} \tag{4.17}$$

$$= \frac{\partial S}{\partial x}\left[f(x,t) + g(x,t)u_{eq}\right] + \frac{\partial S}{\partial x}\left[g(x,t)u_N\right]$$

In sliding mode, the trajectory will remain on the switching surface $S(x) = 0$, meaning its derivative will be zero $\dot{S}(x) = 0$ and $u_N = 0$ as given by equation (4.14).

$$u_{eq} = -\left[\frac{\partial S}{\partial x}f(x,t)\right].\left[\frac{\partial S}{\partial x}g(x,t)\right]^{-1} \quad , u_N = 0 \tag{4.18}$$

During the convergence mode, by replacing the term u_{eq} with its value from equation (4.18) in equation (4.17).

Let us define: $L = \frac{\partial S}{\partial x}$ Hence: $u_{eq} = -[Lf][Lg]^{-1}$ Thus, we obtain a new expression for the derivative of the surface:

$$\dot{S}(x) = \frac{\partial S}{\partial x}.[g(x,t)u_N] \tag{4.19}$$

The problem reduces to finding u_N such that:

$$S(x)\dot{S}(x) = \dot{S}(x) = \frac{\partial S}{\partial x}.[g(x,t)u_N] < 0 \tag{4.20}$$

The simplest solution is to choose u_N in the form of a relay, as shown in Figure 4.6. In this case, the control is written as follows:

$$u_N = K.\,sign(S(x)) \tag{4.21}$$

By substituting expression (4.20) into (4.19), we obtain:

$$S(x)\dot{S}(x) = |S(x)|\frac{\partial S}{\partial x}.Kg(x,t) < 0 \tag{4.22}$$

The factor $\frac{\partial S}{\partial x}.g(x,t)$ is always negative for the class of systems we consider.

The gain K is chosen to be positive to satisfy condition (4.22). The choice of this gain is very influential because if it is too small, the response time will be very long, and if it is

too large, we will have a very short response time with strong oscillations in the control system. These very high-frequency oscillations, known as “Chattering”, can excite neglected dynamics or even degrade the control system or damage the actuators.

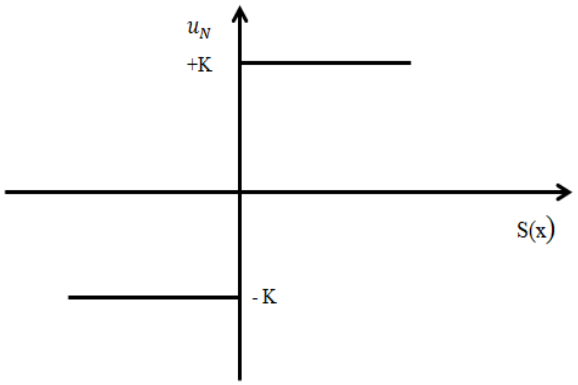

Figure 4.6. Definition of the control law.

4.4.4 Advantages and disadvantages of sliding mode control

There are many advantages to sliding mode control: precision, simplicity, fast response time, and robustness. This makes it particularly suitable for handling systems with poorly known models, either due to parameter identification issues or due to model simplifications.

An ideal sliding regime requires a control that can switch at an infinite frequency. Obviously, for practical applications, only switching at a finite frequency is possible. Thus, during the sliding regime, the discontinuities applied to the control can lead to a phenomenon known as chattering. This phenomenon is characterized by strong oscillations of the system's trajectories around the sliding surface. The main cause of this phenomenon is the discontinuous nature of the control, which corresponds to the discontinuous component of the form $K.\mathrm{sign}(S(x))$ causing the operating point to oscillate around the sliding surface at a high frequency.

The chattering phenomenon is considered a real obstacle to the application of sliding mode control. To address this issue, several solutions have been proposed.

4.5 Sliding mode control tuning strategy for the PMSM

After presenting the theory of sliding mode control, we will analyze in this section the behavior of the traction system controlled by sliding mode.

The model of the permanent magnet synchronous machine is recalled as follows:

$$\dot{i}_d = -\frac{R}{L_d} i_d + \frac{L_q}{L_d} P\omega_r i_q + \frac{1}{L_d} u_d \qquad (a)$$

$$\dot{i}_q = -\frac{R}{L_q} i_q + \frac{L_d}{L_q} P\omega_r i_d - \frac{\varphi_f}{L_q} P\omega_r + \frac{1}{L_d} u_q \qquad (b) \qquad (4.23)$$

$$\dot{w} = \frac{3P}{2j}\left(\varphi_f i_q + (L_d - L_q) i_d i_q\right) - \frac{1}{j} C_r - \frac{f}{j} w_r \qquad (c)$$

With:

R: Stator resistance, L_d , L_q: d *and* q inductances of the stator along the axes, φ_f : Flux linkage of the permanent magnet, i_d, i_q: Currents in the stator, u_d, u_q: Voltages of the stator ω_r: Mechanical speed, j:Inertial moment, f: Viscous friction coefficient, P: Pole pair count, C_r:Torque due to the load.

4.5.1 Three-surface adjustment strategy

Figure 4.7 shows the diagram of sliding mode tuning by applying the cascade tuning method principle. The system consists of a speed regulation loop that produces the current reference i_{qref} which in turn determines the control u_{qref}, the control u_{dref} is determined by the current regulation i_{dref}.

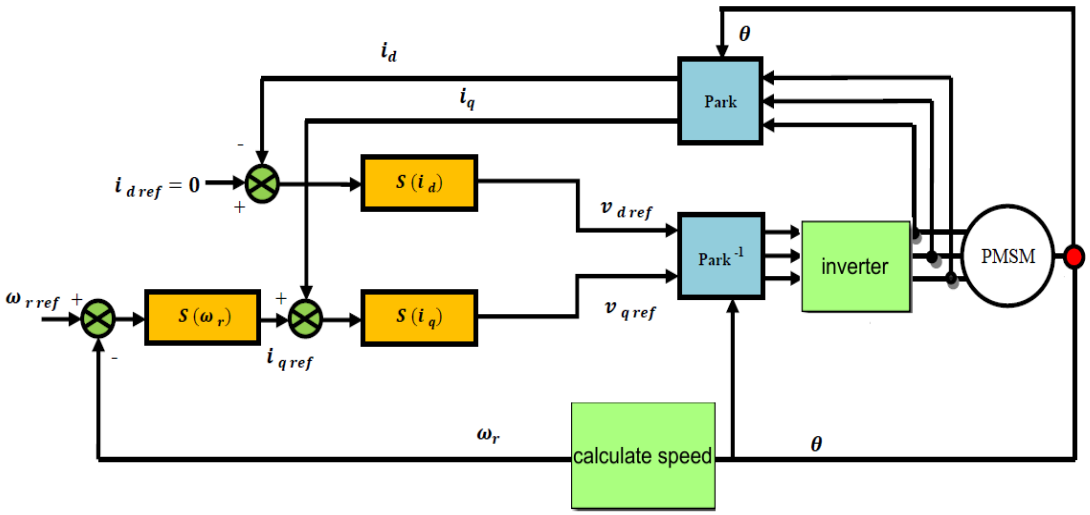

Figure 4.7 General schematic of the SMC strategy using three surfaces.

i_d Current Adjustment

The expression for current i_d is expressed by Equation 4.23(a): It can be observed from Equation 4.23(a) that the relative level of the current i_d with respect to the control v_d is equal to one. Therefore, the error variable e_d is given by:

$$e_d = i_{dref} - i_d \tag{4.24}$$

The resulting error will be adjusted by a regulator functioning in sliding plane, with the control surface described as:

$$s(i_d) = i_{dref} - i_d \tag{4.25}$$

Thus, the derivative of the surface is:

$$\dot{s}(i_d) = \dot{i}_{dref} - \dot{i}_d \tag{4.26}$$

Taking into account the current equation i_d derived in the system of equations Equation 4.23(a), the surface's derivative becomes:

$$\dot{s}(i_d) = \dot{i}_{dref} + \frac{R}{L_d} i_d - \frac{L_q}{L_d} P w_r i_q - \frac{1}{L_d} u_d \tag{4.27}$$

In sliding mode, we have: $\dot{s}(i_d) = 0$, $u_{dN} = 0$

$$v_{deq} = (\dot{i}_{dref} + \frac{R}{L_d} i_d - \frac{L_q}{L_d} P w_r i_q) L_d \tag{4.28}$$

$$u_{dN} = K_d . \text{sign}(s(i_d)) \tag{4.29}$$

Where: K_d represents the positive amplification factor of the direct current regulator.

i_q Current Adjustment

The expression for current i_q is given by Equation 4.23(b): The output value i_{qref} from the speed controller is assessed against the observed value. The error that results will be corrected by a regulator functioning in sliding mode. Subsequently, using the same method as previously, we are able to determine u_{qref} and u_{qN} the control surface is described by the equation below:

$$s(i_q) = i_{qref} - i_q \tag{4.30}$$

The derivative can be written as:

$$\dot{s}(i_q) = \dot{i}_{qref} - \dot{i}_q \tag{4.31}$$

By substituting the value $\dot{i}_q$ from equation 4.23(b) into equation 4.32, we get:

$$\dot{s}(i_q) = \dot{i}_{qref} - (\frac{R}{L_q} i_q - \frac{L_d}{L_q} P w_r i_d - \frac{P\varphi_f}{L_q} w_r + \frac{1}{L_q} u_q) \tag{4.32}$$

While in the sliding mode, we have $\dot{s}(i_q) = 0$, $s(i_q) = 0$, $u_{qN} = 0$

$$u_{qeq} = (\dot{i}_{qref} + \frac{R}{L_q} i_q - \frac{L_d}{L_q} P w_r i_d + \frac{P\varphi_f}{L_q} w_r) L_q \tag{4.33}$$

$$u_{qN} = K_q . \text{sign}(s(i_q)) \tag{4.34}$$

With: K_q represents the positive amplification factor of the quadratic current regulator.

Speed Adjustment

From equation 4.23(c), it is observed that the relative order of the speed is unity. In this scenario, the sliding surface is defined by the tracking error.

$$s(w_r) = w_{rref} - w_r \tag{4.35}$$

Accordingly, the derivative of it

$$\dot{s}(w_r) = \dot{w}_{rref} - \dot{w}_r \tag{4.36}$$

Substituting equation 4.23(c) into equation 4.28, gives us:

$$\dot{s} = \dot{w}_{rref} - \frac{P(L_d - L_q) i_d + P\varphi_f}{j} i_q + \frac{1}{j} C_r + \frac{f}{j} w_r \tag{4.37}$$

In the sliding mode, we get $s(w_r) = 0$, $\dot{s}(w_r) = 0$, $i_{qN} = 0$

$$\dot{i}_{qeq} = \frac{\dot{w}_{rref} + \frac{f}{j} w_r + \frac{1}{j} C_r}{\frac{P(L_d - L_q)}{j} i_d + P\frac{\varphi_f}{j}} \tag{4.38}$$

$$i_{qN} = K_{w_r} . \text{sign}(s(w_r)) \tag{4.39}$$

With: K_{w_r} represents the positive amplification factor of the speed controller.

4.6 Fuzzy sliding mode control of PMSM

With the significant advancements in electric machine control, new techniques and approaches have been developed. Among them, fuzzy sliding mode control stands out as a widely used robust control method. By integrating fuzzy logic with sliding mode control, this approach harnesses the strengths of both techniques. It effectively addresses the limitations of traditional tuning algorithms while improving the system's performance in terms of stability, precision, speed, and robustness. In this section, we detail the principle of fuzzy control (FLC) to address this drawback. What we aim to demonstrate is that fuzzy sliding mode control (FSMC) can effectively mitigate the chattering phenomenon.

4.6.1 Description of Fuzzy Logic

Fuzzy logic emerged as an alternative to strict logic, mimicking the empirical behavior of the human brain. Its formal introduction was pioneered by the renowned researcher L. Zadeh, who contributed to the modeling of physical phenomena using fuzzy formalism based on the fuzzy set theory developed in 1965 [104]. Later, M. Mamdani experimented with it in 1974 by applying it to industrial process control, specifically in the regulation of a steam engine [105].

Without delving too deeply into the mathematical formalism of fuzzy logic, we will briefly present general definitions of this method and its key properties.

4.6.1.1 Fuzzy Sets and Membership Function

Fuzzy set theory [104] allows expressing the concept of partial membership of an element in a set, or more precisely, its degree of membership. In classical set theory, an element either belongs to a set or does not. However, in reality, it is rare to encounter situations where things are distinctly defined.

A fuzzy set A is defined by a membership function $\mu_A(x)$ that takes values in the range [0, 1] and quantifies the degree to which an element x of X belongs to A.

$$A = \{(x, \mu_A(x) \in X)\} \tag{4.40}$$

Multiple fuzzy sets (sometimes called subsets) can be defined on the same variable, each with its own membership function. The set is called the "Universe of Discourse X".

4.6.1.2 Representations of membership functions

Various nonlinear shapes can represent membership functions. The trapezoidal, triangular in Figure 4.8, and bell-shaped forms are the most commonly used [106].

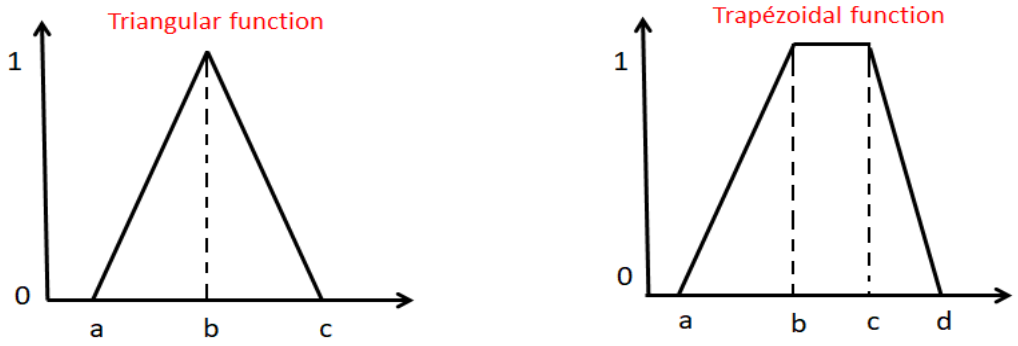

Figure 4.8. Types of membership functions.

4.6.1.3 Structure of a fuzzy controller

The basic structure of a fuzzy controller consists of three main parts, as shown in Figure 4.9 [107].

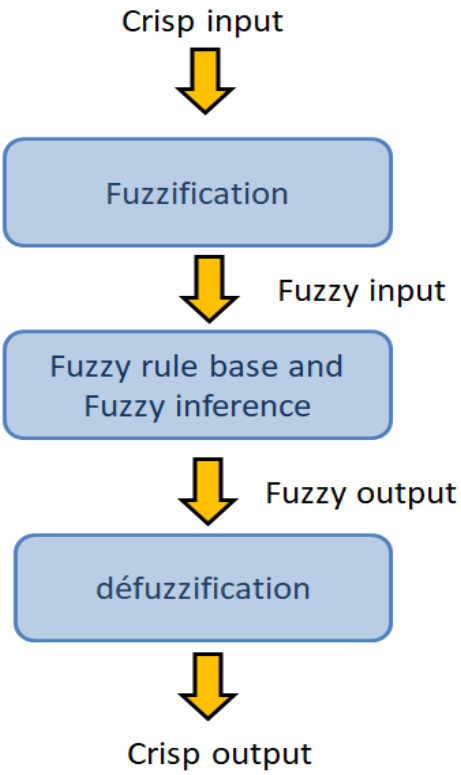

Figure 4.9. The structure of fuzzy logic controller.

- **Fuzzification**

Fuzzification involves defining membership functions for the different input physical variables. It consists of assigning the input variable (which is a strict 'crisp' variable in English) degrees of membership to its fuzzy sets. The number of fuzzy sets, the shape of the membership functions, and their distribution over the universe of discourse are determined by the expert operator.

- **Rule Base**

The expert's knowledge of a given process is transformed into a set of linguistic rules in the following form:

If premise Then conclusion

The rules can be represented in a matrix known as the inference matrix. The premise consists of a set of conditions connected by fuzzy operators applied to membership functions. The most commonly used operators are the intersection operator 'AND,' the union operator 'OR,' and the negation or complement operator 'NOT'.

For example, considering two fuzzy sets A and B, with their respective membership functions $\mu_A(x)$ and $\mu_B(x)$, belonging to a universe of discourse X, the aforementioned operators are defined as follows [107]:

- **OR operator**

It corresponds to the union (C) of two fuzzy sets (A, B), mathematically expressed as:

$$C = A \cup B \tag{4.41}$$

In fuzzy logic, the union is generally achieved by formulating the maximum of the membership functions as follows:

$$\mu_C(x) = \max(\mu_A(x), \mu_B(x)) \tag{4.42}$$

- **AND operator**

The intersection (C = A) is often achieved using the following minimum formulation:

$$\mu_C(x) = \min(\mu_A(x), \mu_B(x)) \tag{4.43}$$

- **NOT operator**

The complement of a fuzzy set A is defined by the membership function as follows $\mu_{\bar{A}}(x)$:

$$\mu_{\bar{A}}(x) = 1 - \mu_A(x) \tag{4.44}$$

- **Inference mechanism**

Now, it is necessary to define the membership degrees of the output variable to its fuzzy sets. This is referred to as the inference mechanism or fuzzy implication methods. For systems regulated by fuzzy logic, one of the following methods is generally used:
-Max-min inference method, also known as the Mamdani method.
-Max-prod inference method, also known as the Larsen method.
-Sum-prod inference method.
-Sugeno inference method.
Due to its simplicity, the Mamdani method is the most widely used [108]. It implements the 'AND' operator using the 'min' function, the 'THEN' conclusion of each rule using the 'min' function, and the connection between all rules (the 'OR' operator) using the 'max' function.

$$\mu_A(x) = \min(\mu_A(x), \mu_B(x)) \tag{4.45}$$

Finally, the aggregation of rules is the last step of inference. It allows synthesizing the obtained results by considering the influence of all the values proposed by the fuzzy decision.

- **Defuzzification**

The result obtained from inference using one of the implication methods is formally a fuzzy value. This value cannot be directly used to control the process. Therefore, a transformation must be applied at the output of the inference mechanism to convert it into a precise quantity. This action is referred to as defuzzification. In the literature, several solutions exist to perform this operation, including the maximum value method, the mean of maxima, the center of gravity (centroid), and weighted heights.
The defuzzification method using the center of gravity is by far the most widely used method in fuzzy control [107, 108]. In the literature, several strategies exist to perform this operation, such as the mean of maxima, the center of areas, and the center of

maxima. The center of gravity defuzzification method is the most commonly used in fuzzy control because it intuitively provides the most representative value of the fuzzy set resulting from rule aggregation. This method involves calculating the center of gravity of the surface formed by the resulting membership function.

The maximum technique: This is the simplest method, which consists of considering only the rule with the highest validity for each output. This technique is rarely used because it presents disadvantages when multiple values make the resulting membership function reach its maximum.

The weighted average technique: The defuzzifier examines the fuzzy set that determines the values for which the membership function is maximal, then calculates the average of these values as the defuzzification result.

The center of gravity technique: This method is more effective and provides the best results. It consists of determining the center of gravity of the output membership function using the following equation:

$$\overline{X} = \frac{\int_{-1}^{1} x\mu_B(x)dx}{\int_{-1}^{1} \mu_B(x)dx} \tag{4.46}$$

The integral in the denominator gives the surface area, while the integral in the numerator corresponds to the moment of the surface.

4.6.1.4 Different approaches for rule determination

There are two main approaches for determining the rules of a fuzzy controller. The first is a purely heuristic method, where the rules are designed to correct the deviation between the setpoint and the output. This approach relies on qualitative knowledge of the process behavior [109]. The second approach is a systematic method that determines the linguistic structure and/or parameters that meet the control objectives and constraints.

Another method was introduced [110] for rule determination by referring to the trajectory of the closed-loop system. The intuitive search for the closed-loop system behavior, for rule determination in the time domain, frequently uses the error e (observation), the error variation Δe (process dynamics), and the control variation ΔU (input of the process to be regulated)

The procedure to follow for determining the rules of the fuzzy controller is explained by considering the points indicated in Figure 4.10. For each of these points, the expertise is expressed as follows:

Rule 1: If $e = PG$ and $\Delta e = EZ$, then $\Delta U = PG$. Start.

Rule 2: If $e = PG$ and $\Delta e = NP$, then $\Delta U = PM$. Increase the order to maintain balance.

Rule 3: If $e = PM$ and $\Delta e = NP$, then $\Delta U = PP$. Very slight increase in the order to avoid exceeding the limit value.

Rule 4: If $e = PP$ and $\Delta e = NP$, then $\Delta U = EZ$. Convergence towards equilibrium.

Rule 5: If $e = EZ$ and $\Delta e = NP$, then $\Delta U = NP$. Process deceleration.

Rule 6: If $e = NP$ and $\Delta e = PP$, then $\Delta U = NM$. Deceleration and reversal of the command variation.

Rule 7: If $e = NM$ and $\Delta e = EZ$, then $\Delta U = NM$ Process recall towards equilibrium.

Rule 8: If $e = NP$ and $\Delta e = EZ$, then $\Delta U = EZ$. Convergence towards equilibrium.

Rule 9: If $e = EZ$ and $\Delta e = EZ$, then $\Delta U = EZ$. Equilibrium.

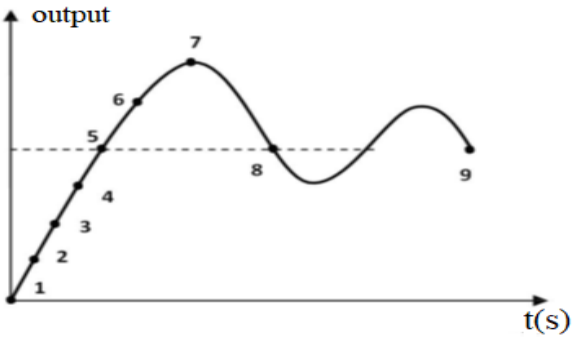

Figure 4.10. Formulation of the rule set using temporal analysis.

4.7 Hybrid tuning strategy by fuzzy sliding mode control (HFSMC) of the machine

The main drawback of sliding mode controllers is the chattering induced by their discontinuous control signals. To overcome this limitation, Sliding Mode Control (SMC) is integrated with Fuzzy Logic Control (FLC) to enhance robustness and improve the dynamic response of nonlinear systems [111]. The resulting hybrid approach, termed fuzzy sliding mode control, effectively suppresses chattering while ensuring precise tracking of the PMSM reference speed. In the fuzzy sliding mode control, it is sufficient to replace the k.sign(S(x)) function with a fuzzy controller.

In this section, a fuzzy controller (FLC) is introduced to replace the $K_{w_r}.\text{sign}(s(w_r))$ function, so that the state trajectory can reach and move along the switching surface. A good steady-state dynamic performance can be achieved through the combination of SMC and FLC. Fuzzy-PI controllers have two inputs and one output. The fuzzy PI controller is developed using membership functions for the inputs error "e" and error change "de" as well as the output membership function for w_r, the measured speed of the PMSM.

$$e = w_{rref} - w_r \tag{4.47}$$

$$de = e_k - e_{k-1} \tag{4.48}$$

with w_{rref} defined as the reference or the ideal output velocity, and w_r is the real speed of output. The basic schematic of the fuzzy sliding mode control of the PMSM is identical to that shown in Figure 4.7, by replacing the $K_{w_r}.\text{sign}(s(w_r))$ function with a fuzzy controller, as illustrated in Figure 4.11.

These numerical variables are transformed into language variables using the seven levels or fuzzy sets listed below:

NG: Negative Large, NM: Negative Medium, NP: Negative Small, ZE: Around Zero, PP: Positive Small, PM: Positive Medium, PG: Positive Large, as shown in Table 4.1. The chattering problem is one of SMC's well-known disadvantages.

To enable the state trajectory to reach and follow the changing surface, a Fuzzy Logic Control (FLC) is added in this section in place of the speed surface. Combining SMC and FLC can result in a favorable dynamic equilibrium state [112]. Through simulation results, the benefits of the suggested fuzzy sliding mode control are confirmed.

Table 4.1: The rule base for controlling the speed.

de \ e	NB	NM	NS	ZE	PS	PM	PB
NB	NB	NB	NB	NB	NM	NS	ZE
NM	NB	NB	NB	NM	NS	ZE	PS
NS	NB	NB	NM	NS	ZE	PS	PM
ZE	NB	NM	NS	ZE	PS	PM	PB
PS	NM	NS	ZE	PS	PM	PB	PB
PM	NS	ZE	PS	PM	PB	PB	PB
PB	ZE	PS	PM	PB	PB	PB	PB

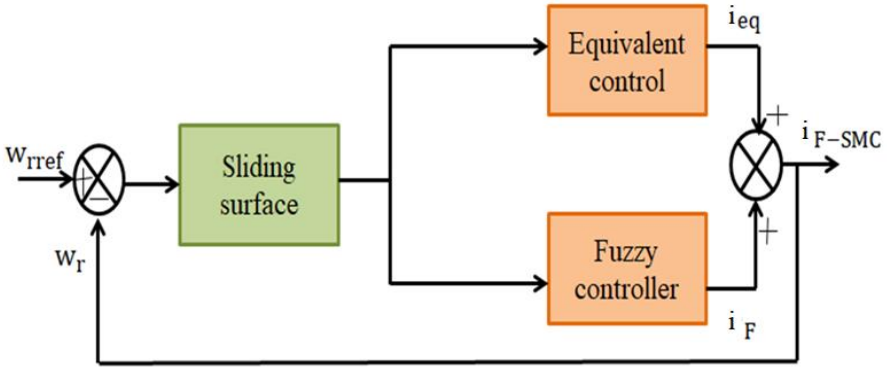

Figure 4.11. Block diagram of the speed control using a fuzzy sliding mode controller.

The same procedure used in designing the speed controller is applied to the current controller, with the only difference being that we have:

The input error e: rather than being equivalent to $e = w_{rref} - w_r$, it will be defined as $e = id_{s_{ref}} - id_s$ to the primary fuzzy regulator on the current id_s, similarly for the second fuzzy regulator of current iq_s, $e = iq_{s_{ref}} - iq_s$, The output of the fuzzy controller corresponds to vd_s for the id_s current regulator and $v\,q_s$, for the iq_s current regulator. This ensures that the inner loop operates faster than the outer one, satisfying the subordination condition. Table 4.2 displays the rule basis for the output variable, it comprises nine linguistic rules that define the variation of the fuzzy logic controller's output based on the two input variables e and de for each current controller (id_s and iq_s).

Additionally, three fuzzy sets are assigned to each membership function:
P: Positive, N: Negative and ZE: Zero.

Table 4.2: The rule base for controlling the currents.

de \ e	N	ZE	P
N	N	N	ZE
ZE	N	ZE	P
P	ZE	P	P

4.8 Presentation of the studied traction system

The traction system analyzed in this study corresponds to the one illustrated in Figure 4.12. The vehicle is assumed to be driven by a single permanent magnet synchronous motor (PMSM), powered by a 21-level multilevel voltage inverter. The parameters of both PMSM and the electric vehicle (EV) are provided in appendices A and B respectively.

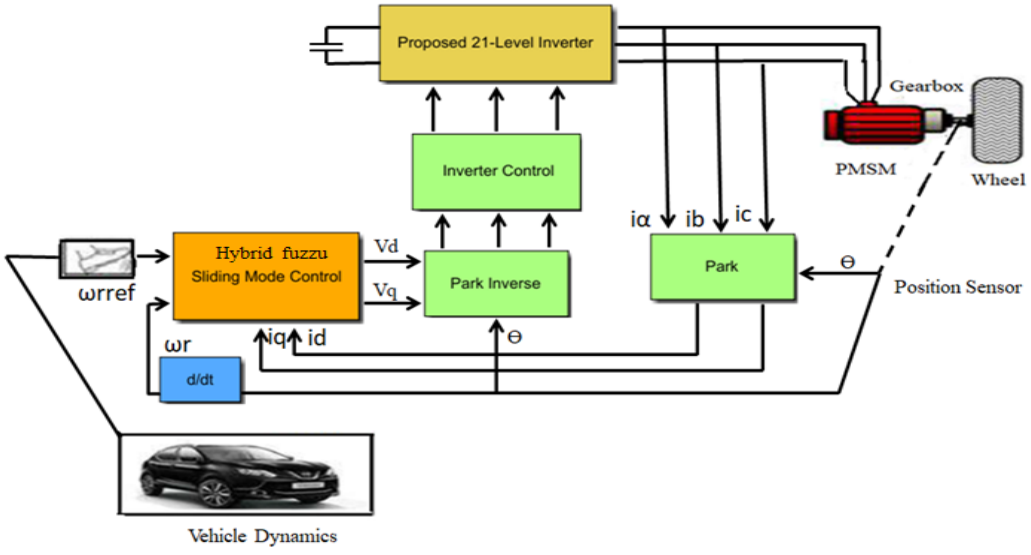

Figure 4.12. Description of the traction system block diagram.

4.9 Simulation results

The numerical simulations were carried out on an electric vehicle powered by a 50 kw permanent magnet synchronous motor (PMSM), supplied by a new 21-level voltage inverter topology. The inverter plays a key role in the system, as it optimizes the output voltage quality to supply the motor (by reducing the Total Harmonic Distortion, THD), while minimizing the number of control devices. This makes the system more cost-effective, simpler, and easier to maintain compared to conventional designs**.** The control strategies applied to the traction chain are of the following types: Sliding Mode Control and a hybrid approach combining Sliding Mode and Fuzzy Logic. The objective of the simulations performed is to evaluate the dynamic performance of the proposed control strategy under the standardized urban driving cycle ECE-15.

4.9.1 Reference tracking test

4.9.1.1 Performance validation by SMC

The following simulation results demonstrate the control of the vehicle's speed using a Sliding Mode Controller (SMC). It should be mentioned that the European Urban Driving Cycle ECE-15 was used to conduct the simulation. In the course of this cycle, three speed demands in a trapezoidal form were applied (36 Km/h, 76 Km/h, 120 Km/h). In addition, a 10% slope was introduced between 16 and 23 seconds. The objective of this simulation is to verify whether our control method can be implemented in real-time and to observe the vehicle's behavior through various studied modes. This helps improve the vehicle's energy performance.

The ability to perform robust speed transitions is a critical factor for drivers, as the vehicle's response in such scenarios is a key indicator of driving quality under real traffic conditions. Accordingly, speed change tests are essential for evaluating the performance of our electric vehicle, particularly in terms of energy management, overtaking capability, deceleration, and other dynamic responses. The simulation has been conducted using the Matlab-Simulink environment.

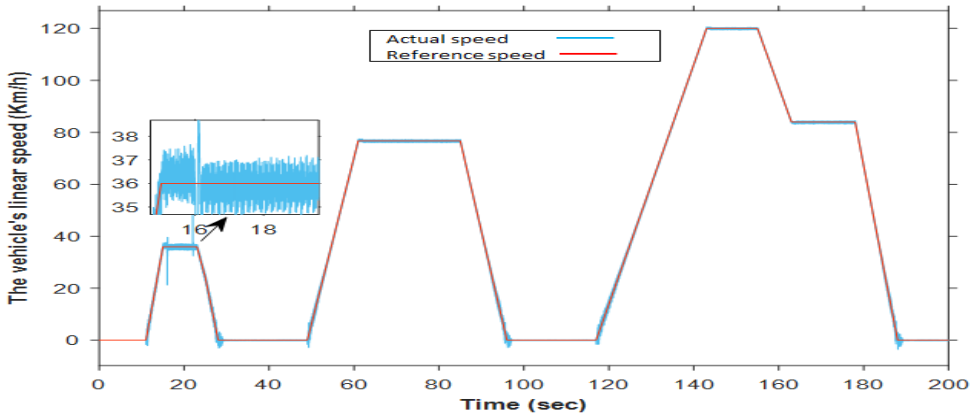

Figure 4.13. The vehicle's linear speed (SMC).

Figure 4.13 illustrates the vehicle speed response using the SMC technique. We observe that the vehicle's linear speed can rapidly track the reference speed, a good tracking dynamics are observed. This command switches very quickly within its limits which impacts the overall command of the vehicle

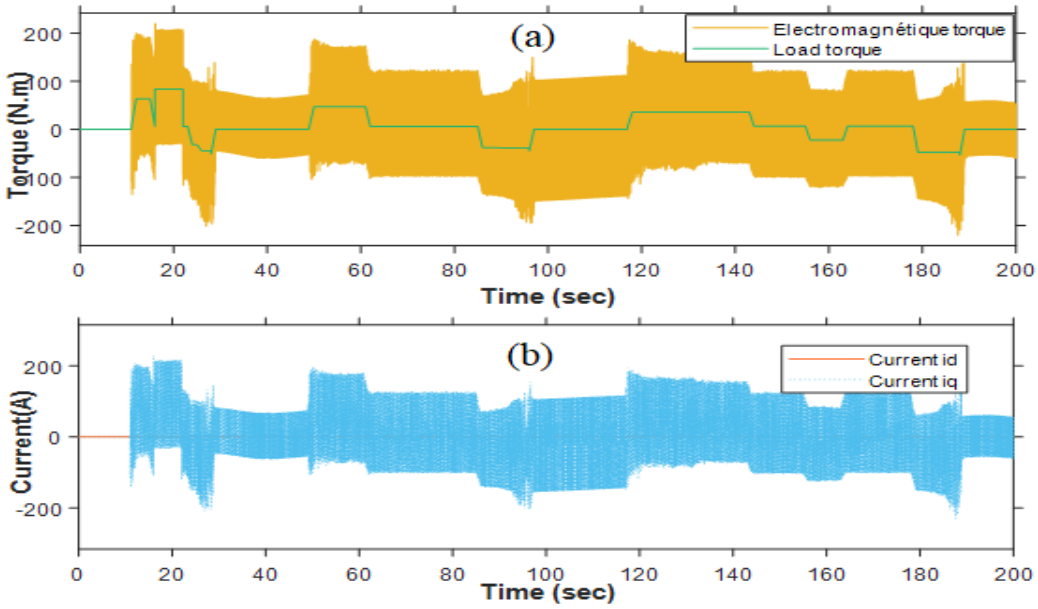

Figure 4.14. (a) Electromagnetic and load torque, (b) Quadratic and direct currents (SMC).

Figure 4.14(a) shows the variation of electromagnetic torque as load torque changes, Figure 4.14 (b) shows the results for the direct and quadrature currents. As mentioned in the description of the control strategy, it is clearly observed that this method maintains the direct current at zero and allows only the quadrature component to respond to the torque disturbance. This demonstrates the controller's good tracking

performance (i_{dref} = 0). The i_q current and the electromagnetic torque have the same profile, which indicates that decoupling has been perfectly achieved.

It can also be seen in Figure 4.14 that the electric motor generates more electromagnetic torque to reach the different stages of the speed reference, reaching 200 N·m between 16 and 23 seconds to overcome the inertia torque. The oscillations are even more noticeable in the torque response curve shown in Figure 4.14. This phenomenon affects the operation of the control system as well as the currents absorbed by the machine. From these curves, it is evident that the decoupling is seriously affected by the chattering phenomenon.

These simulation results demonstrate the advantages of sliding mode control, which reflects the robustness it offers against disturbances. However, it can be noted that the system's performance may be degraded due to a phenomenon known as chattering. This issue is the subject of intensive research efforts aimed at mitigation.

4.9.1.2 Performance validation by HFSMC

The robustness of the Hybrid Fuzzy Sliding Mode Control (HFSMC) with respect to variations in load and rotational speed is evaluated. The standard ECE-15 driving cycle, representing the driver's requested speed, was employed, covering a time interval of 0 < t < 200 s. Additionally, a 10% gradient was introduced between 16 and 23 seconds to simulate a more challenging driving condition**.**

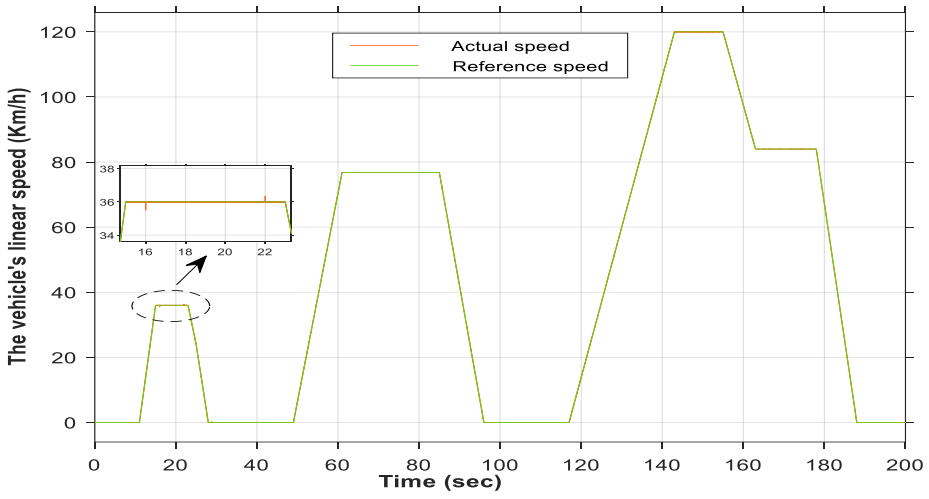

Figure 4.15. The vehicle's linear speed (HFSMC).

Figures 4.15 show that the implemented control strategy offers advantages compared to the strategy using only the sliding mode Figures 4.13, where a more robust

response to speed and load disturbances applied during the period 16 < t < 23s can be observed. Thus, there is a significant reduction in the chattering phenomenon. This confirms the advantage of the proposed control strategy in terms of robustness against load and rotational speed disturbances.

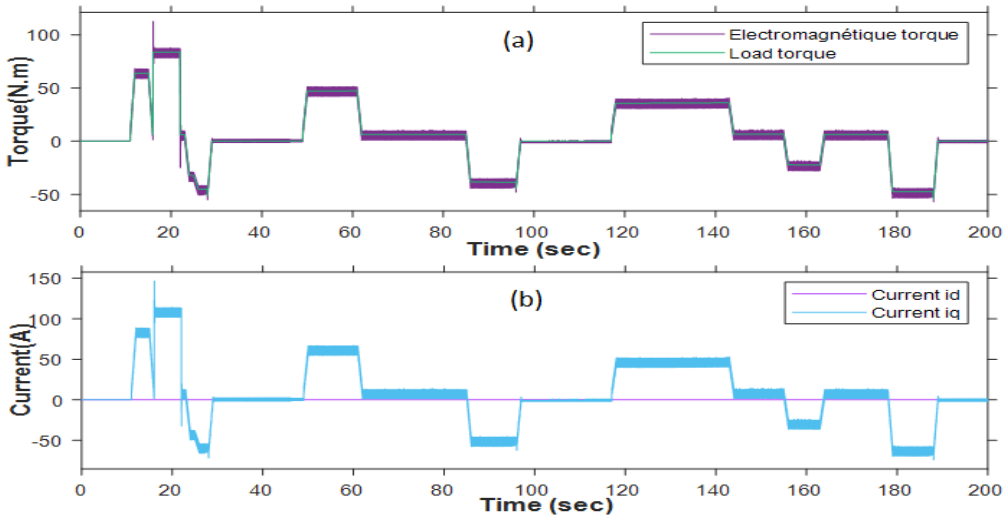

Figure 4.16. (a) Electromagnetic and load torque, (b) Quadratic and direct currents (HFSMC).

Figure 4.16 (b) illustrates the stator current profiles along the d and q axes. The two currents are independently regulated and exhibit distinct dynamic behaviors depending on the control strategy employed, both during transient and steady-state operation, with a particular emphasis on the i_q component. Regarding the sliding mode control strategy, the effect of the chattering phenomenon on the i_q current is clearly noticeable. In contrast, with the fuzzy sliding mode control strategy, a significant reduction of this phenomenon is observed. This improvement is due to the contribution of fuzzy logic, which effectively mitigates the undesirable chattering while maintaining strong robustness against disturbances.

Figure 4.16 (a) illustrates the behavior of the electromagnetic torque and the resistant torque. As the flux is kept constant, the electromagnetic torque remains steady and closely matches the profile of the i_q current.

In this section, we have studied a controller that can be applied to a wide class of nonlinear systems. It combines the advantages of two control techniques widely recognized for their robustness: fuzzy control whose undeniable performance has made it increasingly attractive to researchers and sliding mode control, which is well known

for its stability properties and robustness against external disturbances. The application of this hybrid control strategy to our traction system has yielded highly satisfactory results in terms of stabilization and trajectory tracking, while effectively overcoming the chattering issues typically associated with sliding mode control and the lack of analytical tools inherent to fuzzy logic control.

4.9.2 Evaluating robustness to parametric variations

4.9.2.1 Validation of robustness using SMC control

To highlight the importance of the sliding mode control technique, we will carry out robustness tests on our machine. To verify this robustness, we assume that the values of R and J are increased by up to 50%. The influence of the variations of these parameters on the vehicle speed and torque is illustrated in Figure 4.17 and Figure 4.18

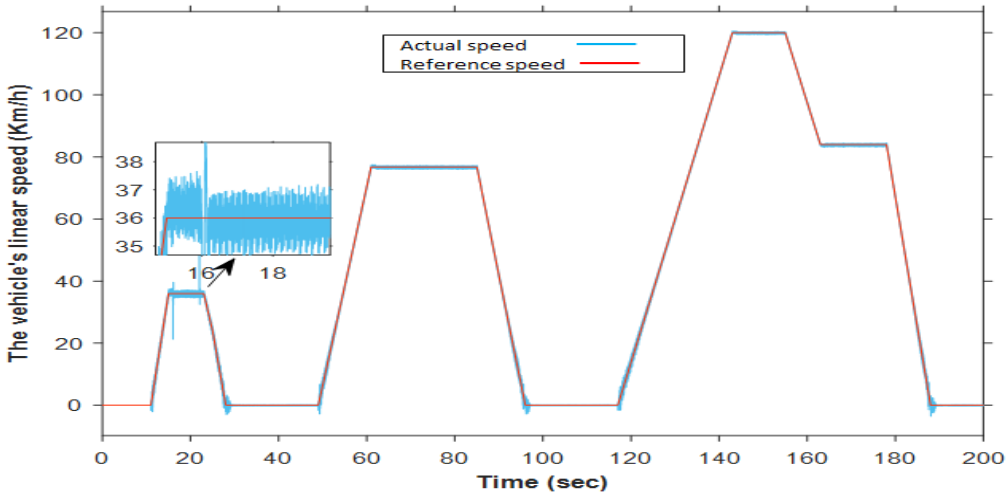

Figure 4.17. Simulation results of the vehicle speed with variations in inertia (j)

and resistance (R)- (SMC)

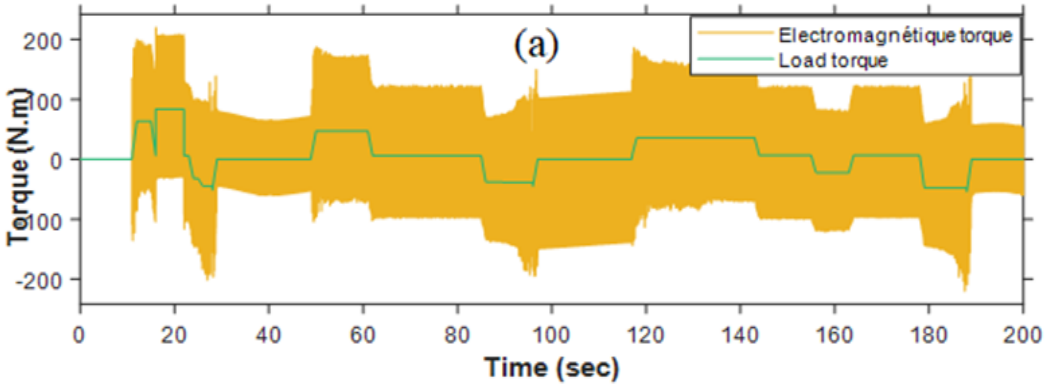

Figure 4.18. Simulation results of the torque with variations in inertia (j)

and resistance (R)- (SMC)

It is observed that the speed remains unaffected by variations and follows its setpoint with a very short response time and no overshoot. Which highlights the high robustness of the control against parametric variations.

4.9.2.2 Validation of robustness using HFSMC control

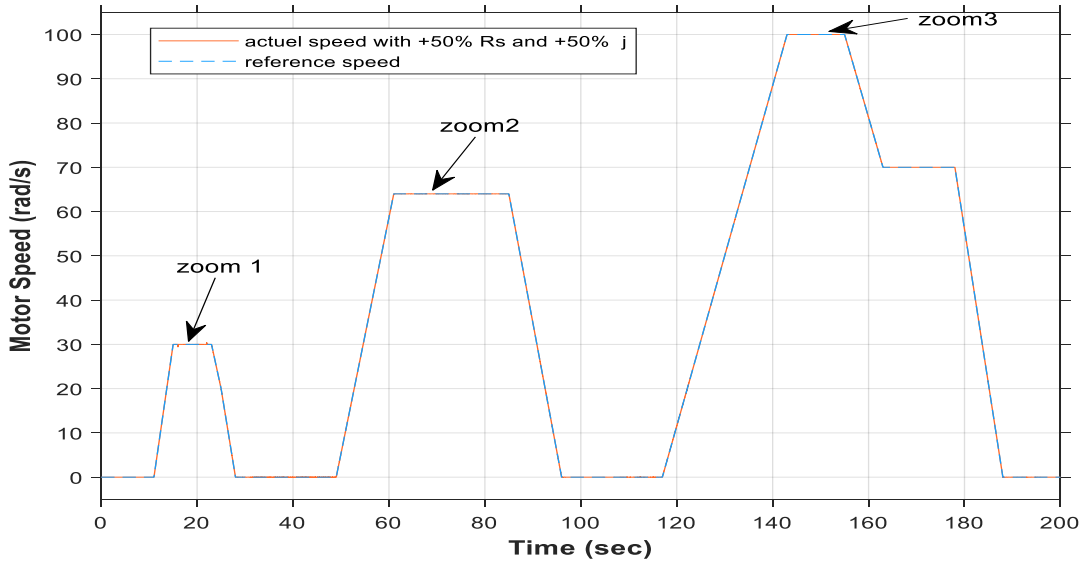

Figure 4.19. Simulation results of the vehicle speed with variations in inertia (j)

and resistance (R)- (HFSMC)

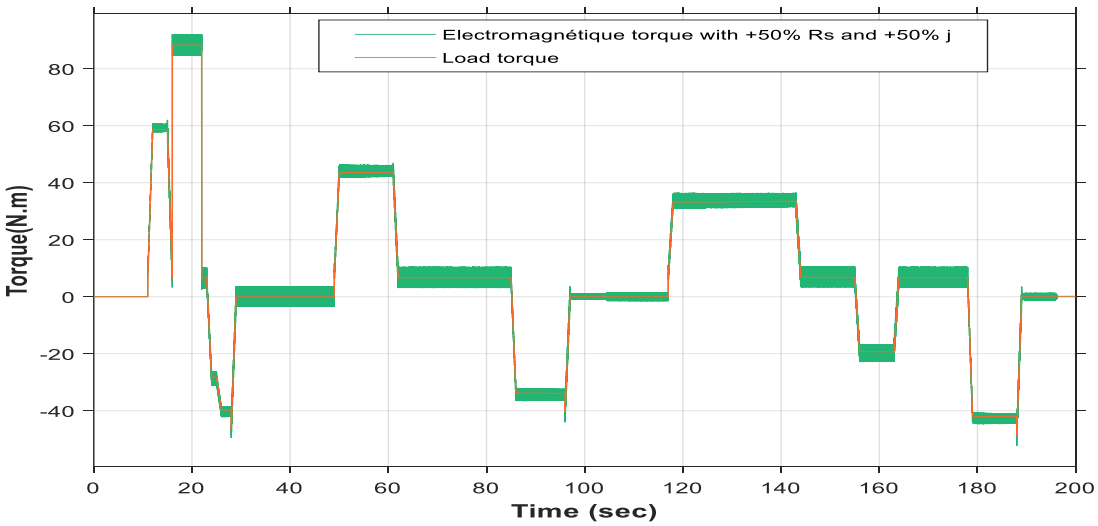

Figure 4.20. Simulation results of the torque with variations in inertia (*j*)

and resistance (R)- (HFSMC)

These results confirm that the hybrid control approach (HFSMC) provides enhanced robustness and improved dynamic performance compared to the classical SMC strategy, even in the presence of significant parameter variations.

4.10 Conclusion

The work presented in this chapter focuses on nonlinear control, specifically sliding mode control and fuzzy sliding mode control, to regulate the speed of a permanent magnet synchronous traction motor.

First, the theoretical foundations of sliding mode controllers are introduced, followed by their application to the vector decoupling of the PMSM (Permanent Magnet Synchronous Motor) using the principle of cascade control applied to the traction system. Next, the fuzzy sliding mode control approach is presented. The goal of this hybrid control method is to build a bridge between fuzzy control—whose undeniable performance makes it increasingly attractive to researchers—and sliding mode control, which demonstrates stability and robustness against parametric and external disturbances. Therefore, it combines the advantages of both techniques.

The application of this control strategy to the PMSM has yielded good results, overcoming the chattering issues associated with sliding mode control and the lack of analytical tools in fuzzy logic control, while also reducing the number of fuzzy rules. The robustness of this control approach is demonstrated through the obtained simulation results.

General Conclusion

General conclusion

The depletion and rising costs of fossil fuels, combined with increasing global awareness of climate change, have driven the development of electric vehicles in recent years. These vehicles now represent a viable industrial solution for reducing fuel consumption, thereby lowering CO_2 emissions and other harmful pollutants. This trend is further evidenced by the fact that a majority of automotive manufacturers have already implemented, or are in the process of implementing, electrification strategies, primarily through electric traction systems and hybrid powertrains. These technologies contribute to a substantial reduction in fuel consumption and overall environmental impact. In this context, automotive manufacturers are expected to contribute to this strategy by investing in research and development of new hybrid or fully electric traction vehicle prototypes. To ensure that the performance of these vehicles is comparable to that of internal combustion engine vehicles, significant technological advancements are required. The deployment of fully electric traction vehicles would not be feasible without the use of static power converters.

The study of multilevel converters represents a major research focus in the field of improving power supply signals for electric machines. Numerous current works are oriented toward advanced control methods based on the use of artificial intelligence, aiming for efficient and robust control of multilevel converters. The objective of this thesis is to develop specific control methods for a new multilevel converter topology that enhance the performance of multi-source electric vehicles. In this work, a modeling and optimization study is conducted on the traction chain of an electric vehicle composed of a permanent magnet synchronous motor (PMSM) powered by a new multilevel inverter topology, itself supplied by a hybrid energy source (fuel cell and supercapacitor). The traction system requires control strategies that are robust against disturbances, parameter variations, and nonlinearities. In this context, a technical review of the evolution of hybrid vehicles is provided, highlighting key developments in system architecture and component configurations. Several hybrid vehicle (HV) architectures are discussed, along with a detailed description of the primary components of the electric traction system, including electric machines, power converters, and energy sources.

Subsequently, following the mathematical formulation of the dynamic forces acting on the vehicle, detailed models of the internal components of each subsystem—including the permanent magnet synchronous motor (PMSM), fuel cell, and super-capacitor—were developed. These models provided the necessary framework for the design and implementation of the proposed control strategies.

In the subsequent section, we present an analysis of a hybrid power supply for electric-vehicle traction, comprising two energy sources and two DC–DC converters. The primary source is a fuel cell, while the secondary source is a super-capacitor. The core objective is to implement a robust control scheme that ensures a constant DC-bus voltage under abrupt load disturbances. Both energy sources interface with the DC bus via a boost converter and a buck–boost converter. These converters facilitate regulation of the DC-bus voltage and orchestrate power flow to the traction load. First, after modeling the sources and with the aim of regulating the voltage at the DC bus, the fuel cell was simulated with an interleaved Boost converter. The results obtained were satisfactory. Second, the supercapacitor was simulated with a Buck-Boost converter using a simple PI controller. The results obtained were satisfactory. Next, we introduced a new hybrid asymmetric multilevel inverter with a reduced component count. The main advantage of the proposed topology lies in its ability to generate a high number of voltage levels with fewer switching elements compared to conventional converters. This topology promises significant improvements in voltage waveform quality, cost, and efficiency. A (PD–SPWM) modulation technique was applied to the proposed inverter topology.

To control the traction system, we focused on modeling nonlinear Sliding Mode Control (SMC) applied to the permanent-magnet synchronous motor (PMSM) driven by a 21-level asymmetric inverter. This technique delivers rapid speed and electromagnetic-torque responses, thereby ensuring effective decoupling between these two variables for precise speed tracking and satisfactory dynamic performance. However, SMC suffers from the chattering phenomenon. To mitigate this, a hybrid fuzzy sliding-mode control (HFSMC) scheme was proposed to reduce chattering. The simulation tests of the complete system (MATLAB Simulink) will be performed to evaluate its dynamic performance and efficiency, focusing on both tracking accuracy and robustness.

The results of this thesis provide a foundation for several promising avenues of future research:

- Experimental validation of the proposed topology on an electric vehicle (EV) to assess the accuracy and practical feasibility of the developed simulation model.
- Integration of advanced control strategies based on artificial intelligence (AI) techniques to further enhance the performance, adaptability, and robustness of the control system.
- Implementation of real-time control using embedded systems or FPGA platforms to evaluate the system's performance under realistic operating conditions.

Appendix

Appendix

Appendix A

The machine parameters must be specified in the electric drive model of the PMSM in Matlab/Simulink. The electric motor of the Hy Power Bora has the following characteristics:

-Constant torque of 255 Nm between 0 and 1200 tr/min

-Constant power of 50 kW between 1200 and 1540 tr/min

-DC bus voltage: 570 V

Table A.1 represents the PMSM parameters used in this work.

Table A.1: Electric motor parameters PMSM [65].

Stator resistance	0.005 Ω
Stator inductance	0.3 mH
Inertia	0.25 $Kg.m^2$
Friction coefficient	0.005 Nm.s
Pole pairs	4
Magnets' induced flux	0.192 Wb

Appendix B

Several parameters such as the vehicle mass, kinematics, and geometry. The parameters to be specified are those of the Volkswagen Bora HY Power (Table B.1).

Table B.1: EV parameters [65].

M : The vehicle's mass (Kg)	1000 Kg
V : Vehicle speed	140 Km/h
SC_x: Coefficient of master torque (m^2)	0.46
P_{air} : The air density(Kg/m^3)	0.23

C_r : The vehicle's rolling coefficient	0.008
g : Gravitational acceleration (m/s^2)	9.81
R_r : Radius of the wheel	0.25
i : Gearbox transition ratio	3

Appendix C

Fuel cell parameters:

Table C.1: FC parameters [65].

E = 27.1 V (55°C)
I_0 = 6.54 mA
A = 1.35 V
B = 1.29 V
R_m = 0.045 Ω
i_n = 230 mA
i_L = 100 A

Appendix D

Super-capacitor paramètres:

Table D.1: Parameters of the BCAP 3000 super-capacitors [65].

ELECTRICAL	BCAP3000
Rated Capacitance[1]	3,000 F
Minimum Capacitance, initial[1]	3,000 F
Maximum ESR $_{DC}$ initial[1]	0.29 mΩ
Rated Voltage	2.70 V
Absolute Maximum Voltage[11]	2.85 V
Maximum Continuous Current ($\Delta T = 15°C$)[2]	130 A_{RMS}
Maximum Continuous Current ($\Delta T = 40°C$)[2]	210 A_{RMS}
Maximum Peak Current, 1 second [3]	2,200 A
Leakage Current, maximum [4]	5.2 mA

TEMPERATURE	BCAP3000
Operating temperature range (Cell case temperature)	
Minimum	-40°C
Maximum	65°C
Storage temperature range (Stored uncharged)	
Minimum	-40°C
Maximum	70°C

PHYSICAL	BCAP3000
Mass, typical	510 g
Terminals	Threaded or Weldable
Vibration	IEC 16750
Shock	SAE J2464

Reference

References

[1] R. Deng, Y. Xiang, D. Huo, Y. Liu, Y.Huang, and J. C Liu, "Exploring flexibility of electric vehicle aggregators as energy reserve." Electric Power Systems, Vol. 184, pp.106305, 2020. doi.org/10.1016/j.epsr.2020.106305.

[2] Y. Wang, T. John, and B.A. Xiong,"two-level coordinated voltage control scheme of electric vehicle chargers in low-voltage distribution networks." Electric power Systems, Vol.168, pp.218–227, 2019. https://doi.org/10.1016/j.epsr.2018.12.005.

[3] K. Van den Bergh, and E. Delarue, "Energy and reserve markets: interdependency in electricity systems with a high share of renewables." Electric Power Systems. Vol. 189, pp. 106537, 2020. https://doi.org/10.1016/j.epsr.2020.106537

[4] M. Salehifar, M. Moreno-Eguilaz, G. Putrus, and P. Barras, "Simplified fault tolerant finite control set model predictive control of a five-phase inverter supplying bldc motor in electric vehicle drive." Electric Power System. Vol. 132, pp. 56-66, 2016. https://doi.org/10.1016/j.epsr.2015.10.030

[5] S. Mathiyalagan, K. Nagarajan, K. Chandrasekaran, and B. Sourav, " Power management for fuel-cell electric vehicle using Hybrid SHO-CSGNN approach" , Energy Reports, Vol. 11, pp: 6069-6082, 2024. https://doi.org/10.1016/j.egyr.2024.05.003

[6] Y. Zhang, G. Chen, Y. Hu, C. Gong, and Y. Wang, "Cascaded multilevel inverter based power and signal multiplex transmission for electric vehicles." CES Trans. Electr. Mach. Syst. 4, 123–129, 2020. doi: 10.30941/CESTEMS.2020.00017.

[7] M. Chindamani, C.S. Ravichandran, and M. Alamelumangai, "Drive Control using Multilevel Inverter for Electric Vehicle Application: A Hybrid SCSO-SNN Technique," IETE Journal, Vol.70, No.11, pp.8232-8241, 2024. https://doi.org/10.1080/03772063.2024.2378475

[8] S. Bouradi, "Intelligent Control Of New Static Converter Structures For Vehicular Applications" , PHD thesis, Université de TIARET, 2023.

[9] H. Akagi, "Multilevel Converters: Fundamental Circuits and Systems," in Proceedings of the IEEE, vol. 105, no. 11, pp. 2048-2065, Nov. 2017, doi: 10.1109/JPROC.2017.2682105.

[10] M. J. Sathik, N. P. Gopinath, A. Hota, K. Vijayakumar, S. Mekhilef , and V. Agarwal, "Improved Dual Boost Mid-Point Clamped Five-Level Inverter Topology," in IEEE Transactions on Circuits and Systems II: Express Briefs, vol. 71, no. 6, pp. 3221-3225, 2024, doi: 10.1109/TCSII.2024.3356171.

[11] B. Dmitry, B. Eli, B. Svetlana, S. Moshe, A. Ilan, and K. Alon, "High power T-type-based multi-level inverter for electric vehicles", Energy Reports, Vol. 9, pp. 220-225, 2023. doi: 10.1016/j.egyr.2023.09.181

[12] G. Deshmukh, P. Chaturvedi and V. Rajderkar, "Single phase Cascaded H-Bridge Multilevel Inverter Topology," International Conference on Futuristic Technologies (INCOFT), Belgaum, India, 2022, pp. 1-6, doi: 10.1109/INCOFT55651.2022.10094514.

[13] S. Cai, V. Kirtley, and C. H. T. Lee, "Critical Review of Direct-Drive Electrical Machine Systems for Electric and Hybrid Electric Vehicles," in IEEE Transactions on Energy Conversion, Vol. 37, No. 4, pp. 2657-2668, 2022. doi: 10.1109/TEC.2022.3197351

[14] Z. Huang, et al., "Profiling the Eddy Current Losses Variations of High-Speed Permanent Magnet Machines in Plug-In Hybrid Electric Vehicles," in IEEE Transactions on Transportation Electrification, Vol. 8, No. 3, pp. 3451-3463, 2022. doi: 10.1109/TTE.2022.3152845.

[15] X. Liu, J. Zhao, S. Wang and Q. Xiang, "Research on Sliding Mode Control and Fuzzy Control Strategies of Motor Drive System for New Energy Vehicles," 40th Chinese Control Conference (CCC), Shanghai, China, pp. 5971-5976, 2021, doi: 10.23919/CCC52363.2021.9550587.

[16] Z. Zhao, X. Peng, Y. Guo and J. Chen, "Vector Control of PMSM Servo System Based on Fuzzy Terminal Sliding Mode Control,"42nd Chinese Control Conference (CCC), Tianjin, China, pp. 432-437, 2023, doi: 10.23919/CCC58697.2023.10240111

[17] J. Zhang, Y. Che, R. Teodorescu, et al, "Energy storage management in electric vehicles." Nat. Rev. Clean Technol. 1, 161–175 , 2025. https://doi.org/10.1038/s44359-024-00020-2

[18] I. Kranthikumar, C.H. Srinivas, T.V. Kiran, et al. "A novel hybrid approach for efficient energy management in battery and supercapacitor based hybrid energy storage systems for electric vehicles." Electr Eng 107, 1–17, 2025, https://doi.org/10.1007/s00202-024-02483-9

[19] E. Taherzadeh, H. Radmanesh and A. Mehrizi-Sani, "A Comprehensive Study of the Parameters Impacting the Fuel Economy of Plug-In Hybrid Electric Vehicles," in IEEE Transactions on Intelligent Vehicles, vol.5, no. 4, pp. 596-615, 2020, doi: 10.1109/TIV.2020.2993520

[20] H. Maghfiroh, O. Wahyunggoro and A. I. Cahyadi, "Energy Management in Hybrid Electric and Hybrid Energy Storage System Vehicles: A Fuzzy Logic Controller Review," in IEEE Access, vol. 12, pp. 56097-56109, 2024, doi: 10.1109/ACCESS.2024.3390436.

[21] Z. Zhu, C. Li, Y. Tian and Q. Wei, "Parametric Matching and Simulation Analysis of the Series-parallel Hybrid Electric Vehicle," 2020 IEEE 5th Information Technology and Mechatronics Engineering Conference (ITOEC), Chongqing, China, pp. 325-329, 2020, doi: 10.1109/ITOEC49072.2020.9141916.

[22] J. Pierquin," Contribution a la Commande des Systèmes Multimachines Multiconvertisseurs Application a la Résolution de Problèmes en Traction Electrique", Thèse De Doctorat , Génie Electrique ,Université Des Sciences Et Technologies De Lille, Juillet 2002 .

[23] K. T. Chau ,"Electric Vehicle Machines and Drives Design, Analysis and Application", International Research Centre for Electric Vehicles the University of Hong Kong , John Wiley & Sons Singapore Pte , 2015.

[24] K. Hartani , M. Bourahla ,Y. Miloud ,and M. Sekour ,"Electronic Differential with Direct Torque Fuzzy Control for Vehicle Propulsion System", Turk J Elec Eng & Comp Sci, Vol.17, No.1, pp. 21-38, 2009.

[25] V. Reinbold ,"Méthodologie de Dimensionnement d'un Moteur Electrique pour Véhicules Hybrides Optimisation Conjointe des Composants et de la Gestion d'Energie", Thèse de doctorat en Génie Electrique, Université de Grenoble, Août 2006.

[26] D. Lechner, "Analyse du Comportement Dynamique Des véhicules Routiers Légers Développement d'une Méthodologie Appliquée a la Sécurité Primaire , Thèse de doctorat en Mécanique , Ecole Centrale de Lyon , juin 2002.

[27] M. B. Camara, "Supercondensateurs pour Échange Dynamique D'énergie a bord du Véhicule Électrique Hybride Modélisation, Etude des Convertisseurs et Commande", Thèse de doctorat en Génie Electrique, Université de Franche- Comté, France , Décembre 2007.

[28] R. Rajamani , "Vehicle Dynamics and Control", Mechanical Engineering Series book series (MES),University of Minnesota, USA, Springer, 2006.

[29] B. Haidar, "A techno-economic analysis of the electric vehicle transition: Policy, infrastructure, usage, and design," Ph.D. dissertation, Université Paris-Saclay, 2021.

[30] R. Xiong, W. Shen, "Battery Management Systems in Electric Vehicles," in Advanced Battery Management Technologies for Electric Vehicles , Wiley, pp.231-248, 2019, doi: 10.1002/9781119481652.ch8.

[31] J. Deng, C. Bae, A. Denlinger, and T. Miller, "Electric vehicles batteries: Requirements and challenges,"Joule, vol. 4, no. 3, pp. 511–515, 2020.

[32] M. Hassan, "Machine learning optimization for hybrid electric vehicle charging in renewable microgrids." Sci Rep 14, 13973, 2024, https://doi.org/10.1038/s41598-024-63775-5

[33] E. A. Grunditz and T. Thiringer, "Performance Analysis of Current BEVs Based on a Comprehensive Review of Specifications," in IEEE Transactions on Transportation Electrification, vol. 2, no. 3, pp. 270-289, 2016, doi: 10.1109/TTE.2016.2571783.

[34] J. Deng, C. Bae, A. Denlinger, and T. Miller, "Electric vehicles batteries: Requirements and challenges,"Joule, vol. 4, no. 3, pp. 511–515,ISSN: 2542-4351, 2020, doi: https://doi.org/10.1016/j

[35] B. Das, P. K. Panigrahi and C. K. Samant, "Impact Analysis of Plug-in Hybrid Electric Vehicle on Integration with Micro grid -A Review," IEEE International Symposium on Sustainable Energy, Signal Processing and Cyber Security (iSSSC), Gunupur Odisha, India, pp. 1-5,2020, doi: 10.1109/iSSSC50941.2020.9358824.

[36] B. Eom, K. Eom, D. Yang, et al. "Novel Electric Vehicle Powertrain of Multi-stack Fuel Cell Using Optimal Energy Management Strategy." Int.J Automot. Technol. 25, 201–211 , 2024. https://doi.org/10.1007/s12239-024-00010-0

[37] S. Hou, X. Liu, H. Yin and J. Gao, "Reinforcement Learning-Based Energy Optimization for a Fuel Cell Electric Vehicle," 4th International Conference on Smart Power & Internet Energy Systems (SPIES), Beijing, China, pp. 1928-1933, 2022 doi: 10.1109/SPIES55999.2022.10082644.

[38] R. Á. Silva, F. J. Pujatti, and I. A. Pires, "Nine-phase im for hybridisation of a compact vehicle by parallel ttr architecture," IET Electric Power Applications, vol. 12, no. 8, pp. 1134–1141, 2018, https://doi.org/10.1049/iet-epa.2017.0783.

[39] S. Wang, Z. Zhang, Y. Hou, P. Liu and Z. Wang, "Research on Plug-in Hybrid Electric Vehicle Bus Utility Factor Based on Real-World Data," 6th International Conference on Transportation Information and Safety (ICTIS), Wuhan, China, 2021, pp. 799-804, doi: 10.1109/ICTIS54573.2021.9798549.

[40] P. Egede, "Environmental assessment of lightweight electric vehicles", pp. 94-98. 2017, Cham: Springer.

[41] B. Sarrazin, "Optimisation d'une chaine de traction pour véhicule électrique" PhD thesis, Grenoble (2012).

[42] C. A. Bilaţiu, S. I. Cosman, R. A. Marţiş, C. S. Marţiş and S. Morariu, "Identification and Evaluation of Electric and Hybrid Vehicles Propulsion Systems," Electric Vehicles International Conference (EV), Bucharest, Romania, 2019, pp. 1-5, doi: 10.1109/EV.2019.8892965.

[43] B. Gasbaoui, "Analyse et Commande Directe du Couple d'un Véhicule Electrique a deux Roues Motricess," PhD thesis, Université de Béchar, 2012.

[44] K. Young, C. Wang, L. Y. Wang, and K. Strunz, "Electric vehicle battery technologies. In Electric vehicle integration into modern power networks," (pp. 15-56), New York, NY: Springer New York, 2012.

[45] X. Sun, Z. Li, X.Wang, and C. Li, "Technology development of electric vehicles: A review," Energies, vol. 13, no. 1, p. 90, 2019, https://doi.org/10.3390/en13010090.

[46] Z. Li, A. Khajepour, and J. Song, "A comprehensive review of the key technologies for pure electric vehicles," Energy, vol. 182, pp. 824–839, 2019, https://doi.org/10.1016/j.energy.2019.06.077

[47] F. Un-Noor, S. Padmanaban, L. Mihet-Popa, M. N. Mollah, and E. Hossain, "A comprehensive study of key electric vehicle (ev) components, technologies, challenges, impacts, and future direction of development," Energies, vol. 10, no. 8, p. 1217, 2017, https://doi.org/10.3390/en10081217

[48] M. Iqbal, “Design and control of hybrid electric vehicle for efficient urban use.,” Ph.D. dissertation,Université Bourgogne Franche-Comté, 2022.

[49] K. Okba, “Control and energy management of an electrical vehicle,” Ph.D. dissertation, 2015.

[50] M. S. Alam Chowdhury, K. A. A. Mamun and A. M. Rahman, "Modelling and simulation of power system of battery, solar and fuel cell powered Hybrid Electric vehicle," 3rd International Conference on Electrical Engineering and Information Communication Technology (ICEEICT), Dhaka, Bangladesh, 2016, pp. 1-6, doi: 10.1109/CEEICT.2016.7873126.

[51] S. Maakaroun ," Modélisation et Simulation Dynamique d’un Véhicule Urbain Innovant en Utilisant le Formalisme de la Robotique", Thèse de doctorat en Automatique, Productique, Université Nantes Angers le Mans , Décembre 2011.

[52] A. Etxeberria, I. Vechiu, H. Camblong, S. Kreckelbergh, and S. A. Bacha, Florescu,Gestion optimisée des flux énergétiques dans le véhicule électrique PhD thesis Thése de doctorat du Grenoble INP, Grenoble, 2012.

[53] R. Dwivedi, S. Singh, B. Singh, A. Chandra and M. Rezkallah, "Three-Phase AC/DC Converter fed Two Parallel Interleaved DC-DC Converters for Fast Charging Applications with Improved Power Quality," IEEE 14th International Conference on Power Electronics and Drive Systems (PEDS), Montreal, QC, Canada, 2023, pp. 1-6, doi: 10.1109/PEDS57185.2023.10246676.

[54] S. Bouradi, K. Negadi, R. Araria, B. Boumediene, and M. Koulali, “Design and implementation of a four-quadrant dc-dc converter based adaptive fuzzy control for electric vehicle application,”Mathematical Modelling of Engineering Problems, vol. 9, no. 3, pp. 721–730, 2022. https://doi.org/10.18280/mmep.090319.

[55] R. Araria, A. Berkani, K. Negadi, F. Marignetti, M. Boudiaf, et al., “Performance analysis of dc-dc converter and dtc based fuzzy logic control for power management in electric vehicle application,” Journal Europeen des Systemes Automatises, vol. 53, no. 1, pp. 1–9, 2020. https://doi.org/10.18280/jesa.530101.

[56] S. N. Pise, A. L. Jagtap, S. Yeolekar and N. Lokhande, "Comprehensive analysis of Rolling Resistance Coefficients on various road conditions and their effect on electric vehicle performance," International Conference on Intelligent Systems and Advanced Applications (ICISAA), Pune, India, 2024, pp. 1-6, doi: 10.1109/ICISAA62385.2024.10828627.

[57] O. Trigui, E. Mejri, Y. Dube, S. Kelouwani and K. Agbossou, "Energy Efficient Routing Estimation in Electric Vehicle with Online Rolling Resistance Estimation," IEEE Vehicle Power and Propulsion Conference (VPPC), Belfort, France, 2017, pp. 1-6, doi: 10.1109/VPPC.2017.8330912.

[58] A. Louwen, W. G. Van Sark, A. P. Faaij, and R. E. Schropp, “Re-assessment of net energy production and greenhouse gas emissions avoidance after 40 years of photovoltaics development,” Nature Communications, vol. 7, no. 1, p. 13 728, 2016. https://doi.org/10.1038/ncomms13728

[59] L. Gasc ," Conception d’un actionneur à aimants permanents à faibles ondulations de couple pour assistance de direction automobile Approches par la structure et par la commande ", thèse de doctorat de l’institut national polytechnique Toulouse 2004.

[60] M.A. Ferreira De Sousa ," Contribution à la conception de lois de commande à caractère robuste pour une machine synchrone entrainant une charge élastique à inertie variable ", thèse de doctorat institut national polytechnique de Toulouse, 2007.

[61] S. Belakehal ," Conception & Commande des Machines à Aimants Permanents Dédiées aux Energies Renouvelables", Thèse de doctorat, université de Constantine, Juin 2010.

[62] M. S. Merzoug ," Machines synchrone à aimants permanents (MSAP) techniques de commandes et applications " , thèse de doctorat, université de Mentouri Constantine Algérie, 2012.

[63] L. Djafer, R. Taleb, F. Mehedi, “ Dspace implementation of real-time selective harmonics elimination technique using modified carrier on three phase inverter.” Electrical Engineering & Electromechanics, no. 5, pp. 28-33, 2024, doi: https://doi.org/10.20998/2074-272X.2024.5.04

[64] A. Khlaief ," Contribution à la commande vectorielle sans Capteur Mécanique des Machines Synchrones à Aimants Permanents (MSAP) ", thèse de doctorat, AIXMarseille Université, Juillet 2012.

[65] A. Larbaoui ,"Commandes Non Linéaires Robustes Appliquées à un Moteur Synchrone à Aimants Permanents," Mémoire de Magister , Spécialité : Electrotechnique Option : Systèmes électro-énergétiques, Universite Djillali Liabes de Sidi-Bel-Abbes ,2013.

[66] M. Koteich ," Modélisation et Observabilité des Machines Electriques en Vue de la Commande sans Capteur Mécanique", Thèse de doctorat en Automatique , Université Paris-Saclay, Mai 2016.

[67] R. Sen, S. Shukla and S. Singh, "A Novel Control Strategy of Fuel Cell Interactive Battery Based E-mobility System," 3rd International conference on Power Electronics and IoT Applications in Renewable Energy and its Control (PARC), Mathura, India, pp. 409-414, 2024 doi: 10.1109/PARC59193.2024.10486543.

[68] H. Mishra, S. Ray and S. Rathore, "Energy Management Strategy in Fuel Cell Hybrid Vehicle with CDM Controllers," International Conference on Advances in Electrical, Computing, Communication and Sustainable Technologies (ICAECT), Bhilai, India, pp. 1-6, 2021, doi: 10.1109/ICAECT49130.2021.9392620.

[69] A. Lahyani, P. Venet, A. Guermazi and A. Troudi, "Battery/Supercapacitors Combination in Uninterruptible Power Supply (UPS)," in IEEE Transactions on Power Electronics, vol. 28, no. 4, pp. 1509-1522, 2013, doi: 10.1109/TPEL.2012.2210736.

[70] T. Mesbahi , N. Rizoug , P. Bartholomeus , and P. Lemoigne ,"Pris en compte du Vieillissement pour la Modélisation d'une Source Hybride Batterie/ Supercondensateur", Symposium de Genie Electrique (Sge'14) : EF-EPF-MGE 2014, pp.8-10, Ens Cachan, France, Juillet 2014.

[71] A. M. Puşcaş, M. C. Carp, C. Z. Kertész, P. N. Borza and G. Coquery, "Thermal and voltage testing and characterization of supercapacitors and batteries," 2010 12th International Conference on Optimization of Electrical and Electronic Equipment, Brasov, Romania, pp. 125-132, 2010, doi: 10.1109/OPTIM.2010.5510502.

[72] H. Maker ,"Optimisation et Gestion D'énergie pour un Système Hybride : Association Pile à Combustible et Super-condensateurs", Thèse de Doctorat en Automatique, Electronique de puissance, Universite De Technologie Belfort Montbeliard , Novembre 2008.

[73] A. Laire ,"Méthodologies de Modélisation et de Gestion L'énergie de Systèmes de Stockage Mixtes pour Véhicules Electrique et Hybrides", Thèse de doctorat en Génie Électrique , Université Lille 1 Sciences et Technologies , Septembre 2010.

[74] A. Boucherit ," Conception d'un Convertisseur de Puissance pour les Véhicules Electriques Multi-sources", Thèse de doctorat en Génie Électrique, Université de technologie de Belfort Montbéliard, Décembre 2011.

[75] E. Oksuztepe, M. Yildirim, "PEM fuel cell and supercapacitor hybrid power system for four in-wheel switched reluctance motors drive EV using geographic information system," International Journal of Hydrogen Energy, Vol; 75, PP. 74-87, 2024, https://doi.org/10.1016/j.ijhydene.2023.12.207

[76] A.S. Mohamed, S.M.Atnaw, A.O.Salau, J.N. Eneh, "Review of optimal sizing and power management strategies for fuel cell/battery/super capacitor hybrid electric vehicles," Energy reports, vol 9, pp. 2213-2228, 2023, https://doi.org/10.1016/j.egyr.2023.01.042

[77] S. K. Pradhan, S. S. and I. Chakraborty, "A High Gain DC-DC Converter based FC-Battery-SC System for EV Application," 2023 IEEE Silchar Subsection Conference (SILCON), Silchar, India, 2023, pp. 1-5, doi: 10.1109/SILCON59133.2023.10404918.

[78] M. Karthikeyan, G. Ramesh, P. Jayakrishnan and M. Jayakumar, "Review on Energy Storage Technology and Energy Management Strategies in Electric Vehicles," Innovations in Power and Advanced Computing Technologies (i-PACT), Kuala Lumpur, Malaysia, pp. 1-6, 2021, doi: 10.1109/i-PACT52855.2021.9696530.

[79] Y. Guttula and S. Samanta, "Modeling and Control Implementation of Interleaved Coupled and Uncoupled Boost Converter for EV Drive Applications," IEEE 18th India Council

International Conference (INDICON), Guwahati, India, pp. 1-6, 2021, doi: 10.1109/INDICON52576.2021.9691491.

[80] M. Andleeb, K. L. Khan, S. Hussain and S. J. Iqbal, "Non-Linear Modeling and Control of DC-DC Buck and Boost Converters For EV Application," 2022 1st International Conference on Sustainable Technology for Power and Energy Systems (STPES), SRINAGAR, India, pp. 1-6, 2022, doi: 10.1109/STPES54845.2022.10006486.

[81] M. B. Camara, B. Dakyo and H. Gualous, "Energy management based on two-phase interleaved buck-boost and boost converters for Electric Vehicles applications - using lithium-battery and fuel cell," International Conference on Renewable Energy Research and Applications (ICRERA), Nagasaki, Japan, pp. 1-6, 2012, doi: 10.1109/ICRERA.2012.6477433.

[82] L. Djafer, R. Taleb, F. Mehedi, A. Aissa Bokhtache, T. Bessaad, F. Chabni, H. Saidi, "Electric drive vehicle based on sliding mode control technique using a 21-level asymmetrical inverter under different operating conditions." Electrical Engineering & Electromechanics, no. 3, pp. 31-36, 2025. doi: https://doi.org/10.20998/2074-272X.2025.3.05

[83] R. Anand, R.K. Mandal, "Experimental Design and Analysis of Symmetrical and Asymmetrical Multilevel Inverters." Iran J Sci Technol Trans Electr Eng 47, 983–992, 2023, https://doi.org/10.1007/s40998-023-00602-z

[84] A. Ghosh and Y. Pal, "A Simplified Space Vector PWM Technique of Three-Level Diode Clamped Inverter with Rectifier Side Direct Power Control Topology," 2nd International Conference on Emerging Frontiers in Electrical and Electronic Technologies (ICEFEET), Patna, India, pp. 1-6, 2022, doi: 10.1109/ICEFEET51821.2022.9848393.

[85] B. Rooholahi, "A New Two-Stage Single-Phase Transformerless Inverter Topology with a Novel DC/DC High Gain Boost Converter and a Three-Level Neutral-Point-Clamped Inverter for Photovoltaic Systems," 23rd European Conference on Power Electronics and Applications (EPE'21 ECCE Europe), Ghent, Belgium, pp. 1-9, 2021, doi: 10.23919/EPE21ECCEEurope50061.2021.9570598.

[86] M. J. Sathik, Z. Tang, Y. Yang, K. Vijayakumar and F. Blaabjerg, "A New 5-Level ANPC Switched Capacitor Inverter Topology for Photovoltaic Applications," IECON 2019 - 45th Annual Conference of the IEEE Industrial Electronics Society, Lisbon, Portugal, pp. 3487-3492, 2019, doi: 10.1109/IECON.2019.8926832.

[87] J. Yuan, O. Oghorada, L. Zhang, "Loss analysis of three-level flying capacitor converter-based EV chargers using hybrid WBG-Si devices", future batteries, Vol. 6, , pp. 100066, 2025, https://doi.org/10.1016/j.fub.2025.100066

[88] K. Antoniewicz, M. Jasinski, M. P. Kazmierkowski, and M. Malinowski. Model predictive control for three-level four-leg flying capacitor converter operating as shunt active power filter.

IEEE Transactions on Industrial Electronics, 63(8):5255–5262, Aug 2016. ISSN 0278-0046. doi: 10.1109/TIE.2016.2536584.

[89] A.Adem, F.Kacar, N. Matorakis,"Enhancement design of eleven-level cascaded h-bridge motor driver application," computers and electrical engineering, Vol. 123, Part C, pp. 110179, 2025, https://doi.org/10.1016/j.compeleceng.2025.110179.

[90] M. B. Latran, and A. Teke. "Investigation of multilevel multifunctional grid connected inverter topologies and control strategies used in photovoltaic systems". Renewable and Sustainable Energy Reviews, 42:361 – 376, 2015. ISSN 1364-0321. doi: https://doi.org/10.1016/j.rser.2014.10.030.

[91] S. Sudha Letha, T. Thakur, and J. Kumar, "Harmonic elimination of a photo-voltaic based cascaded h-bridge multilevel inverter using pso (particle swarm optimization) for induction motor drive." Energy, 107:335 – 346, 2016. ISSN 0360-5442. doi: https://doi.org/10.1016/j.energy.2016.04.033.

[92] P. G. Song, E. Y. Guan, L. Zhao, and S. P. Liu. "Hybrid electric vehicles with multilevel cascaded converter using genetic algorithm." In 2006 1ST IEEE Conference on Industrial Electronics and Applications, pp. 1–6, May 2006. doi: 10.1109/ICIEA.2006.257211.

[93] M. Senthilkumar, S. Prabhu, U. Arun Kumar, et al. "EV charging and fuel cell vehicle refuelling with distributed energy resources using hybrid approach. " Environ Dev Sustain 2024, https://doi.org/10.1007/s10668-024-05138-8

[94] A. Ouadah, I. Merzouk, A. Hafaifa, et al. "Enhancing Energy Efficiency for Sustainable Mobility in Fuel Cell Electric Vehicles via an Integrated Intelligent Energy Management System." Process Integr Optim Sustain , 2025. https://doi.org/10.1007/s41660-025-00548-1.

[95] S. Poorani, P. Kathirvel, T.M. Murugan, et al, "A Novel Differential Flatness Control Approach of an Electric Vehicle Using Energy Management Methodology." Iran J Sci Technol Trans Electr Eng, 2025. https://doi.org/10.1007/s40998-025-00819-0

[96] P. Kalaivani, C.S. Joice, "Design and modelling of a neural network-based energy management system for solar PV, fuel cell, battery and ultracapacitor-based hybrid electric vehicle." Electr Eng 106, pp. 689–709, 2024. https://doi.org/10.1007/s00202-023-02015-x

[97] E. Lu, W. Li, S. Jiang and Y. Liu, "Anti-Disturbance Speed Control of Permanent Magnet Synchronous Motor Based on Fractional Order Sliding Mode Load Observer," in IEEE Access, vol. 12, pp. 71716-71732, 2024, doi: 10.1109/ACCESS.2022.3214205

[98] L. Zhang, Z. Chen, X. Yu, J. Yang and S. Li, "Sliding-Mode-Based Robust Output Regulation and Its Application in PMSM Servo Systems," in IEEE Transactions on Industrial Electronics, vol. 70, no. 2, pp. 1852-1860, Feb. 2023, doi: 10.1109/TIE.2022.3163536.

[99] Z.Zhang, Z.Chen, N.Li, K.Chen, N.C.Cheng, J.pan, “A dynamic convergence second-order sliding mode control structure for PMSM with an observer based on a novel sliding mode reaching law,” Vol. 164, pp.106504, 2025, https://doi.org/10.1016/j.conengprac.2025.106504

[100] B. Liu , Y. Zhao , H.Z. Hu, “Structure-variable sliding mode control of interior permanent magnet synchronous motor in electric vehicles with improved flux-weakening method. Advances in Mechanical Engineering.” 2018, 10(1). doi:10.1177/1687814017704355

[101] R. Guo, X. Wang, J. Zhao and W. Yu, "Fuzzy sliding mode direct torque control for PMSM," 2011 Eighth International Conference on Fuzzy Systems and Knowledge Discovery (FSKD), Shanghai, China, 2011, pp. 511-514, doi: 10.1109/FSKD.2011.6019599.

[102] M. Comanescu, "Minimum Time Speed Control of the Induction Motor Drive Using Discrete Time Sliding Mode," 2020 International Symposium on Power Electronics, Electrical Drives, Automation and Motion (SPEEDAM), Sorrento, Italy, pp. 213-218, 2020, doi: 10.1109/SPEEDAM48782.2020.9161899.

[103] H. Li and Q. Wang, "Sliding mode controller based on fuzzy neural network optimization for direct torque controlled PMSM," 2010 8th World Congress on Intelligent Control and Automation, Jinan, China, pp. 2434-2438, 2010, doi: 10.1109/WCICA.2010.5554684.

[104] S. Suganthi, R. Karpagam, “Dynamic performance improvement of PMSM drive using fuzzy-based adaptive control strategy for EV applications.” J. Power Electron. 23, 510–521 2023. https://doi.org/10.1007/s43236-023-00594-3

[105] R. Shenbagalakshmi, S.K.Mittal, J. Subramaniyan, et al. “Adaptive speed control of BLDC motors for enhanced electric vehicle performance using fuzzy logic.” Sci Rep 15, 12579 2025. https://doi.org/10.1038/s41598-025-90957-6

[106] R. Na and X. Wang, "An Improved Vector-Control System of PMSM Based on Fuzzy Logic Controller," 2014 International Symposium on Computer, Consumer and Control, Taichung, Taiwan, 2014, pp. 326-331, doi: 10.1109/IS3C.2014.92.

[107] D. Pawar and V. Bhole, "Fuzzy Logic-Based Controller of PMSM Motor for EV Application," 2023 3rd Asian Conference on Innovation in Technology (ASIANCON), Ravet IN, India, 2023, pp. 1-6, doi: 10.1109/ASIANCON58793.2023.10270755.

[108] Y. He et al., "Speed Observation of High-Speed Permanent Magnet Synchronous Motor Based on Fuzzy MRAS," 2020 39th Chinese Control Conference (CCC), Shenyang, China, 2020, pp. 3550-3555, doi: 10.23919/CCC50068.2020.9188464.

[109] V. Pahwa, D. Kumar, P. Bhushan, et al. “Improved Dynamics of Coupled 5-Phase Vector-Controlled PMSM Drive System with Model-Predictive-Controller.” Arab J Sci Eng 2025. https://doi.org/10.1007/s13369-024-09933-3

[110] B. Sangar, M. Singh, and M. Sreejeth, “Enhancing PMSM Drive Performance for Electric Vehicles Through ANFIS-HCC Integration.” Arab J Sci Eng 2025. https://doi.org/10.1007/s13369-025-10509-y

[111] L. Zhang, H. Li, L. Shan, L. Zhang, L. Zhang, “Double-hierarchical fuzzy exponential convergence law fractional-order sliding mode control for PMSM drive control in EV”, Engineering science and technology an international journal, vol. 47, pp.101536, 2023, https://doi.org/10.1016/j.jestch.2023.101536

[112] M. Monadi, M. Nabipour, F. Akbari-Behbahani and E. Pouresmaeil, "Speed Control Techniques for Permanent Magnet Synchronous Motors in Electric Vehicle Applications Toward Sustainable Energy Mobility: A Review," in IEEE Access, vol. 12, pp. 119615-119632, 2024, doi: 10.1109/ACCESS.2024.3450199.